

IntechOpen

Science, Technology and Advanced Application of Supercapacitors

Edited by Takaya Sato



Science, Technology and Advanced Application of Supercapacitors

Edited by Takaya Sato

Published in London, United Kingdom



IntechOpen





Supporting open minds since 2005



Science, Technology and Advanced Application of Supercapacitors

<http://dx.doi.org/10.5772/intechopen.76959>

Edited by Takaya Sato

Contributors

Arun Singh, Mohd Arif, Amit Sanger, Daisuke Tashima, Mohmmad Khalid, Prerna Bhardwaj, Vesselin Shanov, Sathya Kanakaraj, Yu-Yun Hsieh, Yanbo Fang, Noe Alvarez, Kevin Johnson, Paa Kwasi Adusei, Xiaogang Sun, Wei Chen, Xu Li, Jie Wang, Hao Hu, Guodong Liang, Yapan Huang, Chengcheng Wei, Sachindra Nath Das, Apurba Ray, Atanu Roy, Samik Saha, Enhua Wang, Minggao Ouyang, Fujun Zhang, Changlu Zhao, Randhir Bhorla, C.C. Tripathi

© The Editor(s) and the Author(s) 2019

The rights of the editor(s) and the author(s) have been asserted in accordance with the Copyright, Designs and Patents Act 1988. All rights to the book as a whole are reserved by INTECHOPEN LIMITED. The book as a whole (compilation) cannot be reproduced, distributed or used for commercial or non-commercial purposes without INTECHOPEN LIMITED's written permission. Enquiries concerning the use of the book should be directed to INTECHOPEN LIMITED rights and permissions department (permissions@intechopen.com).

Violations are liable to prosecution under the governing Copyright Law.



Individual chapters of this publication are distributed under the terms of the Creative Commons Attribution 3.0 Unported License which permits commercial use, distribution and reproduction of the individual chapters, provided the original author(s) and source publication are appropriately acknowledged. If so indicated, certain images may not be included under the Creative Commons license. In such cases users will need to obtain permission from the license holder to reproduce the material. More details and guidelines concerning content reuse and adaptation can be found at <http://www.intechopen.com/copyright-policy.html>.

Notice

Statements and opinions expressed in the chapters are those of the individual contributors and not necessarily those of the editors or publisher. No responsibility is accepted for the accuracy of information contained in the published chapters. The publisher assumes no responsibility for any damage or injury to persons or property arising out of the use of any materials, instructions, methods or ideas contained in the book.

First published in London, United Kingdom, 2019 by IntechOpen

eBook (PDF) Published by IntechOpen, 2019

IntechOpen is the global imprint of INTECHOPEN LIMITED, registered in England and Wales,

registration number: 11086078, The Shard, 25th floor, 32 London Bridge Street

London, SE19SG – United Kingdom

Printed in Croatia

British Library Cataloguing-in-Publication Data

A catalogue record for this book is available from the British Library

Additional hard and PDF copies can be obtained from orders@intechopen.com

Science, Technology and Advanced Application of Supercapacitors

Edited by Takaya Sato

p. cm.

Print ISBN 978-1-78985-801-3

Online ISBN 978-1-78985-802-0

eBook (PDF) ISBN 978-1-83962-111-6

We are IntechOpen, the world's leading publisher of Open Access books Built by scientists, for scientists

4,100+

Open access books available

116,000+

International authors and editors

120M+

Downloads

151

Countries delivered to

Our authors are among the
Top 1%

most cited scientists

12.2%

Contributors from top 500 universities



WEB OF SCIENCE™

Selection of our books indexed in the Book Citation Index
in Web of Science™ Core Collection (BKCI)

Interested in publishing with us?
Contact book.department@intechopen.com

Numbers displayed above are based on latest data collected.
For more information visit www.intechopen.com



Meet the editor



Professor Takaya Sato is currently the vice president of the National Institute of Technology, Tsuruoka College, Japan, and professor of polymer chemistry. He studied polymer and fiber chemistry at Shinshu University and Kyoto University. He received his PhD in Polymer Chemistry from Kyoto University in 1992 under the direction of Professor Takeaki Miyamoto. After acquiring a degree, he was engaged in the development of functional polymer materials such as microparticles for cosmetics, gel materials for microbial carriers, solid polymer electrolytes for lithium ion batteries, and novel ionic liquids in Nisshinbo Holdings, Inc. 2003 was the first time that an electric double layer capacitor using an ionic liquid as an electrolyte was commercialized. After moving to Tsuruoka College as a professor in 2004, Professor Miyamoto continues to develop ionic liquids and related polymer materials and is vigorously conducting research to apply them to electrochemical devices and low friction materials.

Contents

Preface	XIII
Section 1	
Science and Technology of Supercapacitors	1
Chapter 1	3
Carbon-Based Composites for Supercapacitor <i>by Mohmmad Khalid, Prerna Bhardwaj and Hamilton Varela</i>	
Chapter 2	21
Fabric-Integrated, Ionic Liquid-Based Supercapacitor as a Tunable and Flexible Power Source <i>by Sathya Narayan Kanakaraj, Paa Kwasi Adusei, Yu-Yun Hsieh, Yanbo Fang, Noe Alvarez and Vesselin Shanov</i>	
Chapter 3	39
Fiber Supercapacitors Based on Carbon Nanotube-PANI Composites <i>by Paa Kwasi Adusei, Yu-Yun Hsieh, Sathya Narayan Kanakaraj, Yanbo Fang, Kevin Johnson, Noe T. Alvarez and Vesselin Shanov</i>	
Chapter 4	55
Deterioration Factors of Electric Double-Layer Capacitors Obtained from Voltage Hold Test <i>by Daisuke Tashima</i>	
Chapter 5	73
Performance and Applications of Lithium Ion Capacitors <i>by Xiaogang Sun, Wei Chen, Xu Li, Jie Wang, Hao Hu, Guodong Liang, Yapan Huang and Chengcheng Wei</i>	
Chapter 6	89
Transition Metal Oxide-Based Nano-materials for Energy Storage Application <i>by Apurba Ray, Atanu Roy, Samik Saha and Sachindranath Das</i>	
Chapter 7	107
CrN Sputtered Thin Films for Supercapacitor Applications <i>by Mohammad Arif, Amit Sanger and Arun Singh</i>	

Section 2	
Application of Supercapacitors	115
Chapter 8	117
Performance Evaluation and Control Strategy Comparison of Supercapacitors for a Hybrid Electric Vehicle	
<i>by Enhua Wang, Mingguo Ouyang, Fujun Zhang and Changlu Zhao</i>	

Preface

Application fields of supercapacitors are expanding because they have a very large charge/discharge current density and a cycle durability of tens of thousands of cycles or more compared to secondary batteries. There are various kinds of supercapacitor: electric double layer capacitors with a relatively long history, pseudocapacitors that utilize electrochemical reactions, and the progress of hybrid capacitor technology that combines double layer capacity and electrochemical reactions. Development of electrode materials and electrolytes and new cell design for constructing devices support the performance improvement and expansion of new applied fields such as automobiles, heavy machinery, and energy harvesting. This book aims to provide engineers with the opportunity to review the latest information by integrating cutting-edge papers on the science, technology, and the application of supercapacitors.

The first chapter reviews the properties of carbon nanomaterials such as activated carbon, graphene, and carbon nanotubes. The author evaluates the current state of carbon nanomaterials and their composite materials for supercapacitor applications and describes future prospects (Khalid et al.). Chapters 2 and 3 focus on device flexibility and introduce the latest material technologies for developing wearable supercapacitors (Shanov et al.). In the fourth chapter, a constant voltage charge test is performed using a conventional electric double layer capacitor, and the relationship between the applied voltage and the deterioration behavior of the capacitor is considered from a practical point of view (Tashima). Chapter 5 explains the lithium doping method, which can increase cell capacity while maintaining the output and cycle characteristics of the capacitor. The author discusses the lithium ion hybrid capacitor, which has attracted attention in the field of capacitor technology (Sun et al.). In Chapters 6 and 7, two authors introduce high-capacity pseudocapacitors by using metal oxide nanomaterial and chromium nitride as electrode materials (Das et al. and Singh et al.). In the last chapter, the authors explain the application of supercapacitors to hybrid buses by drawing a realistic solution related to the controlling method for capacitor and power train based on precise energy efficiency calculation and simulation (Wang et al.).

Takaya Sato
National Institute of Technology,
Tsuruoka College,
Japan



Section 1

Science and Technology of Supercapacitors



Carbon-Based Composites for Supercapacitor

Mohmmad Khalid, Prerna Bhardwaj and Hamilton Varela

Abstract

Supercapacitor is an emerging technology that promises to play an advance role in new generation electronic devices and systems. Carbon (activated carbon, graphene and carbon nanotube) have attracted tremendous attention for their potential applications in supercapacitor technologies due to their excellent mechanical strength, good electrical conductivity, high electron mobilities, excellent chemical stability in acidic and basic medium, good thermal stability in wide range of temperature, various morphological structures, and large specific surface area. This chapter aims to assess the current status of carbon nanomaterials and their composites for supercapacitor application by discussing the literature in this field and presenting a perspective for future research in supercapacitor technologies.

Keywords: carbon nanomaterial, mesoporous carbon, graphene, carbon nanotube, composite, supercapacitor

1. Introduction

The ever-growing need for energy because of continuous depletion of fossil fuels and associated increasing air pollution, has caused the urge of developing sustainable and clean energy sources. Renewable energy sources like solar and wind energy systems are intermittent in nature and do not show potential impact unless the effective energy storage system is connected. Though, traditional batteries are used to store the electricity produced by renewable sources, their toxic components and high cost have precluded them from wide adoption in modern technologies. The traditional capacitors which are made of two metal plates separated by dielectric materials show very little tendency to store energy as the batteries store. One of the latest energy storage systems is supercapacitor. It is an emerging technology that promises to play pivotal role in laying out the roadmap of energy storage system for future. Supercapacitor technology provides a bridge between traditional capacitors and batteries, where supercapacitors could store greater amount of energy than the conventional capacitor and are able to deliver more power than existing batteries. Energy in supercapacitors is directly related to the capacitance of the electrode, which can be boosted by developing highly porous carbon or by introducing pseudocapacitive materials into the carbon network. By this way, the energy storage capability of the supercapacitor electrodes can be increased at much high level than traditional capacitors. Besides having high power capability than batteries, their charge storing and charge releasing mechanism is efficiently reversible, so they are extremely promising candidates with long charge/discharge life. However, their energy storing capacity is still far behind

than the traditional batteries [1–5]. Therefore, there is a huge interest in increasing the energy density of supercapacitors. Almost all worldwide supercapacitor companies such as NESSCAP, Panasonic, AVX Maxwell and NEC use activated carbon as active material for the construction of commercial supercapacitors. However, progress in the development of other allotropes of carbon like graphene, carbon nanotube and other materials such as metal oxides and conducting polymers are continuing at a steady rate in supercapacitor applications. In order to boost the performance of supercapacitor, introduction of the pseudocapacitance in double-layer capacitive electrode seems to be a prevalent target amongst the current research and offers a good chance of developing the next generation high performance supercapacitor. The construction of a supercapacitor is slightly different from that of traditional capacitor, where electrolyte is the conductive connection between two electrodes unlike conventional capacitors [6]. These electrodes are polarized by applying suitable potential in the same way that batteries are polarized. The polarity of the supercapacitor electrodes is controlled by designing the supercapacitor assembly in the form of asymmetrical or symmetrical systems. Asymmetric supercapacitors, where positive and negative electrodes are different from each other, while, in case of symmetric supercapacitor both electrodes are consisted with the same materials in identical shape and size of the electrodes. The voltage of the supercapacitor devices in asymmetrical manner enhances by taking the advantage of the potential ends of two different electrodes. If the both electrode are same as in case of symmetrical supercapacitor design, the total value of capacitance is roughly half that of one electrode. On the basis of charge storage mechanism of the electrodes, supercapacitor can be divided into three types (**Figure 1**): (1) electrical double layer capacitors (EDLCs)—generally high surface area carbon materials and its derivatives are used for making electrodes, where ions are adsorbed on the surface of electrodes in the form of electric double layers (Helmholtz layer), one electrode collects positive ions and other is mirrored with opposite negative ions,

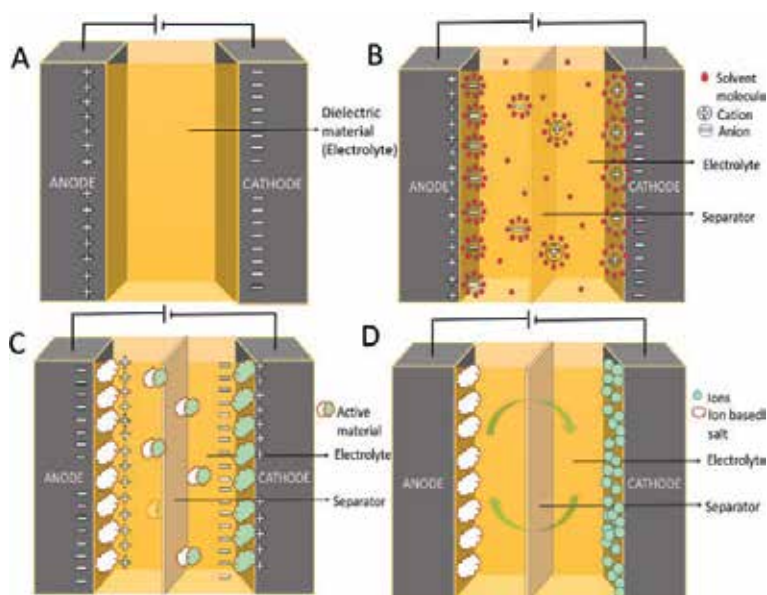


Figure 1. Schematic representation of (A) traditional capacitor; (B) electrical double layer capacitor; (C) pseudocapacitor and (D) hybrid supercapacitor [7].

therefore the total capacitance value of a double layer capacitor is the result of two capacitors connected in series, (2) pseudocapacitors—metal oxides and conducting polymers are used for fabrication of the electrodes, where redox (Faradaic) reactions occurs at the interface of electrode surface and electrolyte, It should also be noted that the suitable potential should be selected for the pseudocapacitive electrode materials, beyond the suitable potential window electrode will be degraded, and (3) hybrid supercapacitor—where electrodes are constructed using the significant features of both EDLC and pseudocapacitors, the most promising outputs seem to lie in the use of hybrid supercapacitors, which consists of carbon material and metal oxides/conducting polymer [8]. **Figure 1** demonstrates the schematic illustration of traditional capacitor, EDLC, pseudocapacitor and hybrid supercapacitor.

The fundamental equation (Eq. (1)) governing the capacitance of a traditional capacitor also stands for supercapacitors.

$$\text{Capacitance, } C = \epsilon_0 \epsilon_r A_e / d \quad (1)$$

Where ϵ_0 is the permittivity of free space, ϵ_r is the relative permittivity, A_e is the surface area of the electrodes and d is the distance between them [9]. Hence, if we could increase the area of electrodes and decrease the distance between them then the capacitance will be improved.

Therefore, in order to choose an electrode material for a supercapacitor [10, 11] the following factors should be taken into account, i.e.,

- The specific surface area of the electrodes.
- Pore size distribution.
- The conductivity of the electrodes.
- The resistance to any oxidation/reduction on the surface of the electrode.
- Electrochemical stability of the electrolyte in the operating voltage.
- Resistance of the electrolyte towards electrode.
- Wettability of the electrolyte on the electrode.

In this chapter, we will focus on the advancement in research concerning use of carbon nanomaterials in developing supercapacitors.

2. Carbon nanomaterials

Carbon is one of the most abundant materials in nature. Thus, it is thought to be an economical choice for employing in energy conversion and storage technologies. Owing to the excellent mechanical strength, good electrical conductivity, high electron mobility, high chemical stability, large surface area and high tunable properties make carbon materials an ideal candidate for energy storage systems. Some of the common carbon materials which fulfill majority of the desired properties to act as an effective and efficient electrode for supercapacitors are—activated carbon, graphene and carbon nanotubes (CNTs).

2.1 Activated carbon

The basic properties of activated carbon (AC), i.e., low cost, high electrical stability and large surface area makes them most common materials used in commercial supercapacitors. ACs are generally produced by physical (thermal) and/or chemical activation of raw materials with high carbon content like coal, wood, etc. The physical activation is carried out by heating the raw material in absence of atmospheric air at very high temperatures, usually in the range 700–1200°C. The chemical activation process requires heating of carbon resource at a lower temperature of 400–700°C in presence of an activating agent such as zinc chloride, phosphoric acid, sodium hydroxide and others [12]. These two processes results in activated carbon with a high surface area (3000 m²/g) but with a pore size distribution in a wide range of macro-pores, mesopores and micropores (>50–2 nm) [13, 14]. The micropores are in general considered to be inaccessible for electrolyte ions thus not capable of supporting an electrical double layer. The mesopores have maximum contribution towards capacitance in an electrical double layer capacitor followed by micropores [15–17]. As discussed above, EDLC and pseudocapacitance both are surface phenomena, thereby, activated carbon with high surface area are perfect candidates for application as electrode material [12]. However, the experimental value of capacitance for activated carbon-based supercapacitor were found to be in the range 1–10 μF/cm² which is lower than the theoretical calculations [18]. This has been explained in detail by Kierzek et al. [19] and found that the surface area of the electrode material is not the only factor that determines performance of the electrode. There are other parameters which need to be considered for calculating capacitance for instance; shape, structure and size distribution of the pores along with the electrical conductivity and wettability of electrode in the particular electrolyte [12]. This gave birth to a new concept, i.e., use of mesoporous carbon (pore size 2–50 nm) for supercapacitor applications, which contributes in easy ion-transport over the conventional activated carbon and hence, demonstrates high power capability [20]. Fernández et al. [21] synthesized mesoporous carbon by carbonizing a mixture of poly(vinyl alcohol) and inorganic salt and showed a specific capacitance of about 180 F/g in aqueous H₂SO₄ electrolyte. The performance of mesoporous carbons can be further enhanced by controlled introduction of micropores. Xia et al. [22] showed that a specific balance between mesopores to micropores ratio can tune the specific capacitance to 223 F/g in 6 M KOH electrolyte at 2 mV/s scan rate with 73% retention cyclability. This improved capacitance has been attributed to the presence of hierarchical porous structure of the electrode material that consists interconnected micropores and mesopores, having the high surface area of 2749 m²/g, and large pore volume of 2.09 cm³/g. The interconnected porous structure facilitates the easy movement of ions. The performance of mesoporous carbon can also be improved by its functionalization. The functionalized mesoporous carbon can then act as an efficient pseudocapacitor electrode in addition to EDLC. Different functional groups like –OH, –COOH or –C=O can be easily introduced by activating the mesoporous carbon using strong acids like nitric acid, sulfuric acid or ammonium persulfate. For example, Jia et al. [23] pyrolyzed the mixture of milk powder and sodium hydroxide without any substrate resulting in the formation of N-doped mesoporous carbon which showed a high capacitance of 396.5 F/g at 0.2 A/g in the electrolyte solution of H₂SO₄ along with high stability in their capacitance value (95.9% capacitance retention after 2000 cycles at 50 mV/s). Ren et al. [24] have also observed that the capacitance of mesoporous carbon increased from 117 to 295 F/g (10 mV/s scan rate) after its treatment with nitric acid. **Table 1** summarize some carbon-based electrical double layer supercapacitors.

Electrode	Electrolyte (M)	Specific capacitance (F/g)	Current density	Retention capacity	Refs.
Layered NOMC	H ₂ SO ₄ (0.5)	810	1.0 A/g	50,000 cycles between 0 and 1.2 V	[25]
	Li ₂ SO ₄ (2.0)	710	1.0 A/g		
Ordered NOMC	H ₂ SO ₄	262	0.5A/g		[26]
	KOH	227			
hierarchically porous NOMC	H ₂ SO ₄ (0.5)	537	0.5A/g	10,000	[27]
NOMC from phenol-urea-formaldehyde	Ionic Liquid	225	0.5 A/g	1000	[28]
NOMC from aqueous assembly	Ionic liquid	186	0.25 A/g	—	[29]
N-doped micro-mesoporous carbon	KOH (6.0)	226	1.0 A/g	2000	[30]
NOMC		288	0.1 A/g	25,000	[31]

NOMC, nitrogen-doped mesoporous carbon.

Table 1. Summarizes some of the studies carried out by different research groups on capacitance values of N-doped mesoporous carbon materials.

Incorporation of heteroatoms such as nitrogen, boron, phosphorous, and sulfur (N, B, P, and S) into the carbon network by replacing some carbon atoms offers a significant change in the electronic, electrical, and surface charges properties of the carbon materials. Doping of heteroatom in carbon materials can be done either by in situ preparation of carbon or through post-treatment by heteroatom containing precursor. In particular, nitrogen doping has gained more attention in supercapacitor, because nitrogen doping not only improves the electrical conductivity and wettability but also contribute additional pseudocapacitance by enhancing the surface polarity and electron donor affinity of carbon. According to the studies made by Wang et al. [31], nitrogen doping facilitates the formation of well-defined mesopores and resulted improved electrochemical performance. Lin et al. [25] developed N-doped mesoporous few-layer carbon with a large surface area of 1900 m²/g for supercapacitor. It was reported that the as-developed few layer carbon showed highest ever specific capacitance of 810 F/g in three-electrode cell and 710 F/g in full cell at 1 A/g in 0.5 M H₂SO₄ and 2 M Li₂SO₄ electrolytes. The full cell device showed high stability with 50,000 repeating cycles between 0 to 1.2 V, and demonstrated highest specific energy of 23.0 W h/kg while maintaining the specific power density of 18.5 kW/kg in 2 M Li₂SO₄ electrolyte. However, the exact mechanism has not yet been confirmed but it is evident that the pyrrolic N, pyridinic N or quaternary N plays a crucial role in determining the ion flow towards the electrode, hence, influencing the capacitance of the electrode [32]. Nitrogen and phosphorus dual doped mesoporous carbon was also prepared, which reveals a high specific capacitance of 220 F/g at a current density of 1 A/g with excellent rate capability of 91% in a 6 M KOH aqueous electrolyte [33]. This value of capacitance was found lower than nitrogen and sulfur or nitrogen and oxygen dual doped mesoporous carbon synthesized using polyhedral oligosilsesquioxanes, which showed almost rectangular cyclic voltammogram curve in wide potential window from -2 to +2 V in ionic liquid electrolyte. These electrode materials showed a gravimetric and volumetric specific capacitance of 163 F/g and 106 F cm⁻³ at a current density of 0.25 A/g [34].

Another form of activated mesoporous carbon is the carbon nanofibers. The ease of preparation and highly mesoporous structure of these fibers exhibited excellent electrode material for electrochemical double layer capacitors [35]. Xu et al. [36] prepared polyacrylonitrile fibers followed by NaOH activation, and observed high specific capacitance of 371 F/g in the aqueous KOH (6 M), 213 F/g in non-aqueous LiClO₄ (1 M) and 188 F/g in ionic liquid electrolyte solutions. Mesoporous carbons have also been extensively studied in the form of composites with other active materials, including conductive polymers (polyaniline [37], poly3-hexylthiophene) and metal oxides (Manganese oxide MnO₂ [38, 39], Ruthenium oxide RuO₂ [11]). In particular, pristine conducting polymers with their excellent electrochemical properties have displayed capacitance 10–100 times higher than EDLCs but they suffer from some limitations like poor stability and short lifetime. Thus, combining the properties of conducting polymers with mesoporous carbon can result in an electrode material with optimum properties. For instance, chemical polymerization of polyaniline onto an ordered bi-modal-mesoporous carbon resulted in the formation of PANI nanowires growing out of mesoporous carbon substrate has been reported by Yan et al. [40]. The subsequent composite exhibited a specific capacitance of 517 F/g in 1 M H₂SO₄ electrolyte with 91.5% retention rate after 1000 cycles. Chen et al. have presented a facile synthesis of highly porous N-doped carbon nanofibers coated with polypyrrole by carbonization which showed a specific capacitance of 202 F/g in aqueous KOH (6 M) electrolyte at a current density of 1 A/g. It exhibited maximum power density of 90 kW/kg while maintaining high capacitance retention and cyclability. This kind of N-doped carbon nanofiber-based composites exemplifies unconventional and practically potential candidates for a competent electrode material for supercapacitors [41].

2.2 Graphene

Since the discovery of graphene by Novoselov and Geim in 2004, the research on this flattish material has received enormous attention. This flat sheet is a one-atom-thick layer of sp²-bonded, 2D honeycomb lattice of carbon with a fully conjugated structure of alternating C–C and C=C bonds. Its unique physico-chemical properties make this material a promising candidate for a large variety of applications. However, the use of graphene for most of the electronic applications often requires precise functionalization of individual graphene sheets into various device elements at molecular level. Therefore, surface functionalization of graphene sheets is essential, and researchers have devised various covalent and noncovalent chemistries for making graphene materials with the bulk and surface properties needed for many potential applications including energy conversion and storage. Its high mechanical strength, excellent electrical and thermal conductivity and large theoretical surface area (2600 m²/g) make this material particularly interesting for energy-storing devices. The other forms of carbon allotropes like Fullerene (0-D), carbon nanotubes (1-D) and graphite (3-D), all resemble the graphene hexagonal ring structure of graphene with different orientations in space, and each of these structures represent a unique property of its own [42]. Graphene, despite having exclusive physical and chemical properties and high theoretical surface area, it is not free from some drawbacks. The major drawback is of its sheet to sheet restacking (due to strong π - π interactions between its layers), which reduces the effective surface area rendering it nonfunctional for its application as multidimensional flexible electrode material. In order to overcome these shortcomings, constructive experiments have been made to fabricate nanoporous graphene by intercalation of other nanoparticles in graphene layers. Efforts are also being made to utilize the surface defects of crystal lattice structure of host material originated during

chemical synthesis for immobilization of electrolyte ions. In general, graphene activation can be achieved by methods like; introducing spacers between its layers, exfoliation method, templating technique or forming hydrogel by reducing graphene oxide. Thus, for application purposes graphene is not used as pristine but it has to be employed as reduced graphene oxide or activated graphene or doped graphene or graphene/metal oxide composites or graphene/polymer composites [43]. For instance, Zhang et al. [44] pioneered a new carbon material by chemical modification of one-atom thick layer of graphene (specific surface area $705 \text{ m}^2/\text{g}$), which demonstrated high specific capacitance values of 135 F/g in aqueous electrolyte and 99 F/g in organic electrolyte. In addition, it showed good retention ability over a wide range of voltage scan rates. Another group led by Vivekchand et al. [45] have reported the synthesis of graphene using thermal exfoliation of graphitic oxide at very high temperature of 1050°C . The product obtained had a high surface area of $925 \text{ m}^2/\text{g}$ and specific capacitance is 117 F/g in aqueous H_2SO_4 electrolyte. On the other hand, functionalization of graphene can also be achieved by controlled thermal exfoliation at low temperatures [46] without compromising its capacitance performance. Chemical functionalization of graphene oxide platelets grown on an intrinsically flexible, highly porous and ordered carbon films by nitrogen doping [47] has shown to enhance its electrical as well as supercapacitive properties. All the above-mentioned activation methods have led to the production of materials with high capacitance but for real-life practical application of these materials, another important factor to be considered is energy density. The commercially available batteries have higher energy density than supercapacitors. This means that supercapacitors can provide a very high energy pulse when required but can store less energy per unit weight, as compared to batteries. Liu et al. [48] have demonstrated the synthesis of 1-layer graphene in a curved form which restricted the face to face restacking of its sheets, hence, utilizing maximum possible electrode surface. This resulted in supercapacitor electrode material with very high specific energy density of 86 and 136 Wh/kg at room temperature and 80°C respectively at 1 A/g current density. Xu et al. [49] have also described the development of sponge-like graphene nanostructures that showed high energy density of 48 kW/kg . A new approach to efficiently exploit the surface of each layer of graphene structure is by employing the “in-plane” strategy in place of stacking [50]. In case of conventional (stacked) assembly, the entire electrochemical (specific) surface area cannot be used as some of the regions are unapproachable to the electrolyte ions (**Figure 2a**). Whereas the new structural design assists the percolation of electrolyte ions between graphene layers to reach the current collector. Consequently, facilitating the maximum usage of available specific surface area [50]. This type of in-plane 2D graphene supercapacitor has shown a maximum specific capacitance value of 250 F/g at current density 176 mA/g with good retention rate for 1500 cycles.

2.2.1 Graphene/metal-oxide composites

Variety of metal-oxides such as RuO_2 , MnO_2 , NiO , Fe_3O_4 , ZnO , TiO_2 , etc. have been explored for possible electrode material in supercapacitors. These so called active material, when added in an appropriate quantity to the graphene structure can result in excellent electrode material. The addition of metal oxide nanoparticle acts as nanospacers between the graphene layers to prevent its restacking. On the other hand, the flexible space between the 2-D graphene sheets provides a smooth horizontal way for the mobility of electrolyte ions improving its energy storing capacity. Lu et al. [51] have described the supercapacitor behavior of graphene-ZnO and graphene- SnO_2 composite materials. They found that electrochemical performance of graphene-ZnO composite was improved to a great extent in terms of capacitance

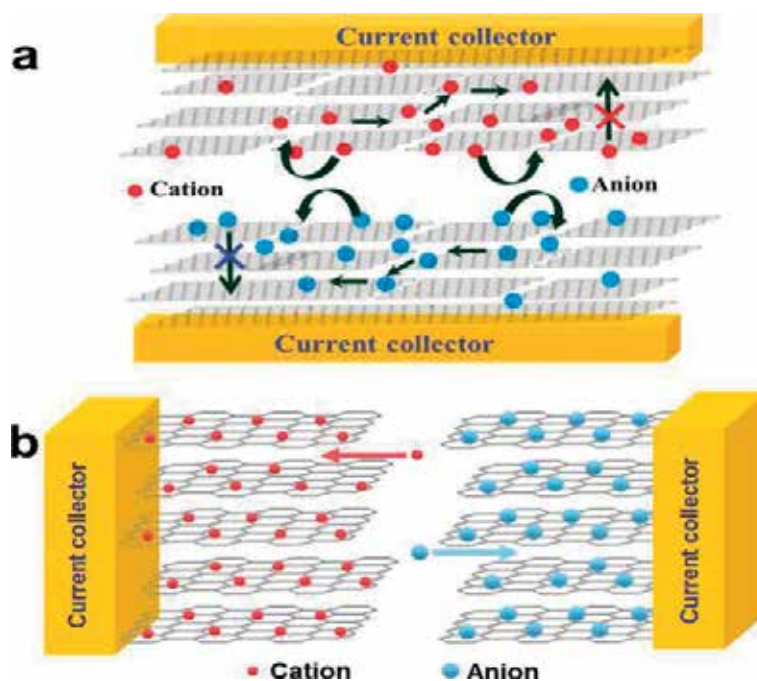


Figure 2.

Schematic depiction of the (a) stacked geometry where all graphene layers are parallel to the current collectors, (b) operating principle in case of the in-plane supercapacitor device utilized for the performance evaluation of graphene as electrodes. Reproduced with permission from Ref. [50]. Copyright (2011) to American Chemical Society.

value and reversibility when compared to pristine ZnO or SnO₂ or graphene. Its specific capacitance was 61 F/g and energy density of 4.8 Wh/kg, which was also greater than that of graphene-SnO₂ samples. Graphene-MnO₂ composite with high MnO₂ content (78 wt.%) demonstrates a specific capacitance of 310 F/g at a scan rate of 2 mV/s. The authors claim that hybridization of graphene and MnO₂ caused increase in specific surface area resulting in higher conductivity and eventually high-performance rate [52]. Apart from conventional symmetric supercapacitors (using same material for both electrodes), a number of studies have been carried out to exploit the potential of asymmetric supercapacitors (using different material for each electrode) based on metal oxide/graphene composites [53]. The objective for fabrication of asymmetric supercapacitors is to obtain a higher energy density. The most vital step in its assembly is the choice of two such electrodes, which have same working potential range and sufficient wettability in the same electrolyte. The use of asymmetric model for supercapacitor allows the extension of operating potential window along with the improved capacitance performance rate. For example, Cao et al. [54] have established that an asymmetric supercapacitor developed using MnO₂ nanoparticles as anode and graphene as cathode exhibits a specific capacitance of 37 F/g and could operate up to voltage range of 2.0 V with 96% capacitance retention for 500 cycles. It displayed much higher energy density of 25.2 Wh/kg and power density of 100 W/kg when compared to 4.9 Wh/kg (MnO₂/MnO₂) and 3.6 Wh/kg (graphene/graphene) based symmetric supercapacitors.

2.2.2 Graphene/conducting polymer composites

The composites made from graphene and electrically conductive polymers [polyaniline, polythiophene, polypyrrole, poly(3,4-ethylenedioxythiophene)] have

attracted great deal of attention. The flexible and conductive nature of conductive polymers when combined with the intrinsic layered structure of graphene results in a material with potential for electrode application in supercapacitors. The increasing need for lightweight, flexible and smaller size supercapacitors in future electronics world has stimulated the interest in such graphene/polymer composite electrodes. These composites have improved mechanical strength and conductivity as compared to each material individually. They have been successfully implied in other applications like solar cells, fuel cells, transparent electrodes, etc.

The synthesis of graphene/polymer composite is facile and cost effective. Anodic in-situ polymerization of aniline on the graphene layered structure has been reported by Wang et al. [55]. The product formed was flexible, self-standing, strong and electrochemically stable. It showed a high electrochemical capacitance of 233 F/g at 2 mV/s scan rate with good stability for 2000 reversible cycles. The 2D structure of graphene can also be used to grow 1D nanorods of conductive polymer [56]. This represents an opportunity to utilize the maximum available surface area, hence, enhancing the energy storing capacity of the electrode. For example, graphene/polyaniline nanorod composite showed very high specific capacitance of 555 F/g in 1 M H₂SO₄ electrolyte with cyclic stability of 2000 cycles [57]. Some graphene and conducting polymer based composites have been listed in the **Table 2**. It is evident from the capacitance values in the table: that compositing conducting polymer with graphene convalesces its capacitance performance rate. However, this process may also lead to increase in the π - π stacking of graphene layer which in turn lowers the specific surface area of electrode. Therefore, there is a need to develop techniques for constructing 3-D structures of polymer matrix and introducing 1-D layer of graphene into it to avoid layer restacking.

2.3 Carbon nanotubes

Carbon nanotubes (CNTs) are quasi 1D nanomaterial formed by rolling one or more sheets of graphene concentrically. They have a unique cylindrical structure

Electrode material	Electrolyte (M)	Capacitance (F/g)	Current density	Retention cycle	Refs.
Graphene/Ppy	LiClO ₄ (0.1)	1510	—	—	[58]
GNS/PANI	H ₂ SO ₄ (1)	1130	—	1000	[59]
Graphene/PANI	H ₂ SO ₄ (1)	1126	—	1000	[60]
rGO/PANI	H ₂ SO ₄ (0.5)	970	2.5 A/g	1700	[61]
PANI/Graphene	HClO ₄ (1)	878	1.0 A/g	1000	[62]
GO/PANI	H ₂ SO ₄ (1)	746	0.2 A/g	500	[63]
Graphene/PANI	H ₂ SO ₄ (1)	640	0.1 A/g	1000	[64]
Graphene/PANI	H ₂ SO ₄ (2)	526	0.2 A/g	—	[65]
G-doped PANI	H ₂ SO ₄ (1)	531	0.2 A/g	—	[66]
GO-Ppy	H ₂ SO ₄ (1)	510	0.3 A/g	—	[67]
Graphene/PANI	H ₂ SO ₄ (2)	480	0.1 A/g	1000	[68]
Graphene/ Ppy	H ₂ SO ₄ (1)	420	0.5 A/g	200	[69]
Graphene/PEDOT	H ₂ SO ₄ (2)	342	0.02 A/g	—	[70]

Table 2.
 Some graphene and conducting polymer based composites and their capacitances.

with few micrometer length and diameter in the range of nanometers. CNTs are typically classified as single-walled (SW), double-walled (DW), or multi-wall (MW), corresponding to the number of graphene layers forming CNTs. The very first CNT was formally reported in 1991 by Iijima, when he closely observed the structure of carbon-soot obtained by an arc-discharge method using TEM technology [71, 72]. Since then, both SWCNTs and MWCNTs have been extensively studied for their numerous possible applications. The presence of hexagonal lattice structure of graphene with sp^2 bonded carbon atoms in CNTs contributes to its excellent properties like electrical and thermal conductivity, high mechanical strength, optimum chemical stability and low mass per unit volume [73]. In terms of tensile strength, CNTs are hundred times tougher than steel. They have Young's modulus of about 1.2 TPa (1 TPa for SWCNTs and 1.28 TPa for MWCNTs) and can withstand large strains before mechanical failure. The electrical conductivity of CNTs depends on their structure, i.e., MWCNTs with concentric tubular structure having inter-layer distance of about 0.34 nm shows metallic conductivity. Whereas, the SWCNTs have shown both metallic or semiconducting behavior depending on their chirality and diameter size. CNTs have been successfully synthesized and employed in various application namely chemical sensors, field emission sources, nanotweezer, scanning microscope probe tip, electro-mechanical actuators, etc. CNTs have a large crosswise dimension (<1 , $1-2$, $2-5$, $5-10$, and >10 μm), high specific surface area (SWCNT > 1600 m^2/g , MWCNT > 430 m^2/g), and excellent carrier mobility for both ions and holes ($15,000$ cm^2/Vs) and are being widely used as the active electrode in supercapacitors [74]. This can be attributed to the fact that CNTs have high aspect ratio so they tend to get entangled and form a porous structure with nanotube network skeleton. It also creates a mesoporous open central canal in case of MWCNTs. This provides an easy pathway for the electrolyte ions to move freely between electrode/electrolyte during charge and discharge cycles. In order to minimize the size of supercapacitor-based power cell for its real-world application, it is important to work towards high power density electrodes. Niu et al. [75] have fabricated a supercapacitor based on MWCNTs, which showed a capacitance value of 102 F/g, high power density >8 kW/kg and an energy density of ~ 1 Wh/kg in H_2SO_4 electrolyte. They also showed that such electrode material did not require any binder and was self-sufficient. A supercapacitor based on SWCNT electrode as reported by An et al. [76] showed comparatively higher specific capacitance value of 180 F/g in KOH (7.5 M) electrolyte solution with power density of 20 kW/kg and energy density in the range 7–6.5 Wh/kg. Similar to other carbon materials, CNTs are also being more commonly used as its composite. CNT/conductive polymer composite have attained a lot of attention in terms of its capacitive applications as it combines high pseudocapacitance of conductive polymers with excellent mechanical properties of CNTs. They can be synthesized chemically or electrochemically. The electrochemical method involves either deposition of polymer on a CNT electrode, or co-deposition of polymer and CNT on electrode. The composites formed by electrochemical co-deposition are found to be most homogeneous. They show enhanced electron delocalization due to the presence of conjugated carbon chain and an unusual interaction between the polymer and CNTs. As a result, they exhibit excellent electrochemical charge storage properties and fast charge/discharge switching, making them promising electrode materials for high power supercapacitors.

2.4 Hybrid carbon materials

More recently, several attempts have been made to merge the unique properties of several carbon-based nanomaterials to form a hybrid material. For instance, Li

et al. [77] have reported synthesis of a flexible, light weight and self-standing film by combining activated carbon, CNT and reduced graphene oxide. The hybrid film is prepared by weaving 3D porous framework using CNTs and graphene that was further used to accommodate activated carbon particles using their intrinsic van der Waals force. In such a material, each component has an important role to play like carbon particles block the restacking of graphene structure and the CNTs improve electronic conductivity. The AC/CNT/rGO electrode thus formed showed a specific capacitance of 101 F/g in organic electrolyte at 0.2 A/g current density with a maximum energy density of 30 Wh/kg. Supercapacitors, are generally known to work only in a narrow temperature range. However, a flexible hybrid film consisting of CNTs and rGO has been reported to be able to operate between the temperature range -40 and 200°C . The electrode material exhibited a maximum area specific capacitance of 330 mF/cm^2 with energy density of 1.7 mWh/cm^3 and 90% retention even after 100,000 cycles [78]. More interestingly, CNTs were intercalated between graphene sheets to retain high specific surface area by minimizing its aggregation [79], where π - π interaction between graphene sheets and CNTs also improve the electrical conductivity and mechanical strength. Similarly, Yu and Dai produced hybrid films of CNT and graphene interconnected network with well-defined nanoporous structure [80], which exhibited a specific capacitance of 120 F/g in 1 M H_2SO_4 electrolyte and an almost rectangular cyclic voltammogram even at high scan rate of 1 V/s. Yu et al. developed a continued CNT and graphene hybrid fiber with well-defined mesoporous structure [81], which showed specific surface area as high as $396\text{ m}^2/\text{g}$ with an electrical conductivity of 102 S/cm. The corresponding fiber-shaped supercapacitor demonstrate a volumetric specific capacitance of 305 F/cm^3 at 26.7 mA/cm^3 current density and a volumetric energy density of 6.3 mWh/cm^3 , which is comparable to the energy density of a 4 V-0.5 mAh thin-film lithium ion battery.

3. Summary and perspective

Carbon has already made a revolution in the world. Now its surface engineering with variety of functional materials and nanoporous structure are the fascinating parts of the research. In the light of the aforementioned studies, a broad range of carbon nanomaterials with various dimensions and unique morphological structure designs have been made and successfully implemented in energy storage device fabrication technologies. The incorporation of heteroatoms into the carbon network provides a new class of carbon materials with unique properties unmatched with parental carbon materials. Compositing carbon nanomaterials with metal oxides/ conducting polymers having pseudocapacitance increases energy density largely but compromise with rate capability and cycling life. In this chapter, we have thoroughly conferred the recent progress of carbon nanomaterials based supercapacitors. The potential of carbon nanomaterials and its composites for supercapacitors is in resolving the foreseen of clean energy mitigation. Various materials, methods and technologies have been employed in finding a solution for an energy storing device with high capacitance along with high energy/power density. No doubt, carbon materials are potential candidates for supercapacitor electrode materials but they need a supporting active material to enhance their performance. Nevertheless, increase in specific capacitance value, power density and energy density in certain cases gives a hope that if the research continues in right direction then one-day carbon material based supercapacitor can bring a new revolution in the electronic world. We are confident that the information presented in this chapter would definitely help in the research and development of carbon nanomaterials based supercapacitors.

Acknowledgements

Authors would like to place on record thanks to the São Paulo Research Foundation (FAPESP) for financial support under ongoing projects of Grant No. 2017/00433-5 and Grant No. 2013/16930-7.

Author details


Mohmmad Khalid^{1*}, Prerna Bhardwaj² and Hamilton Varela¹

1 Institute of Chemistry of São Carlos, University of São Paulo, São Carlos, SP, Brazil

2 Department of Chemistry, Panjab University, Chandigarh, India

*Address all correspondence to: mkansarister@gmail.com

IntechOpen

© 2018 The Author(s). Licensee IntechOpen. This chapter is distributed under the terms of the Creative Commons Attribution License (<http://creativecommons.org/licenses/by/3.0>), which permits unrestricted use, distribution, and reproduction in any medium, provided the original work is properly cited. 

References

- [1] Kotz R, Carlen M. Principles and applications of electrochemical capacitors. *Electrochimica Acta*. 2000;**45**:2483-2498. DOI: 10.1016/S0013-4686(00)00354-6
- [2] Sher HA, Addoweesh KE. Power storage options for hybrid electric vehicles—A survey. *Journal of Renewable and Sustainable Energy*. 2012;**4**:052701. DOI: 10.1063/1.4759457
- [3] Gidwani M, Bhagwani A, Rohra N. Supercapacitors: The near future of batteries. *International Journal of Engineering Inventions*. 2014;**4**:22-27
- [4] Winter M, Brodd RJ. What are batteries, fuel cells, and supercapacitors? *Chemical Reviews*. 2004;**104**:4245-4270. DOI: 10.1021/cr020730k
- [5] Turner JA. A realizable renewable energy future. *Science*. 1999;**285**:687-689. DOI: 10.1126/science.285.5428.687
- [6] Zuo W, Li R, Zhou C, Li Y, Xia J, Liu J. Battery-supercapacitor hybrid devices: Recent progress and future prospects. *Advanced Science*. 2017;**4**:1600539-1600550. DOI: 10.1002/advs.201600539
- [7] Chen X, Paul R, Dai L. Carbon-based supercapacitors for efficient energy storage. *National Science Review*. 2017;**4**:453-489. DOI: 10.1093/nsr/nwx009
- [8] Chen T, Dai L. Carbon nanomaterials for high performance supercapacitors. *Materials Today*. 2013;**16**:272-280. DOI: 10.1016/j.mattod.2013.07.002
- [9] Zhai Y, Dou Y, Zhao D, Fulvio PF, Mayes RT, Dai S. Carbon materials for chemical capacitive energy storage. *Advanced Materials*. 2011;**23**:4828-4850. DOI: 10.1002/adma.201100984
- [10] Notarianni M, Liu J, Vernon K, Motta N. Synthesis and applications of carbon nanomaterials for energy generation and storage. *Beilstein Journal of Nanotechnology*. 2016;**7**:149-196. DOI: 10.3762/bjnano.7.17
- [11] Sugimoto W, Yokoshima K, Murakami Y, Takasu Y. Charge storage mechanism of nanostructured anhydrous and hydrous ruthenium-based oxides. *Electrochimica Acta*. 2006;**52**:1742-1748. DOI: 10.1016/j.electacta.2006.02.054
- [12] Zhang LL, Zhao XS. Carbon-based materials as supercapacitor electrodes. *Chemical Society Reviews*. 2009;**38**:2520-2531. DOI: 10.1039/b813846j
- [13] Qu D, Shi H. Studies of activated carbons used in double-layer capacitors. *Journal of Power Sources*. 1998;**74**:99-107. DOI: 10.1016/S0378-7753(98)00038-X
- [14] Raymundo-Piñero E, Kierzek K, Machnikowski J, Béguin F. Relationship between the nanoporous texture of activated carbons and their capacitance properties in different electrolytes. *Carbon*. 2006;**44**:2498-2507. DOI: 10.1016/j.carbon.2006.05.022
- [15] Kastening B, Spinzig S. Electrochemical polarization of activated carbon and graphite powder suspensions: Part II. Exchange of ions between electrolyte and pores. *Journal of Electroanalytical Chemistry*. 1986;**214**:295-302. DOI: 10.1016/0022-0728(86)80104-8
- [16] Mayer ST, Pekala RW, Kaschmitter JL. The aerocapacitor: An electrochemical double-layer energy-storage device. *Journal of the Electrochemical Society*. 1993;**140**:446-451. DOI: 10.1149/1.2221066

- [17] Tanahashi I, Yoshida A, Nishino A. Electrochemical characterization of activated carbon-fiber cloth polarizable electrodes for electric double-layer capacitors. *Journal of the Electrochemical Society*. 1990;**137**:3052-3057. DOI: 10.1149/1.2086158
- [18] Conway BE. *Electrochemical Supercapacitors*. New York: Plenum Publishing; 1999. DOI: 10.1007/978-1-4757-3058-6
- [19] Kierzek K, Frackowiak E, Lota G, Gryglewicz G, Machnikowski J. Electrochemical capacitors based on highly porous carbons prepared by KOH activation. *Journal of Electrochimica Acta*. 2004;**49**:515-523. DOI: 10.1016/j.electacta.2003.08.026
- [20] Li W, Liu J, Zhao D. Mesoporous materials for energy conversion and storage devices. *Nature Reviews Materials*. 2016;**1**:16023. DOI: 10.1038/natrevmats.2016.23
- [21] Fernández JA, Morishita T, Toyoda M, Inagaki M, Stoeckli F, Centeno TA. Performance of mesoporous carbons derived from poly(vinyl alcohol) in electrochemical capacitors. *Journal of Power Sources*. 2008;**175**:675-679. DOI: 10.1016/j.jpowsour.2007.09.042
- [22] Xia K, Gao Q, Jiang J, Hu J. Hierarchical porous carbons with controlled micropores and mesopores for supercapacitor electrode materials. *Carbon*. 2008;**46**:1718-1726. DOI: 10.1016/j.carbon.2008.07.018
- [23] Jia S, Wang Y, Xin G, Zhou S, Tian P, Zang J. An efficient preparation of N-doped mesoporous carbon derived from milk powder for supercapacitors and fuel cells. *Electrochimica Acta*. 2016;**196**:527-534. DOI: 10.1016/j.electacta.2016.02.196
- [24] Ren TZ, Liu L, Zhang Y, Yuan ZY. Nitric acid oxidation of ordered mesoporous carbons for use in electrochemical supercapacitors. *Journal of Solid State Electrochemistry*. 2013;**17**:2223-2233. DOI: 10.1007/s10008-013-2088-1
- [25] Lin T, Chen IW, Liu F, Yang C, Bi H, Xu F, et al. Nitrogen-doped mesoporous carbon of extraordinary capacitance for electrochemical energy storage. *Science*. 2015;**350**:1508-1513. DOI: 10.1126/science.aab3798
- [26] Wei J, Zhou D, Sun Z, Deng Y, Xia Y, Zhao D. A controllable synthesis of rich nitrogen-doped ordered mesoporous carbon for CO₂ capture and supercapacitors. *Advanced Functional Materials*. 2013;**23**:2322-2328. DOI: 10.1002/adfm.201202764
- [27] Han LN, Wei X, Zhu QC, Xu SM, Wang KX, Chen JS. Nitrogen-doped carbon nets with micro/mesoporous structures as electrodes for high-performance supercapacitors. *Journal of Materials Chemistry A*. 2016;**4**:16698-16705. DOI: 10.1039/C6TA05607E
- [28] Xie M, Xia Y, Liang J, Chen L, Guo X. Ordered nitrogen doped mesoporous carbon assembled under aqueous acidic conditions and its electrochemical capacitive properties. *Microporous and Mesoporous Materials*. 2014;**197**:237-243. DOI: 10.1016/j.micromeso.2014.06.024
- [29] Liu D, Zeng C, Qu D, Tang H, Li Y, Su BL, et al. Highly efficient synthesis of ordered nitrogen-doped mesoporous carbons with tunable properties and its application in high performance supercapacitors. *Journal of Power Sources*. 2016;**321**:143-154. DOI: 10.1016/j.jpowsour.2016.04.129
- [30] Chen A, Wang Y, Li Q, Yu Y, Li Y, Zhang Y, et al. Synthesis of nitrogen-doped micro-mesoporous carbon for supercapacitors. *Journal of the Electrochemical Society*.

2016;**163**:A1959-A1964. DOI:
10.1149/2.0711609jes

[31] Wang JG, Liu H, Sun H, Hua W, Wang H, Liu X, et al. One-pot synthesis of nitrogen-doped ordered mesoporous carbon spheres for high-rate and long-cycle life supercapacitors. *Carbon*. 2018;**127**:85-92. DOI: 10.1016/j.carbon.2017.10.084

[32] Rennie AJR, Hall PJ. Nitrogen-enriched carbon electrodes in electrochemical capacitors: Investigating accessible porosity using CM-SANS. *Physical Chemistry Chemical Physics*. 2013;**15**:16774-16778. DOI: 10.1039/C3CP52233D

[33] Feng J, Song W, Sun L, Xu L. One step nanocasting synthesis of nitrogen and phosphorous dual heteroatom doped ordered mesoporous carbons for supercapacitor applications. *RSC Advances*. 2016;**6**:110337-110343. DOI: 10.1039/C6RA22728G

[34] Liu D, Cheng G, Zhao H, Zeng C, Qu D, Xiao L, et al. Self-assembly of polyhedral oligosilsesquioxane (POSS) into hierarchically ordered mesoporous carbons with uniform microporosity and nitrogen-doping for high performance supercapacitors. *Nano Energy*. 2016;**22**:255-268. DOI: 10.1016/j.nanoen.2016.02.022

[35] Zhang L, Jiang Y, Wang L, Zhang C, Liu S. Hierarchical porous carbon nanofibers as binder-free electrode for high-performance supercapacitor. *Electrochimica Acta*. 2016;**196**:189-196. DOI: 10.1016/j.electacta.2016.02.050

[36] Xu B, Wu F, Chen R, Cao G, Chen S, Zhou Z, et al. Highly mesoporous and high surface area carbon: A high capacitance electrode material for EDLCs with various electrolytes. *Electrochemistry Communications*. 2008;**10**:795. DOI: 10.1016/j.elecom.2008.02.033

[37] Zhang K, Zhang LL, Zhao XS, Wu. Graphene/polyaniline nanofiber composites as supercapacitor electrodes. *Journal of Chemistry and Materials Research*. 2010;**22**:1392-1401. DOI: 10.1021/cm902876u

[38] Bahloul A, Nessark B, Briot E, Groult H, Mauger A, Zaghbi A, et al. Polypyrrole-covered MnO₂ as electrode material for supercapacitor. *Journal of Power Sources*. 2013;**240**:267-272. DOI: 10.1016/j.jpowsour.2013.04.013

[39] Yang ZC, Tang CH, Gong H, Li X, Wang J. Hollow spheres of nanocarbon and their manganese dioxide hybrids derived from soft template for supercapacitor application. *Journal of Power Sources*. 2013;**240**:713-720. DOI: 10.1016/j.jpowsour.2013.05.034

[40] Yan Y, Cheng Q, Zhu Z, Pavlinek V, Saha P, Li C. Controlled synthesis of hierarchical polyaniline nanowires/ordered bimodal mesoporous carbon nanocomposites with high surface area for supercapacitor electrodes. *Journal of Power Sources*. 2013;**240**:544-550. DOI: 10.1016/j.jpowsour.2013.03.190

[41] Chen LF, Zhang XD, Liang HW, Kong M, Guan QF, Chen P, et al. Synthesis of nitrogen-doped porous carbon nanofibers as an efficient electrode material for supercapacitors. *ACS Nano*. 2012;**6**:7092-7102. DOI: 10.1021/nn302147s

[42] Matte HSSR, Subrahmanyam KS, Rao CNR. Synthetic aspects and selected properties of graphene. *Nanomaterials and Nanotechnology*. 2011;**1**:3-13

[43] Huang Y, Liang J, Chen Y. An overview of the applications of graphene-based materials in supercapacitors. *Small*. 2012;**8**:1805-1834. DOI: 10.1002/smll.201102635

[44] Zhang LL, Zhao X, Stoller MD, Zhu Y, Ji H, Murali S, et al. Highly conductive and porous activated

reduced graphene oxide films for high-power supercapacitors. *Nano Letters*. 2012;**12**:1806-1812. DOI: 10.1021/nl203903z

[45] Vivekchand SRC, Rout CS, Subrahmanyam KS, Govindaraj A, Rao CNR. Graphene-based electrochemical supercapacitors. *Journal of Chemical Sciences*. 2008;**120**:9-13

[46] Du Q, Zheng M, Zhang L, Wang L, Chen J, Xue L, et al. Preparation of functionalized graphene sheets by a low-temperature thermal exfoliation approach and their electrochemical supercapacitive behaviors. *Journal of Electrochimica Acta*. 2010;**55**:3897-3903. DOI: 10.1016/j.electacta.2010.01.089

[47] Lee SH, Kim HW, Hwang JO, Lee WJ, Kwon J, Bielawski CW, et al. Three-dimensional self-assembly of graphene oxide platelets into mechanically flexible macroporous carbon films. *Angewandte Chemie*. 2010;**42**:10084-10088. DOI: 10.1002/anie.201006240

[48] Liu C, Yu Z, Neff D, Zhamu A, Jang BZ. Graphene-based supercapacitor with an ultrahigh energy density. *Nano Letters*. 2010;**10**:4863-4868. DOI: 10.1021/nl102661q

[49] Xu Z, Li Z, Holt CMB, Tan X, Wang H, Amirkhiz BS, et al. Electrochemical supercapacitor electrodes from sponge-like graphene nanoarchitectures with ultrahigh power density. *Journal of Physical Chemistry Letters*. 2012;**3**:2928-2933. DOI: 10.1021/jz301207g

[50] Yoo JJ, Balakrishnan K, Huang J, Meunier V, Sumpster BG, Srivastava A, et al. Ultrathin planar graphene supercapacitors. *Nano Letters*. 2011;**11**:1423-1427. DOI: 10.1021/nl200225j

[51] Lu T, Zhang Y, Li H, Pan L, Li L, Sun Z. Electrochemical behaviors of graphene-ZnO and graphene-SnO₂

composite films for supercapacitors. *Electrochimica Acta*. 2010;**55**:4170-4173. DOI: 10.1016/j.electacta.2010.02.095

[52] Yan J, Fan Z, Wei T, Qian W, Zhang M, Wei F. Fast and reversible surface redox reaction of graphene-MnO₂ composites as supercapacitor electrodes. *Carbon*. 2010;**48**:3825-3833. DOI: 10.1016/j.carbon.2010.06.047

[53] Deng L, Zhu G, Wang J, Kang L, Liu ZH, Yang Z, et al. Graphene-MnO₂ and graphene asymmetrical electrochemical capacitor with a high energy density in aqueous electrolyte. *Journal of Power Sources*. 2011;**196**:10782-10787. DOI: 10.1016/j.jpowsour.2011.09.005

[54] Cao J, Wang Y, Zhou Y, Ouyang JH, Jia D, Guo L. High voltage asymmetric supercapacitor based on MnO₂ and graphene electrodes. *Journal of Electroanalytical Chemistry*. 2013;**689**:201-206. DOI: 10.1016/j.jelechem.2012.10.024

[55] Liu Y, Shi K, Zhitomirsky I. Asymmetric supercapacitor, based on composite MnO₂-graphene and N-doped activated carbon coated carbon nanotube electrodes. *Electrochimica Acta*. 2017;**233**:142-150. DOI: 10.1016/j.electacta.2017.03.028

[56] Wang DW, Li F, Zhao J, Ren W, Chen ZG, Tan J, et al. Fabrication of graphene/polyaniline composite paper via in situ anodic electropolymerization for high-performance flexible electrode. *ACS Nano*. 2009;**3**:1745-1752. DOI: 10.1021/nn900297m

[57] Xu J, Wang K, Zu SZ, Han BH, Wie Z. Hierarchical nanocomposites of polyaniline nanowire arrays on graphene oxide sheets with synergistic effect for energy storage. *ACS Nano*. 2010;**4**:5019-5026. DOI: 10.1021/nn1006539

[58] Mini PA, Balakrishnan A, Nair SV, Subramanian KR. Highly

super capacitive electrodes made of graphene/poly(pyrrole). *Chemical Communications*. 2011;47:5753-5755. DOI: 10.1039/C1CC00119A

[59] Li J, Xie H, Li Y, Liu J, Li Z. Electrochemical properties of graphene nanosheets/polyaniline nanofibers composites as electrode for supercapacitors. *Journal of Power Sources*. 2011;196:10775-10781. DOI: 10.1016/j.jpowsour.2011.08.105

[60] Wang H, Hao Q, Yang X, Lu L, Wang X. A nanostructured graphene/polyaniline hybrid material for supercapacitors. *Nanoscale*. 2010;2:2164-2170. DOI: 10.1039/C0NR00224K

[61] Xue M, Li F, Zhu J, Song H, Zhang M, Cao T. Structure-based enhanced capacitance: In situ growth of highly ordered polyaniline nanorods on reduced graphene oxide patterns. *Advanced Functional Materials*. 2012;22:1284-1290. DOI: 10.1002/adfm.201101989

[62] Hu L, Tu J, Jiao S, Hou J, Zhu H, Fray DJ. In situ electrochemical polymerization of a nanorod-PANI-graphene composite in a reverse micelle electrolyte and its application in a supercapacitor. *Physical Chemistry Chemical Physics*. 2012;14:15652-15656. DOI: 10.1039/C2CP42192E

[63] Wang H, Hao Q, Yang X, Lu L, Wang X. Effect of graphene oxide on the properties of its composite with polyaniline. *ACS Applied Materials & Interfaces*. 2010;2:821-828. DOI: 10.1021/am900815k

[64] Feng XM, Li RM, Ma YW, Chen RF, Shi NE, Fan QL, et al. One-step electrochemical synthesis of graphene/polyaniline composite film and its applications. *Advanced Functional Materials*. 2011;21:2989-2996. DOI: 10.1002/adfm.201100038

[65] Mao L, Zhang K, Chan HSO, Wu JS. Surfactant-stabilized graphene/polyaniline nanofiber composites for high performance supercapacitor electrode. *Journal of Materials Chemistry*. 2012;22:80-85. DOI: 10.1039/C1JM12869H

[66] Wang H, Hao Q, Yang X, Lu L, Wang X. Graphene oxide doped polyaniline for supercapacitors. *Electrochemistry Communications*. 2009;11:1158-1161. DOI: 10.1016/j.elecom.2009.03.036

[67] Zhang LL, Zhao S, Tian XN, Zhao XS. Layered graphene oxide nanostructures with sandwiched conducting polymers as supercapacitor electrodes. *Langmuir*. 2010;26:17624-17628. DOI: 10.1021/la103413s

[68] Zhang K, Zhang LL, Zhao XS, Wu J. Graphene/polyaniline nanofiber composites as supercapacitor electrodes. *Chemistry of Materials*. 2010;22:1392-1401. DOI: 10.1021/cm902876u

[69] Liu Y, Zhang Y, Ma G, Wang Z, Liu K, Liu H. Ethylene glycol reduced graphene oxide/polypyrrole composite for supercapacitor. *Electrochimica Acta*. 2013;88:519-525. DOI: 10.1016/j.electacta.2012.10.082

[70] Alvi F, Ram MK, Basnayaka PA, Stefanakos E, Goswami Y, Kumar A. Graphene-polyethylenedioxythiophene conducting polymer nanocomposite based supercapacitor. *Electrochimica Acta*. 2011;56:9406-9412. DOI: 10.1016/j.electacta.2011.08.024

[71] Iijima S. Helical microtubules of graphitic carbon. *Nature*. 1991;354:56-58. DOI: 10.1038/354056a0

[72] Iijima S, Ichihashi T. Single-shell carbon nanotubes of 1-nm diameter. *Nature*. 1993;363:603-605. DOI: 10.1038/363603a0

- [73] Dai H. Carbon nanotubes: Opportunities and challenges. *Surface Science*. 2002;**500**:218-241. DOI: 10.1016/S0039-6028(01)01558-8
- [74] Wang G, Liang R, Liu L, Zhong B. Improving the specific capacitance of carbon nanotubes-based supercapacitors by combining introducing functional groups on carbon nanotubes with using redox-active electrolyte. *Electrochimica Acta*. 2014;**115**:183-188. DOI: 10.1016/j.electacta.2013.10.165
- [75] Niu C, Sichel EK, Hoch R, Moy D, Tennent H. High power electrochemical capacitors based on carbon nanotube electrodes. *Applied Physics Letters*. 1997;**70**:1480-1482. DOI: 10.1063/1.118568
- [76] An KH, Jeon KK, Kim WS, Park YS, Lim SC, Bae DJ, et al. Supercapacitors using single walled carbon nanotube electrodes. *Journal of the Korean Physical Society*. 2001;**39**:S511-S517. DOI: 10.1002/1521-4095(200104)13:7<497:AID-ADMA497>3.0.CO;2-H
- [77] Li X, Tang Y, Song J, Yang W, Wang M, Zhu C, et al. Self-supporting activated carbon/carbon nanotube/reduced graphene oxide flexible electrode for high performance supercapacitor. *Carbon*. 2018;**129**:236-244. DOI: 10.1016/j.carbon.2017.11.099
- [78] Zang X, Zhang R, Zhen Z, Lai W, Yang C, Kang F, et al. Flexible, temperature-tolerant supercapacitor based on hybrid carbon film electrodes. *Nano Energy*. 2017;**40**:224-232. DOI: 10.1016/j.nanoen.2017.08.026
- [79] Qiu L, Yang X, Gou X, Yang W, Ma Z-F, Wallace GG, et al. Dispersing carbon nanotubes with graphene oxide in water and synergistic effects between graphene derivatives. *Chemistry: A European Journal*. 2010;**16**:10653-10658. DOI: 10.1002/chem.201001771
- [80] Yu D, Dai L. Self-assembled graphene/carbon nanotube hybrid films for supercapacitors. *Journal of Physical Chemistry Letters*. 2010;**1**:467-470. DOI: 10.1021/jz9003137
- [81] Yu D, Goh K, Wang H, Li W, Jiang W, Zhang Q, et al. Scalable synthesis of hierarchically structured carbon nanotube-graphene fibers for capacitive energy storage. *Nature Nanotechnology*. 2014;**9**:555-562. DOI: 10.1038/nnano.2014.93

Fabric-Integrated, Ionic Liquid-Based Supercapacitor as a Tunable and Flexible Power Source

Sathya Narayan Kanakaraj, Paa Kwasi Adusei, Yu-Yun Hsieh, Yanbo Fang, Noe Alvarez and Vesselin Shanov

Abstract

With the introduction of flexible and wearable electronic technologies such as displays, antenna's, etc., there has been an increased need for integrable, easily scalable, and safe electric power sources. Advances in flexible lithium-ion batteries have been recently reported, however they may still suffer from potential thermal runaways. In this chapter we review the progress in the topic of wearable energy storage devices. These devices have taken the form of both sheets and fibers entirely made of active material. We also discuss the advantages and drawbacks of each forms. Finally, we present our own work revealing a simplistic way to integrate working carbon electrode materials into suitable textile and to functionalize the obtained flexible structure with ionic liquid thus creating fabric supercapacitors. These devices can then be connected easily in series (9 V) or in parallel (high current), depending on the current or voltage requirements. The area of the electrodes can also be tuned to sustain higher capacitances. We report an energy density of 48 Wh/kg for a functional device at 3 V working window, which reveals no losses in energy density after 10,000 bending cycles.

Keywords: supercapacitor, EMIMBF₄, wearable electronics, gel electrolyte, energy storage

1. Introduction

Wearable technology has seen a great spike in development over the past decade [1–3] in the form of fabric integrated sensors (heart rate, chemical gas, etc.), information transfer lines and even energy harvesting (piezoelectric). This comes with the need to develop flexible and durable devices that can effectively power them [4, 5]. Energy storage devices typically consist of current collectors (for transfer of current to and from the electrodes), high surface area electrodes (for actively storing energy in the form of ions), insulating separators (for preventing shorting between electrodes) and an electrolyte. High surface area carbon such as graphite and activated carbon has become the standard electrode for many mainstream energy storage applications. However, metals (copper, steel and aluminum) are still heavily relied upon for taking on the role of current collector. This is a major issue for wearable devices as metals very easily succumb to fatigue through bend cycles and are also prone to oxidation. In addition, metal electrodes substantially add to

the total weight of the device. Care must be taken to prevent the metal from having direct contact with electrolyte as this would cause unwanted oxidation reactions and subsequent deterioration of the device. All these factors combined make it necessary to find an alternative to the metal current collectors for developing wearable energy storage devices.

Carbon based nanomaterials have emerged as promising candidates for the role of a flexible and durable current collector [6]. They boast very high theoretical specific surface area [7–11] reaching up to $3100 \text{ m}^2 \text{ g}^{-1}$ for graphene [11]. Some of the materials also have very high strength and conductivities owing to their sp^2 bonds [12]. All these properties are valuable when it comes to energy storage. Further, most of carbon-based nanomaterials can be synthesized employing non-expensive and scalable processes, making them an ideal alternative to metals. These materials can even be tuned and equipped to function differently depending on the application and need (energy vs. power) represented in the Ragone plot in **Figure 1a** [13].

Electric double layer capacitors (EDLC) are employed where the power is of utmost importance, i.e. the ability to charge and discharge quickly. This is achieved through a non-reactive mechanism wherein the ions of the electrolyte are simply housed on and in the electrodes [14–17]. This process is depicted in **Figure 1b**, the pore size and volume being the most important parameters affecting the energy stored. The size of the pores must be very similar to that of the ion size, meaning different electrolytes require different pore size distributions. Since the mechanism of ion housing is a simple potential assisted diffusion, it allows for very high power [18–20] and high stable cycling of over 100,000 cycles. However, the stored energy is limited as it is heavily restricted by the achievable pore density. This can be partially overcome by using higher voltage stable electrolytes. Ionic liquids are one such class of electrolytes that have a stable window of about 4.5 V.

Pseudocapacitors are a class of energy storage devices that fit the need for high power without compromising on energy. The electrode materials used here have the disadvantage of being low in conductivity, leading to heavy losses through resistance. This is overcome by depositing them on conducting templates. They rely on fast redox reaction mechanism, usually involving surface absorption of electrolytic cations and proton absorption that leads to change in oxidative state [13, 21]. This involves protonation/electronation of the electrode resulting in a change in oxidation state. The briefly described mechanism is depicted in **Figure 1c**. Since redox reactions require actual chemical change, the electrode unavoidably degrades over time due to inefficiencies. The degradation is also attributed to volume expansions that cannot be sustained by the poor mechanical properties of the material. This results in lowering of the cyclability considerably [22]. Another consequence of the higher energy is lowering of the power. To fully utilize the electrode surface area, engineered nanostructures of pseudocapacitive materials with high surface area to volume fractions needs to be realized.

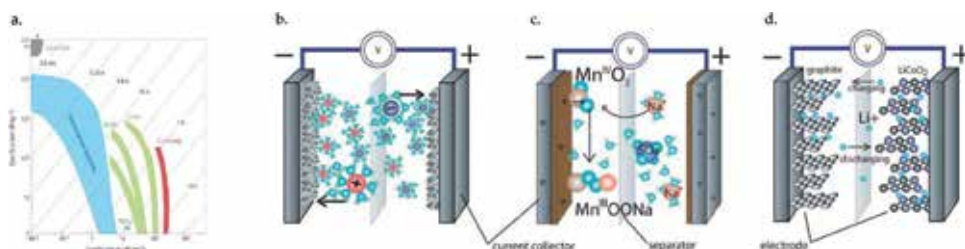


Figure 1. (a) Ragone plot of specific power vs. specific energy for different energy storing devices—reproduced from [13] with permission from Springer Nature; (b) EDLC; (c) pseudocapacitors; and (d) battery—reproduced from [17] with permission from The Royal Society of Chemistry.

Batteries are electrochemical devices that fulfill the needs of high energy storage densities at the expense of power reduction. Their charge-storing mechanism involves actual chemical reactions taking place at the electrodes [23]. This includes ions reacting and transferring from one electrode via the electrolyte and intercalating into the other electrode, as displayed in **Figure 1d**. Depending on the chemical makeup of the electrode and the electrolyte used, the voltage window and charge stored can be tuned [24]. Due to the formation of actual compounds, the reversibility of this mode of charge storage is limited. It also gives the lowest power density of all the energy storage mechanisms described here.

All the mechanisms discussed above can be taken advantage of by using carbon-based nanomaterials to make them adapt to a wearable form. Energy storage in the form of wearable devices has seen considerable development in recent years and has achieved 3 major milestones (methods).

- (i) Introduction of sp^2 bonded carbon nanomaterials.
- (ii) Employment of dip coating and its optimization.
- (iii) Synthesis of fiber-based devices.

The intention of this chapter is to give a concise view of the progress that the wearable energy storage research has achieved, to discuss the advantages and drawbacks of each milestone and finally to introduce our approach for fabricating integrated energy storage devices.

2. Choosing electrode material

Conventional fabric materials do not inherently have the ability to store energy. Thus, the materials that functionalize and allow textile fabric to become energy storage devices are of high importance. It is necessary to explore and develop these materials, mainly carbonaceous, to best suit the application. Owing to this, there has been extensive research conducted on the synthesis/fabrication and characterization of carbon nanomaterials.

The most simplistic form of carbon nanomaterials is the exfoliation of coal to create *carbon black and activated carbon* [25, 26] (**Figure 2a**). The latter has a very high porosity in both the micro (<2 nm) and mesoporous (2–50 nm) range. This makes them ideal for their application as EDLC electrodes. Their ease of synthesis lowers the price to fabricate them. However, they suffer from some drawbacks. They are produced as flakes and as such are not freestanding. This requires the use of a polymer binder which further reduces the conductivity of the material. It is also overwhelmed by significant amounts of amorphous carbon that does not contribute effectively to the electrical conductivity of the material. Furthermore, this carbon-polymer mixture must be cast onto metal current collectors [27–30] to form electrodes, since in their free standing form they are not structurally stable. This makes them difficult to be used as wearable devices.

Carbon nanotubes (CNTs) (**Figure 2b**), have emerged as a very promising electrode material candidate because of their high theoretical property values. The individual multiwalled CNT (MWCNT) has been measured to have an average tensile strength of 60 GPa [31] and a Young's modulus of over 1 TPa [32, 33], with a low electrical resistivity of 3×10^{-5} ohm cm [34–36], and a thermal conductivity of 3500 Wm K^{-1} [37, 38]. All these properties arise from the sp^2 bonds connecting the carbon atoms in the form of a tube. However, as dispersed tubes, they would pose the same problems that traditional powdered carbon materials reveal. Hence, there has been extensive research on exploring ways to scale them up into macro-assemblies. This is directly related to their synthesis process. There are presently three

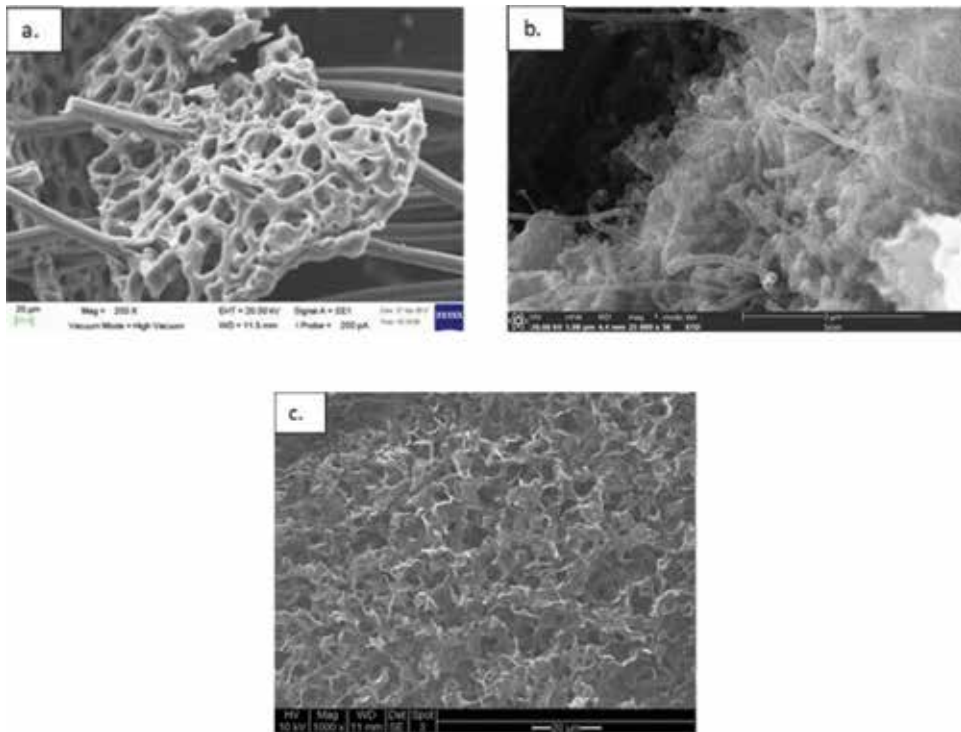


Figure 2. SEM images of: (a) activated carbon, reprinted with permission from [45]; (b) CNTs and (c) graphene.

major established ones, namely direct assembly from gaseous phase, wet spinning and dry spinning from vertically aligned arrays. Macro-assemblages gathered from wet phase are drawn from lyotropic liquid-crystalline phase CNT matrix—which requires the use of corrosive acids to make the CNT solution [39–41]. This results in a final product that has already undergone post processing and contains catalyst impurities, which makes them less effective to further post processing treatments. The macro-assemblages drawn from vertically aligned (VA) CNT arrays, as made in a chemical vapor deposition (CVD) reactor, are in a much more pristine state. This makes them more ideal for further processing. The individual tubes are held together via van der Waals forces and hence require no binding material. This gives CNT assemblages the ability to act as free-standing structures and makes them a good candidate for wearable electrode material.

Graphene, **Figure 2c**, and reduced graphene oxide (rGO) are both highly researched allotropes of carbon for energy storage electrode material. However, as rGO is produced in the form of flakes, it requires a binder and thus cannot be very easily translated into a wearable device. Graphene provides the opportunity to be synthesized in a paper form. This, added with its high surface area and conductivity [11], makes it ideal candidate for a structurally stable current collector. CVD is the more versatile synthesis method as this allows for inclusion of various precursors for functionalization of the graphene. The catalyst can also be modified to tune the porosity of the graphene material. All of these tunable properties allow graphene paper to be used as a conductive housing for different active materials and electrolyte [42–44].

It is seen that sp^2 bonded carbon nanomaterials such as CNTs and graphene have the best suitable properties—high surface area, conductivity and strength—to elevate energy storage in the wearable format. Thus, they lend themselves as a pivotal milestone in the development of fabric-based energy storage devices.

Prior to establishing the norm of using carbon nanomaterials as conductive pathways/current collectors, *active materials* themselves have been used as electrodes. We define active material as those oxides, compounds or polymer chains that can store charge in the form of chemical reactions or volume expansions. However, due to their insulating nature and poor structural strength, their pristine form is mostly avoided for composite materials.

3. Dip coating as a tool for fabricating of fabric-based energy storage devices

Textile fabric materials made by weaving synthetic or natural fibers are highly flexible and possess high surface area. This makes them ideal templates for housing active materials that can store energy. Dip coating takes advantage of this characteristic by applying CNTs or graphene on the surface of the textile fibers via dipping in an aqueous solution that contains a dispersion of the active material (**Figure 3a and b**). Drying the fabric results in a coated material that is ready to be used as a flexible electrode. Cotton, owing to its strength and hydrophilicity, is primarily used for this process as it involves an aqueous solution. Hu et al., utilized this process to make CNT coated cotton fabric electrodes [46] (**Figure 3a and b**). They achieved high active loading of 8 mg/cm^2 resulting in a capacitance of 120 F/g . The impregnation and consequent coating is highly dependent on the permeability/retention ability of the textile used in this process. This renders dip coating a non-versatile and non-reproducible process. The density of packing is also affected making the material not highly conductive. To overcome these issues, screen printing was introduced. By the simple employment of a screen resist on top of the fabric before the application of a thick slurry of the active material, a binder-active material solution can be very evenly coated to the surface of the fabric textiles [46]. This allows for good control over exactly how much of active material is loaded depending on the concentration and volume of the slurry used. The method allows for multiple repetitions as an easy way to increase the mass loading. This way, a reproducible capacitance of 90 F/g was achieved [46].

However, there is an upper limit to the amount of active material that can be added because of the shrinking porosity of the fabric skeleton with impregnation. As a consequence, there is a maximum for the capacitance values that can be achieved. One factor that can be easily changed to better the properties is the active material. Pseudocapacitive materials can be used as active material known for their higher theoretical specific capacitance (F/g). Thus, with the same mass loading, much higher capacitances can be achieved. Yu et al. explored electrodeposition to coat manganese oxide onto graphene coated textile fibers [47], as shown in **Figure 4a**, which successfully increased the capacitance to 350 F/g . The same approach can be adopted to deposit other pseudocapacitive material, such as ruthenium oxide or

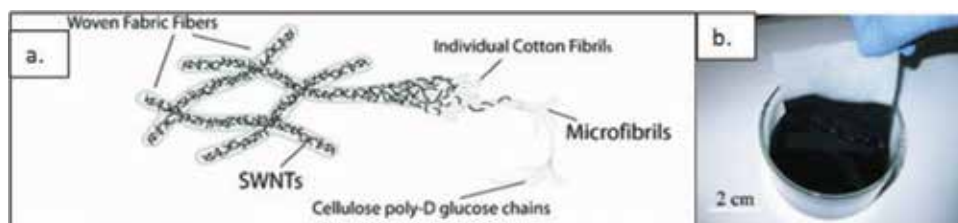


Figure 3. (a) Schematic of screen printed CNT-cotton fibers and (b) picture of the dip coating process with cotton fabric. Reprinted with permission from [46]. Copyright 2010 American Chemical Society.

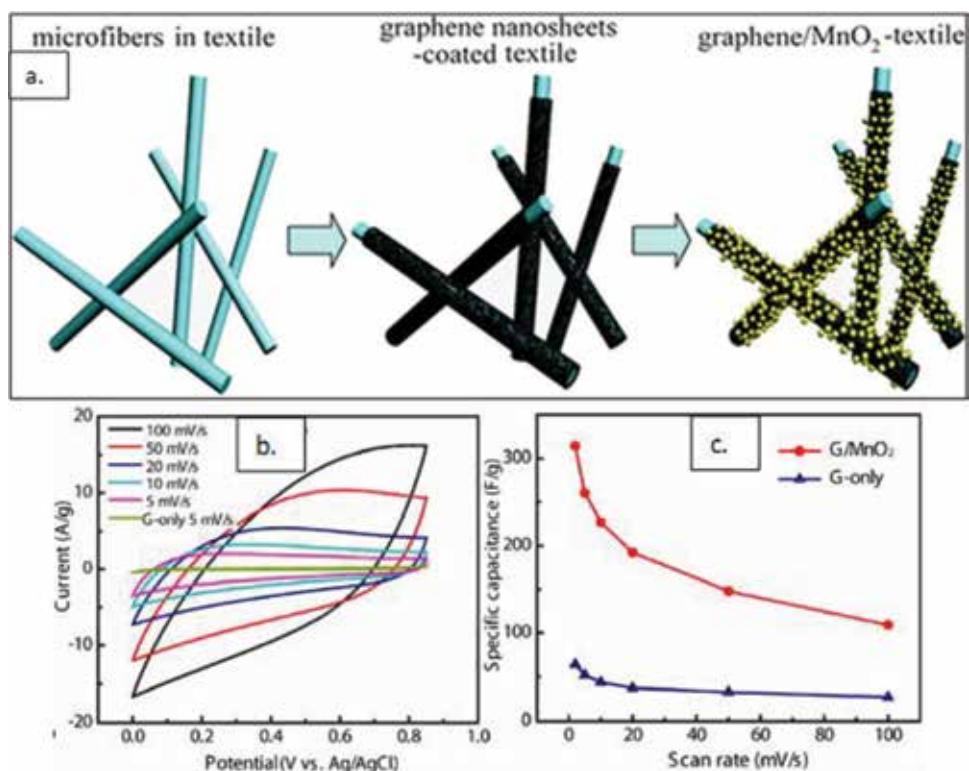


Figure 4.

(a) Schematic of electrodeposition of manganese oxide on graphene coated textile fibers; (b) half-cell cyclic voltammetry of manganese oxide-graphene-fabric electrode; (c) capacitance vs. scan rate curves. Reprinted with permission from [47]. Copyright 2011 American Chemical Society.

conductive polymers. An asymmetrical device with high energy densities can be fabricated by carefully choosing the electrodes based on their working reduction potential ranges. Changing the crystallinity and nanostructure of the deposited material by controlling the deposition parameters and composition can also yield better properties. The alpha phase of the manganese oxide is more conductive and electrochemically stable than its beta and amorphous forms. Thus, a very fine nanorod-structured deposition of alpha phase manganese oxide can greatly increase the energy density. Another option for the device property improvement is exploring more electrochemically active materials such as lithium metal oxides, sulfur, etc. Thus, with the use of a polymer electrolyte matrix separator, a flexible battery device can be fabricated.

As demonstrated in the cyclic voltammetry curves in **Figure 4b** and **c**, there is still a very non-capacitive (rectangular) nature to the fabric devices. This is in part a contribution from the low loading of conductive material—CNT or graphene. The other active materials (pseudocapacitive or battery) are not very conductive in nature and highly rely upon the carbon-base material for their electron transfer requirements. Thus, there are heavy losses in terms of power density in such materials. This can be avoided with the use of metals as current collectors, however making the device non-flexible.

The most promising advantage of the discussed dip coating is the low production cost and time consumption. However, further improvement of the carbon coating material needs to be realized to progress in this fabrication method. An alternative is a fully core to shell design made completely of conductive carbon material and coated active material. This would result in a 100% mass loading of active material and would give more energy per unit gram of fabric.

4. Fiber-based electrodes

Electrodes in the form of yarns that can be readily stitched as a textile fabric has the potential to overcome many of the disadvantages discussed in the previous section. The research in fiber/yarn-based electrodes began with dip coating techniques and as discussed in the sections before, some challenges have emerged. The conductivity and active loading of the material was low, and the related research eventually moved towards more promising approaches. One of them is the possibility to realize a fully active material loaded fiber form.

A conductive carbon-based core that provides the strength, conductivity and flexibility with an outer shell of active material that secures high energy density has been explored. CNTs dispersed in acid and extruded in the form of a fibers which have been easily fabricated. These porous fibers act as a current collector and housing for the active material. Vertically aligned CNT arrays can be used to spin long and porous fibers. These are produced in a more pristine format and hence can be easily processed and react less with electrolytes. These full core-shell carbon structures have very high surface area $\sim 1400 \text{ m}^2/\text{g}$, which gives the opportunity to take advantage of the ELDC characteristic of these fibers [48]. Novel fiber structures utilizing higher surface area graphene have also been fabricate. RGO based fibers that are highly porous and boasting surface area up to $2400 \text{ m}^2/\text{g}$ have been reported, which results in a very high energy density of 400 F/g [49] (**Figure 5i a–c**). Hybrids involving both CNTs and graphene have been synthesized, utilizing the high surface area of both material to create a sponge like fiber material [48] (**Figure 5ii a–c**). Flexible fibers were successfully woven into a fabric and its performance remained consistent through exposure to bending stress. The major drawback of these high energy storage materials is their strength. Although their Young's modulus is appreciable, which allows them to be flexible, their tensile strain to failure is quite low. This makes them prone to breakage and unfit to survive as a self-supporting fabric patch. Addition of any active material to the fiber would make them too brittle to handle.

Carbon fibers, which are a very sturdy and high strength materials, have been used as a substrate to house pseudocapacitive manganese oxide [50] (**Figure 5v a–c**). The resulting fiber proved to be quite strong and showed appreciable energy storage values. However, the electrical conductivity of the material is still a concern. Conventional carbon nanotube fibers have also been used as conductive substrate for housing manganese oxide [51] (**Figure 5iv a–c**). The resulting composite was wound like a spring and encapsulated in a gel polymer, showing no losses in energy storage properties for tensile strains of up to 100%.

A polymer core with carbon nanomaterials grown/deposited across the surface derives most of its strength from the elastic polymer and can sustain higher tensile strains. Active material can then be successfully decorated on the surface [52] (**Figure 5v a–c**). This however suffers from the loss of conductivity and requires an additional current collector in the form of a multiplied metal yarn structure.

Fibers made completely out of electrochemically active material such as poly(3,4-ethylenedioxythiophene) (PEDOT) have also been developed [53]. The bisrolled PEDOT with the CNT matrix makes the composite quite easy to scale up. Further, due to the high electrical contact between the current collector and active material, the device shows good performance at 1 mV/s scan rate. The greatly twisted fiber boasts very high active material loading and high volumetric capacitance.

There are some challenges to the development of these forms of devices. They have the potential to be composed completely of active material leading to unsurpassed energy storage capabilities, however, the loss in strength of the material needs to be countered. A fiber that possess both great tensile strain, strength and high loading of active material could pave way to the next generation of wearable devices. We believe that the key lies in highly densified CNT fibers with modified surfaces.

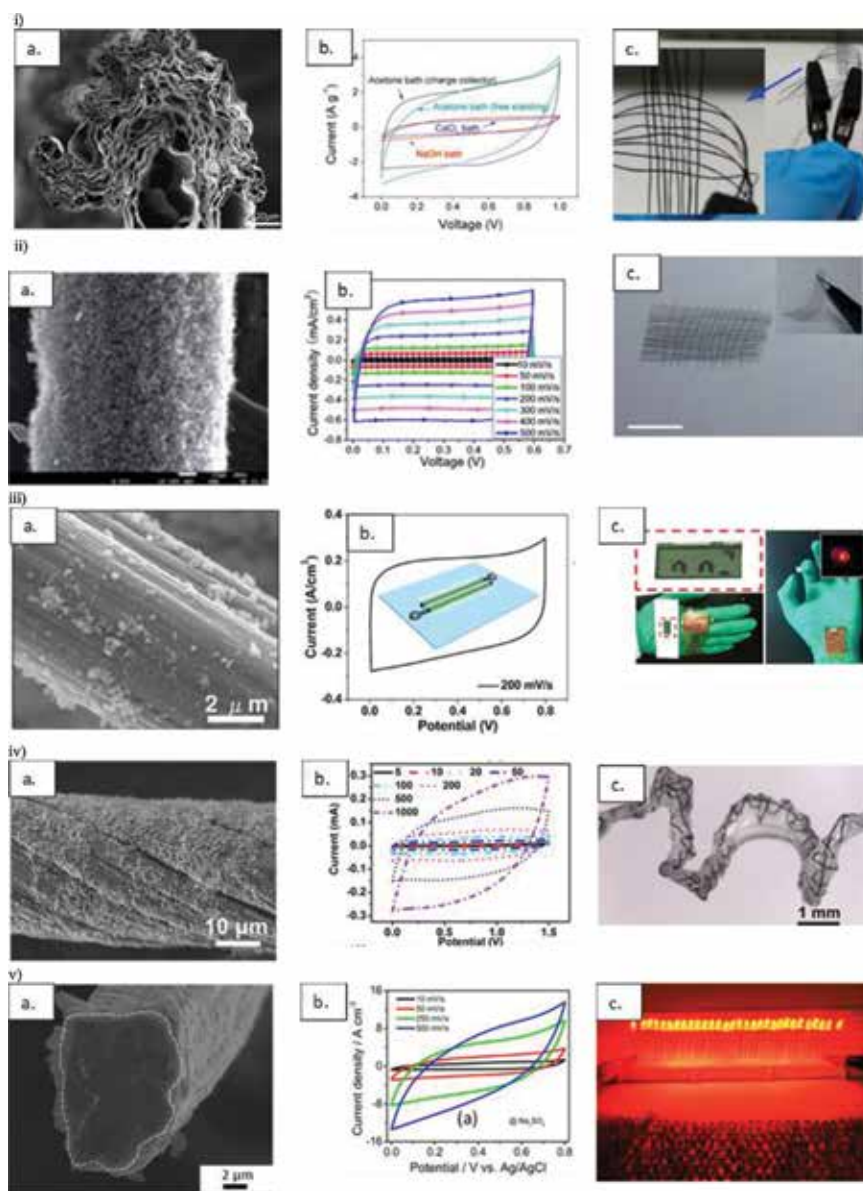


Figure 5. (a) SEM image of electrode base material; (b) cyclic voltammetry graph of the working device; (c) picture of full device. (i) RGO fiber reprinted with permission from [49]. Copyright 2014 American Chemical Society. (ii) CNT-graphene fiber reproduced from [48] with permission from Royal Society of Chemistry. (iii) Carbon fiber coated with manganese oxide reprinted with permission from [50]. Copyright 2012 American Chemical Society. (iv) CNT fiber coated with manganese oxide reprinted with permission from [51]. Copyright 2015 American Chemical Society. (v) GO-active material coated stainless steel fiber reprinted with permission from [52]. Copyright 2015 American Chemical Society.

5. Ionic liquid-based fabric capacitor

Below are presented experimental results on ionic liquid-based fabric capacitors obtained by our team. A factor that is often ignored when it comes to wearable devices is the evaluation of their properties as a function of the weight of the materials. In these cases, most used is the area of the material or only the weight of the active material is taken into consideration. This becomes a limitation when scaling to industry production as bulky materials will not be suitable for powering

fabric-based devices. Most of literature data still relies on textile fibers to provide the structural and flexible skeleton for their electrodes. This requires the usage of two layers of fabrics (electrodes) that adds unnecessary weight to the full device which is mostly never reported. An aspect to consider is the synthesis approach. The more structured the active synthesized material, the higher the surface area and therefore gives a higher specific capacitance. A drawback of this is the cost—both monetary and time consuming—that scales exponentially with the structure complexity. The other major consideration that is overlooked is the practical feasibility of the devices fulfilling certain applications. Most wearable energy storage devices have adopted gel-based polymer electrolyte systems to create a flexible separator. However, they still rely upon aqueous electrolytes such as phosphoric acid, potassium hydroxide, etc. This caps the voltage window for conventional devices with high cyclability to a low value of 0.8 V. However, even LEDs require around 1.3 V to operate. The non-conventional asymmetrical devices can push the envelope to around 1.6 V, but beyond that they suffer from heavy capacitance losses. In this section, we hope to provide a solution based on our work to these practical challenges.

Aqueous electrolytes, although inexpensive and stable, are limited by their low reduction potentials with most conventional carbon materials. Anything beyond voltage window of 1 V results in irrecoverable losses in both the electrode material and the electrolyte. This limitation comes mainly from the presence of water. Thus, a change from aqueous to organic solutions results in a drastic change in the voltage window stability range. Commonly explored solutions are ethanol with suitable salts such as lithium perchlorate dissolved in them. Devices made with this electrolyte can expand the operation window from 1 V to around 2.2 V. This window decreases with introduction of pseudocapacitive materials to around 1.2 V, which is much higher than the 0.8 V offered by aqueous electrolytes. A device with asymmetrical electrodes can increase this window up to 2.2 V. To achieve a higher voltage window more expensive and less explored materials need to be considered. The latter are known as ionic liquids (ILs). These are a highly reactive group of electrolytes that are a combination of an organic cation with a very electronegative anion. Some of them—1-ethyl-3-methylimidazolium tetrafluoroborate (EMIMBF₄)—have a very large and stable working voltage window, going as high as 4.5 V. They find usage as catalysts for higher voltage reduction reactions, however there is an emerging interest in their utilization in energy storage applications. ILs are most commonly combined with polyvinylidene fluoride-hexafluoropropylene (PVDF-HFP) to create a gel polymer electrolyte separator matrix.

We introduce here a novel way to incorporate the IL EMIMBF₄ into any fabric material (from stretchable polyester sports-wear to sturdy military fabric) that utilizes only the essential amount of fabric material. For our tests we procured normal Bucky paper (BP) from General Nano, LLC which is a matrix of single walled carbon nanotubes under no alignment. Our procedure includes using the fabric as a separator to house the gel electrolyte and eventually be sandwiched between symmetrical BP electrodes (**Figure 6a**). Initially, polyvinyl alcohol (PVA)-sulfuric acid gel matrix was used. The gel electrolyte (1 g of PVA in 10 ml 0.1 M sulfuric acid) was dropped into the fabric. The soaked fabric was then allowed to dry till it reached a gel-like consistency. The electrodes were then applied on top of the electrolyte and allowed to further dry until they became integrated into the fabric electrolyte structure. This device was tested electrochemically using a Potentiostat Interface 1000, Gamry Instruments and showed results comparable to conventional devices made without the fabric separator. A similar gel polymer concentration was utilized for the IL (3 ml EMIMBF₄ in 10 ml acetone with 1 g PVDF). The same methodology was adopted to create the gel fabric. However, the electrochemical results with the device were not comparable with average values of conventional devices. This was

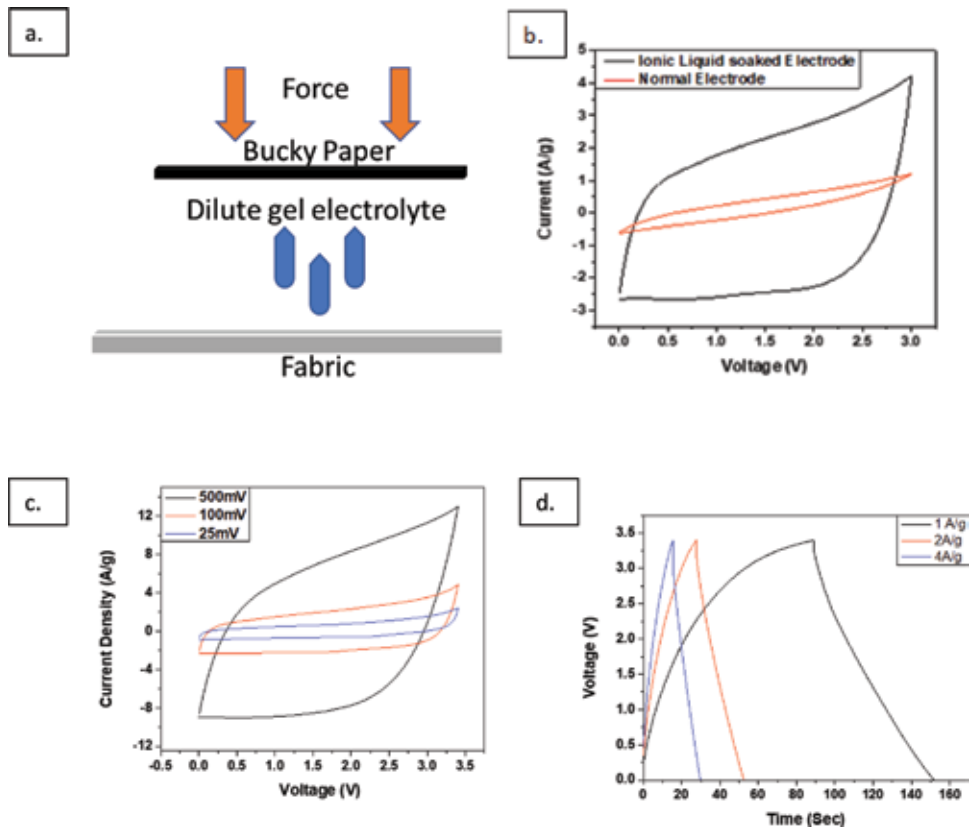


Figure 6. (a) Schematic of creating gel fabric structure with Bucky paper electrode pressed on top; (b) cyclic voltammetry curves at 200 mV/s for normal BP electrode and BP electrode pre-soaked in IL solution; (c) different scan rate cyclic voltammetry curves of IL-soaked device; and (d) charge and discharge curves of the fabricated device obtained at different current densities.

not an indication of the limit of the electrode as the sulfuric acid device gave appreciable values. We added a further step to the device fabrication, which included first soaking the electrode in a solution of the IL plus acetone, and then incorporating it into the fabric structure. This resulted in an increase of the device energy density (Table 1 and Figure 6b–d). Since acetone is fast evaporating solvent, it did not allow for the electrode to be fully penetrated with the electrolyte before drying. The described soaking procedure ensured complete utilization of the electrode surface area and thus increased the stored energy.

The device can be steadily cycled between 0 and 3 V window range without fade in capacitance values. This is not the only major advantage of such a device. Since

Gel electrolyte	Specific capacitance (F/g)	Energy density (Wh/kg)
PVA-sulfuric acid (1 V)	11.54	3.2
PVDF-ionic liquid (3 V)	61.66	19.53
Ionic liquid soak	137.6	48.62

Table 1. Specific capacitance and energy density values of the fabric device achieved with different polymer electrolytes and preparation techniques.

the fabric is being used as a separator and not as the electrode itself, it essentially reduces the weight of the device in half, as compared to other wearable energy storage devices that rely on a fabric skeleton backing for each electrode. The fabric can then be further sewn in as a patch thus making the only additional weight contribution to the device that of the gel electrolyte. Another key advantage of the described system is the ability to be easily modified for various applications. Depending on the energy need, the area of the electrode used can be increased or decreased to give highly tunable capacitance values (**Figure 7a and b**). Since the application and fabrication of the gel fabric is easily controlled, the device can also be made into sections. Various electrodes can be applied next to each other as isolated devices on the same fabric. One patch of fabric could contain many isolated devices. This gives high tunability to the device. Three isolated devices were made in one patch and when connected in series it achieved a working voltage of 9 V. In a parallel wiring

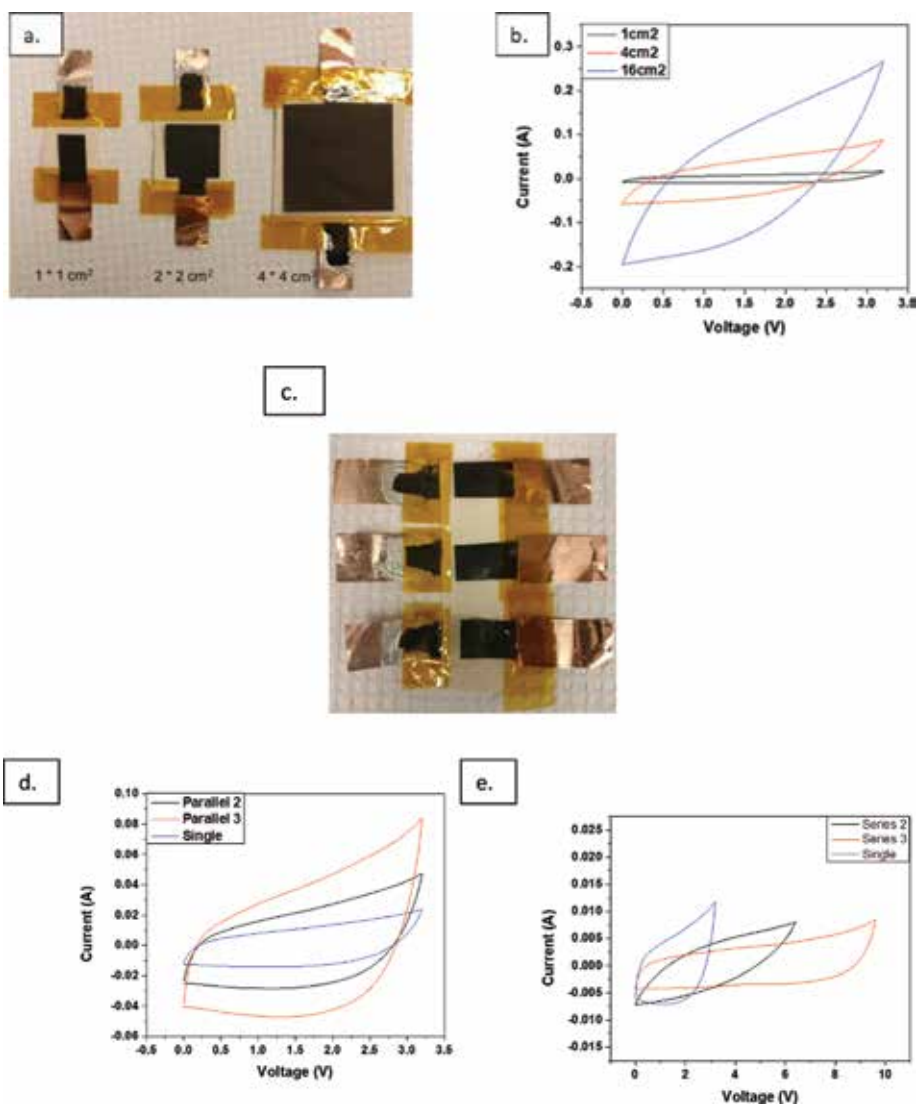


Figure 7. (a) Pictures of different size with increasing areas of electrode materials used for the fabric device; (b) corresponding cyclic voltammetry profiles at 200 mV/s scan rate; (c) picture of isolated devices in a single patch of fabric; (d) corresponding cyclic voltammetry profiles at 200 mV/s scan rate in parallel connections and (e) corresponding cyclic voltammetry profiles at 200 mV/s scan rate in series connections.

the device achieved 3 times the current output and energy density of an individual one (**Figure 7c–e**). The fabricated device is highly versatile in terms of how it can fit to different applications. Electrical contacts can be made by simply applying copper tapes with silver paint to the ends of the electrodes. These connections need not be pre-made, giving a further degree of freedom.

Textile fabrics are exposed to stress in the form of flexing, bending or wrinkling. This is unavoidable in clothing when the wearer executes any form of motion. Such an environment must be taken into consideration when making fabric integrated devices. Here we tested our fabric device by exposing them to 10,000 cycles, where in each cycle it was bent to an angle of 120° and brought back to normal shape (**Figure 8a**). This is a higher degree of bending than fabrics

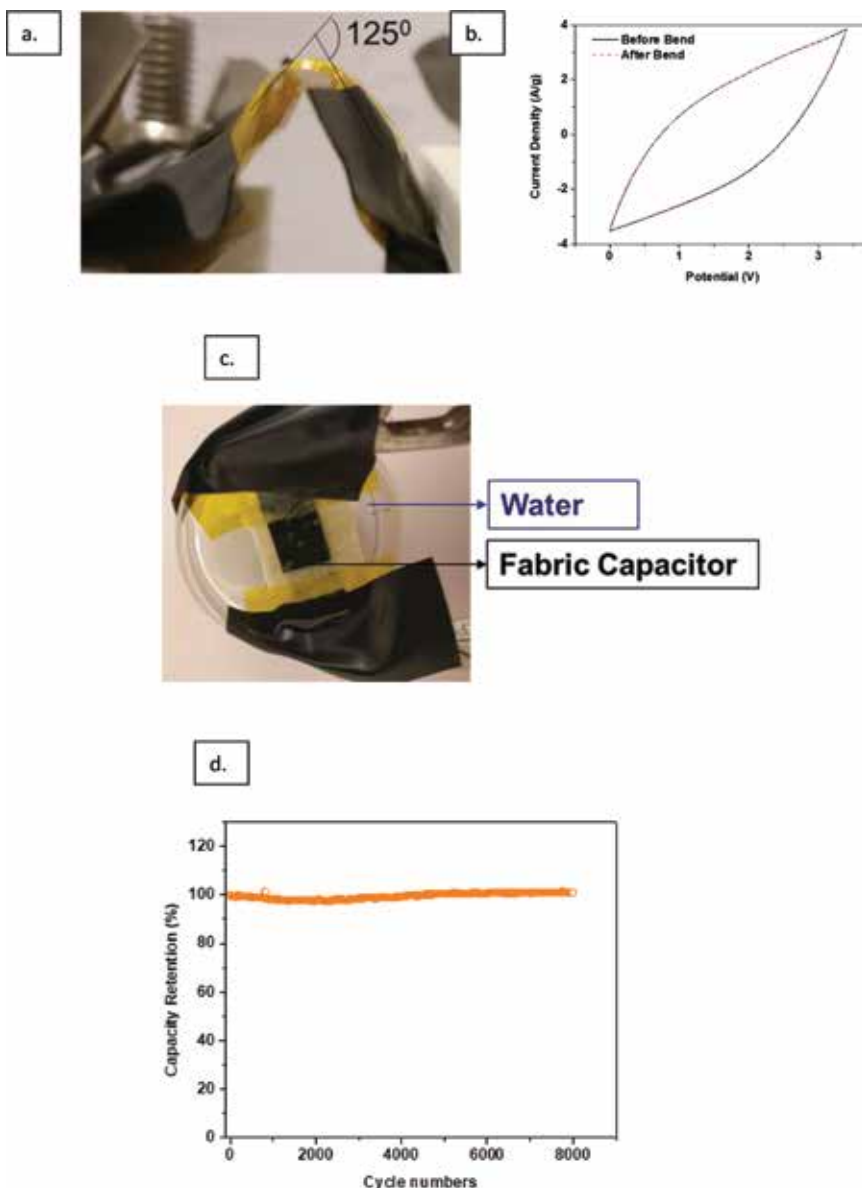


Figure 8. (a) Picture of the degree of bending during each cycle of the stress test; (b) cyclic voltammetry curve of the device before and after bending; (c) picture of the water bath immersion tests; and (d) cycling curve of the device at 2 A/g current density.

would have to usually sustain on a daily basis. The device showed no depreciation in terms of capacitance after the cycling (**Figure 8b**). Another consideration to be taken into account is the exposure to moisture in the form of sweat from the wearer. Our device was soaked in a bath of water and cycled. In this test no observable depreciation in energy density was noticed (**Figure 8c**). Finally, the device was cycled 8000 times at a current density of 2 A/g that resulted in a final capacitance of 102% (**Figure 8d**). This increased capacitance is due to the forcible opening of the pores of the BP electrode with constant cycling. The high retention rate is very promising and ensures that the electrolyte is not being degraded at such high voltage ranges.

There still exists room for improvement for the described architecture of the fabric devices. Altering the electrodes by creating more energy dense materials is a quick way to further improve the properties of the device. Using pseudocapacitive materials like transition metal oxides or conductive polymers in an asymmetrical electrode arrangement has the potential to further enhance the properties. This will be explored in our following works.

6. Conclusion

The wearable energy storage devices have seen much development over the last decade. This evolution included starting from cotton coated electrodes that were not highly reproducible and moving to more reliable techniques such as screen printing using a polymer resist. Further, full active material loaded yarns have been realized. There are however drawbacks with each of the approaches which include either a limit to the active material content and subsequently the energy density, or a lack of strong materials that can sustain the wear and tear of fabrics that will potentially go into articles of clothing. The most promise is shown when using yarn-based devices that, if coupled with high strength, may provide the best properties.

In our work we designed an approach to making a tunable device that can accommodate a various range of practical applications including those requiring voltages as high as 9 V or high current ratings. The gel fabric separator fabricated and reported here utilizes just the essential amounts of fabric, which can be easily patched onto articles of clothing thus adding no extra weight. The final device we created exhibits an energy density of 48 Wh/kg at 1 A/g current density and can sustain high cycling without any noticeable losses in capacitance. The described fabrication approach is versatile and can be adopted for making various electrodes that can further improve the properties of the fabric energy storage devices.

Acknowledgements

This work was partly funded by the following grants: DURIP-ONR N00014-15-1-2473, AFOSR LRIR 16COR322, ARMY W911NF-16-2-0026, NASA NNX13AF46A, and NNC16CA17C. The financial support from the above-mentioned Government institutions is highly appreciated.

Conflict of interest

The authors declare that there was no conflict of interest during this work.

Author details

Sathya Narayan Kanakaraj¹, Paa Kwasi Adusei¹, Yu-Yun Hsieh¹, Yanbo Fang¹,
Noe Alvarez³ and Vesselin Shanov^{1,2*}


1 Department of Mechanical and Materials Engineering, University of Cincinnati,
Cincinnati, OH, USA

2 Department of Chemical and Environmental Engineering, University of
Cincinnati, OH, USA

3 Department of Chemistry, University of Cincinnati, OH, USA

*Address all correspondence to: vesselin.shanov@uc.edu

IntechOpen

© 2018 The Author(s). Licensee IntechOpen. This chapter is distributed under the terms of the Creative Commons Attribution License (<http://creativecommons.org/licenses/by/3.0>), which permits unrestricted use, distribution, and reproduction in any medium, provided the original work is properly cited. 

References

- [1] Esposito M, Minutolo A, Megna R, Forastiere M, Magliulo M, De Pietro G. A smart mobile, self-configuring, context-aware architecture for personal health monitoring. *Engineering Applications of Artificial Intelligence*. 2018;**67**:136-156. DOI: 10.1016/J.ENGAPPAI.2017.09.019
- [2] Jung S, Lauterbach C, Strasser M, Weber W. Enabling technologies for disappearing electronics in smart textiles. In: 2003 IEEE International Solid-State Circuits Conference, 2003. Digest of Technical Papers. ISSCC. Vol. 1. 2003. pp. 386-387. DOI: 10.1109/ISSCC.2003.1234347
- [3] Post ER, Orth M. Smart fabric, or "wearable clothing". In: Digest of Papers. First International Symposium on Wearable Computers. 1997. pp. 167-168. DOI: 10.1109/ISWC.1997.629937
- [4] Li Y, Torah R, Beeby S, Tudor J. An all-inkjet printed flexible capacitor on a textile using a new poly(4-vinylphenol) dielectric ink for wearable applications. In: 2012 IEEE Sensors. 2012. pp. 1-4. DOI: 10.1109/ICSENS.2012.6411117
- [5] Kim BC, Too CO, Kwon JS, Ko JM, Wallace GG. A flexible capacitor based on conducting polymer electrodes. *Synthetic Metals*. 2011;**161**:1130-1132. DOI: 10.1016/j.synthmet.2011.01.015
- [6] Chen T, Dai L. Flexible supercapacitors based on carbon nanomaterials. *Journal of Materials Chemistry A*. 2014;**2**:10756-10775
- [7] Chmiola J, Yushin G, Gogotsi Y, Portet C, Simon P, Taberna PL. Anomalous increase in carbon capacitance at pore sizes less than 1 nanometer. *Science*. 2006;**313**:1760-1763. <http://science.sciencemag.org/content/313/5794/1760.abstract>
- [8] Futaba DN, Hata K, Yamada T, Hiraoka T, Hayamizu Y, Kakudate Y, et al. Shape-engineerable and highly densely packed single-walled carbon nanotubes and their application as super-capacitor electrodes. *Nature Materials*. 2006;**5**:987. <http://dx.doi.org/10.1038/nmat1782>
- [9] Huang J, Sumpter BG, Meunier V. Theoretical model for nanoporous carbon supercapacitors. *Angewandte Chemie International Edition*. 2007;**47**:520-524. DOI: 10.1002/anie.200703864
- [10] Tao XY, Zhang XB, Zhang L, Cheng JP, Liu F, Luo JH, et al. Synthesis of multi-branched porous carbon nanofibers and their application in electrochemical double-layer capacitors. *Carbon*. 2006;**44**:1425-1428. DOI: 10.1016/j.carbon.2005.11.024
- [11] Zhu Y, Murali S, Stoller MD, Ganesh KJ, Cai W, Ferreira PJ, et al. Carbon-based supercapacitors produced by activation of graphene. *Science*. 2011;**332**:1537-1541. <http://science.sciencemag.org/content/332/6037/1537.abstract>
- [12] Castro Neto AH, Guinea F, Peres NMR, Novoselov KS, Geim AK. The electronic properties of graphene. *Reviews of Modern Physics*. 2009;**81**:109-162. DOI: 10.1103/RevModPhys.81.109
- [13] Simon P, Gogotsi Y. Materials for electrochemical capacitors. *Nature Materials*. 2008;**7**:845. DOI: 10.1038/nmat2297
- [14] Winter M, Brodd RJ. What are batteries, fuel cells, and supercapacitors? *Chemical Reviews*. 2004;**104**:4245-4270. DOI: 10.1021/cr020730k
- [15] Jintao Z, Zhao XS. On the configuration of supercapacitors for maximizing electrochemical

- performance. *ChemSusChem*. 2012;**5**:818-841. DOI: 10.1002/cssc.201100571
- [16] Chen T, Dai L. Carbon nanomaterials for high-performance supercapacitors. *Materials Today*. 2013;**16**:272-280. DOI: 10.1016/j.mattod.2013.07.002
- [17] Jost K, Dion G, Gogotsi Y. Textile energy storage in perspective. *Journal of Materials Chemistry A*. 2014;**2**:10776-10787. DOI: 10.1039/C4TA00203B
- [18] Yoon S, Lee J, Hyeon T, Oh SM. Electric double-layer capacitor performance of a new mesoporous carbon. *Journal of the Electrochemical Society*. 2000;**147**:2507-2512
- [19] Lee J, Yoon S, Oh SM, Shin C-H, Hyeon T. Development of a new mesoporous carbon using an HMS aluminosilicate template. *Advanced Materials*. 2000;**12**:359-362. DOI: 10.1002/(SICI)1521-4095(200003)12:5<359::AID-ADMA359>3.0.CO;2-1
- [20] Lee J, Yoon S, Hyeon T, Oh SM, Bum Kim K. Synthesis of a new mesoporous carbon and its application to electrochemical double-layer capacitors. *Chemical Communications*. 1999;**0**:2177-2178. DOI: 10.1039/A906872D
- [21] Lee HY, Goodenough JB. Supercapacitor behavior with KCl electrolyte. *Journal of Solid State Chemistry*. 1999;**144**:220-223. DOI: 10.1006/jssc.1998.8128
- [22] Jiang J, Li Y, Liu J, Huang X, Yuan C, Lou XWD. Recent advances in metal oxide-based electrode architecture design for electrochemical energy storage. *Advanced Materials*. 2012;**24**:5166-5180
- [23] de las Casas C, Li W. A review of application of carbon nanotubes for lithium ion battery anode material. *Journal of Power Sources*. 2012;**208**:74-85. DOI: 10.1016/j.jpowsour.2012.02.013
- [24] Etacheri V, Marom R, Elazari R, Salitra G, Aurbach D. Challenges in the development of advanced Li-ion batteries: A review. *Energy & Environmental Science*. 2011;**4**:3243-3262
- [25] Dimitrov AT, Chen GZ, Kinloch IA, Fray DJ. A feasibility study of scaling-up the electrolytic production of carbon nanotubes in molten salts. *Electrochimica Acta*. 2002;**48**:91-102. DOI: 10.1016/S0013-4686(02)00595-9
- [26] Jha VK, Matsuda M, Miyake M. Sorption properties of the activated carbon-zeolite composite prepared from coal fly ash for Ni²⁺, Cu²⁺, Cd²⁺ and Pb²⁺. *Journal of Hazardous Materials*. 2008;**160**:148-153
- [27] Ryu KS, Lee Y, Han K-S, Park YJ, Kang MG, Park N-G, et al. Electrochemical supercapacitor based on polyaniline doped with lithium salt and active carbon electrodes. *Solid State Ionics*. 2004;**175**:765-768
- [28] Luo J-Y, Xia Y-Y. Electrochemical profile of an asymmetric supercapacitor using carbon-coated LiTi₂(PO₄)₃ and active carbon electrodes. *Journal of Power Sources*. 2009;**186**:224-227
- [29] Wang Y-G, Wang Z-D, Xia Y-Y. An asymmetric supercapacitor using RuO₂/TiO₂ nanotube composite and activated carbon electrodes. *Electrochimica Acta*. 2005;**50**:5641-5646
- [30] Salitra G, Soffer A, Eliad L, Cohen Y, Aurbach D. Carbon electrodes for double-layer capacitors I. Relations between ion and pore dimensions. *Journal of the Electrochemical Society*. 2000;**147**:2486-2493
- [31] Yu M-F, Lourie O, Dyer MJ, Moloni K, Kelly TF, Ruoff RS. Strength

- and breaking mechanism of multiwalled carbon nanotubes under tensile load. *Science*. 2000;**287**:637-640
- [32] Treacy MMJ, Ebbesen TW, Gibson JM. Exceptionally high Young's modulus observed for individual carbon nanotubes. *Nature*. 1996;**381**:678
- [33] Krishnan A, Dujardin E, Ebbesen TW, Yianilos PN, Treacy MMJ. Young's modulus of single-walled nanotubes. *Physical Review B*. 1998;**58**:14013
- [34] Bandaru PR. Electrical properties and applications of carbon nanotube structures. *Journal of Nanoscience and Nanotechnology*. 2007;**7**:1239-1267
- [35] Bachtold A, Henny M, Terrier C, Strunk C, Schönemberger C, Salvetat J-P, et al. Contacting carbon nanotubes selectively with low-ohmic contacts for four-probe electric measurements. *Applied Physics Letters*. 1998;**73**:274-276
- [36] Berger C, Yi Y, Wang ZL, De Heer WA. Multiwalled carbon nanotubes are ballistic conductors at room temperature. *Applied Physics A: Materials Science & Processing*. 2002;**74**:363-365
- [37] Pop E, Mann D, Wang Q, Goodson K, Dai H. Thermal conductance of an individual single-wall carbon nanotube above room temperature. *Nano Letters*. 2006;**6**:96-100
- [38] Kim P, Shi L, Majumdar A, McEuen PL. Thermal transport measurements of individual multiwalled nanotubes. *Physical Review Letters*. 2001;**87**:215502
- [39] Behabtu N, Young CC, Tsentalovich DE, Kleinerman O, Wang X, Ma AWK, et al. Multifunctional fibers of carbon nanotubes with ultrahigh conductivity. *Science*. 2013;**339**:182-186. <http://science.sciencemag.org/content/339/6116/182.abstract>
- [40] Davis VA, Parra-Vasquez ANG, Green MJ, Rai PK, Behabtu N, Prieto V, et al. True solutions of single-walled carbon nanotubes for assembly into macroscopic materials. *Nature Nanotechnology*. 2009;**4**:830-834
- [41] Ericson LM, Fan H, Peng H, Davis VA, Zhou W, Sulpizio J, et al. Macroscopic, neat, single-walled carbon nanotube fibers. *Science*. 2004;**305**:1447-1450
- [42] Li N, Chen Z, Ren W, Li F, Cheng H-M. Flexible graphene-based lithium ion batteries with ultrafast charge and discharge rates. *Proceedings of the National Academy of Sciences*. 2012;**109**:17360-17365
- [43] Zhu N, Liu W, Xue M, Xie Z, Zhao D, Zhang M, et al. Graphene as a conductive additive to enhance the high-rate capabilities of electrospun $\text{Li}_4\text{Ti}_5\text{O}_{12}$ for lithium-ion batteries. *Electrochimica Acta*. 2010;**55**:5813-5818
- [44] Wang H, Yang Y, Liang Y, Robinson JT, Li Y, Jackson A, et al. Graphene-wrapped sulfur particles as a rechargeable lithium-sulfur battery cathode material with high capacity and cycling stability. *Nano Letters*. 2011;**11**:2644-2647
- [45] Anisuzzaman SM, Joseph CG, Daud WMABW, Krishnaiah D, Yee HS. Preparation and characterization of activated carbon from *Typha orientalis* leaves. *International Journal of Industrial Chemistry*. 2015;**6**:9-21
- [46] Hu L, Pasta M, La Mantia F, Cui L, Jeong S, Deshazer HD, et al. Stretchable, porous, and conductive energy textiles. *Nano Letters*. 2010;**10**:708-714
- [47] Yu G, Hu L, Vosgueritchian M, Wang H, Xie X, McDonough JR, et al. Solution-processed graphene/ MnO_2 nanostructured textiles for high-performance electrochemical capacitors. *Nano Letters*. 2011;**11**:2905-2911

[48] Cheng H, Dong Z, Hu C, Zhao Y, Hu Y, Qu L, et al. Textile electrodes woven by carbon nanotube–graphene hybrid fibers for flexible electrochemical capacitors. *Nanoscale*. 2013;5:3428-3434

[49] Aboutalebi SH, Jalili R, Esrafilzadeh D, Salari M, Gholamvand Z, Aminorroaya Yamini S, et al. High-performance multifunctional graphene yarns: Toward wearable all-carbon energy storage textiles. *ACS Nano*. 2014;8:2456-2466

[50] Xiao X, Li T, Yang P, Gao Y, Jin H, Ni W, et al. Fiber-based all-solid-state flexible supercapacitors for self-powered systems. *ACS Nano*. 2012;6:9200-9206

[51] Xu P, Wei B, Cao Z, Zheng J, Gong K, Li F, et al. Stretchable wire-shaped asymmetric supercapacitors based on pristine and MnO₂ coated carbon nanotube fibers. *ACS Nano*. 2015;9:6088-6096

[52] Huang Y, Hu H, Huang Y, Zhu M, Meng W, Liu C, et al. From industrially weavable and knittable highly conductive yarns to large wearable energy storage textiles. *ACS Nano*. 2015;9:4766-4775

[53] Lee JA, Shin MK, Kim SH, Cho HU, Spinks GM, Wallace GG, et al. Ultrafast charge and discharge bistructured yarn supercapacitors for textiles and microdevices. *Nature Communications*. 2013;4:1970

Fiber Supercapacitors Based on Carbon Nanotube-PANI Composites

Paa Kwasi Adusei, Yu-Yun Hsieh, Sathya Narayan Kanakaraj, Yanbo Fang, Kevin Johnson, Noe T. Alvarez and Vesselin Shanov

Abstract

Flexible and wearable electronic devices are of a high academic and industrial interest. In order to power these devices, there is a need for compatible energy storage units that can exhibit similar mechanical flexibility. Fiber-based devices have thus become increasingly popular since their light-weight, and flexible structure can be easily integrated into textiles. Supercapacitors have garnered a lot of attention due to their excellent cycling durability, fast charge times and superior power density. The primary challenge, however, with electric double layer capacitors (EDLCs), which are part of the supercapacitor family, is that their energy densities are significantly lower compared to those of batteries. Pseudocapacitors, on the other hand, can be designed and created with large energy densities and other outstanding properties typical for supercapacitors. This chapter discusses the fabrication and testing of supercapacitors based on carbon nanotube-polyaniline (PANI) composite fibers. These flexible and light-weight devices are assembled using different electrolytes for comparison. The created in this work PANI-CNT composite devices attain an energy density of 6.16 Wh/kg at a power density of 630 W/kg and retained a capacitance of 88% over 1000 charge-discharge cycles.

Keywords: pseudocapacitors, CNT Fibers, PANI, fiber supercapacitors

1. Introduction

Over the last few decades there has been an increase in research into energy storage devices arising from the ever increasing energy demands for applications such as portable electronics and electric transportation [1]. Among portable electronics, wearable electronic devices have created a niche for themselves. Fiber-based devices have become increasingly popular since their thread-type structures can be easily integrated into fabrics and other structures.

Supercapacitors are electrochemical energy storage devices that combine the high-energy-storage capability of conventional batteries with the high-power-delivery capability of traditional capacitors [2, 3]. Though they have lower stored energies than batteries, they deliver the stored energy in seconds. Supercapacitors

operate for extended periods of time, often millions of cycles without losing their energy storage capacities giving them an edge over batteries in how long they can be used [4–6].

Supercapacitors have two main classifications that are based on their charge storage mechanism and the type of electrode materials [4]. The first one, electric double layer capacitor (EDLC), stores charges electrostatically on the electrode-electrolyte interfaces of the high surface area carbon materials. This process involves physical adsorption of ions at the electrode and electrolyte interface [2]. The second one, pseudocapacitor, on the other hand, stores charges within the electrodes in response to fast surface and near-surface redox reactions [5, 7]. The electrodes are derived from transition metal oxides and conducting polymers. Due to these redox reactions, pseudocapacitors have been reported with energy densities far higher than that of EDLCs.

With the emergence of flexible electronics such as foldable displays [8], soft photo-detectors [9] and bendable field effect transistors [10], flexible supercapacitors have become more popular than ever. They have been found to be suitable in powering portable and flexible electronic devices, and several have been fabricated with lightweight, flexible and possessing high power and energy densities [11–14]. Planar format supercapacitors have been found to have larger volumes and structural limitations which impede their use in lighter, smaller and omnidirectional flexible electronic devices [15, 16]. To solve these problems, lightweight and high energy density fiber-shaped supercapacitors have been explored and fabricated [17–22].

Fiber electrodes for supercapacitors have been made from active materials with nanostructures, such as CNTs [23–25], graphene [17, 26, 27] and metal oxides [28–30]. However, the most widely studied ones have been CNT fiber electrodes and their composites. This is attributed to CNT's inherent flexibility, high surface area and high electrical conductivity [31]. In their fiber formats, they are highly aligned and have excellent mechanical durability while maintaining all their aforementioned properties.

Polyaniline (PANI) is probably the most widely studied of the conductive polymers because of its high electronic conductivity, redox and ion exchange properties, excellent environmental stability and ease of preparation [32–34]. It has, therefore, been extensively explored in energy storage devices fabricated with pseudocapacitive electrodes.

Bulk PANI, however, due to its low accessible surface area is not ideal for energy storage device electrodes. The workaround to this has been to fabricate nanostructured PANI materials. These structures have typically been made using a carbon template thereby producing materials with a large area to volume ratio and shorter ion diffusion paths [35–37].

In this chapter, we report our high energy density fiber supercapacitors based on CNT-PANI fiber composites. A chemical oxidation polymerization technique is employed to deposit PANI on the surface of the CNT fibers. This composite material gives superior performance as supercapacitor electrodes due to the fast redox reactions between the PANI and the electrolytes used. To create our CNT fibers, we employ a technique that involves dry spinning of multi-walled carbon nanotube (MWCNT) fibers from vertically aligned MWCNT arrays grown by chemical vapor deposition (CVD) as described in a previous publication by our research group [38]. This technique is used to spin continuous fiber at industrial rates from MWCNT arrays of 3 cm width and 4.25 cm length, resulting in fibers with diameters of approximately 55 μm and up to 40 m in length. Next, these fibers underwent atmospheric pressure oxygen plasma functionalization to create oxygen plasma functionalized CNT (OPFCNT) fibers as the base structure for the PANI deposition.

2. Electrode and device fabrication and characterization

2.1 Dry spinning

CNT fibers are dry spun from vertically aligned CNT arrays. In our work, thin films of Fe and Co were sputtered on a silicon wafer, overlaid with approximately 5 nm Al_2O_3 as a buffer layer, by means of physical vapor deposition (PVD). The created structure serves as a catalyst for the growth of aligned CNT arrays on the silicon wafer. This surface-treated substrate was then diced up into required pieces and then exposed to a CVD environment in a FirstNano ET3000 reactor. The resulting CNT array was drawable and spinnable and, by means of twisting and pulling. A home-made setup was used to fabricate highly aligned fibers [38], as shown in **Figure 1**. These pristine CNT fibers, when used to form EDLCs, produce quite low energy densities necessitating the deposition of PANI on them to increase the energy density.

2.2 Oxygen plasma functionalization of fibers

After the fibers were spun, they underwent an atmospheric pressure oxygen plasma functionalization process to improve the wettability of the fibers. This is necessary since carbon-based materials are naturally hydrophobic and need improved wettability to increase the deposition of PANI on the surface of the fiber during the oxidative polymerization process [39–42]. In previous publications [43, 44], carbon-based materials were treated with acids to functionalize them and thereby improve the wettability before polymerization. These involve wet chemistry and as such mostly require multi-step reactions and involve strong chemicals, which affect the bulk properties of the CNT structures. The plasma functionalization process employed in this work is continuous, effective and can be used industrially for extensive lengths of fibers.

Oxygen plasma functionalization was generated by systematically pulling the CNT fiber through a plasma head with a chamber for tubular structures (Surfx Atomflo 400 system). The set-up is shown below in **Figure 2**. The pristine CNT fiber was threaded through the plasma head and affixed to the collector bobbin with double-sided tape. The fiber was pulled through the plasma head at a speed of 0.206 cm/s using the collector bobbin on the motor. This processing led to the functionalization of the fiber with the following plasma parameters: 60 W power, 0.1 L/min oxygen and 15 L/min helium. These parameters were chosen since they ensured the fibers to be functionalized had minimum destruction, checked by Raman spectroscopy.

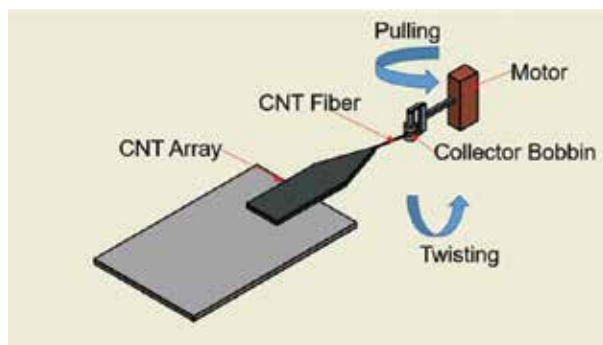


Figure 1.
Carbon nanotube fiber spinning process by twisting and pulling.

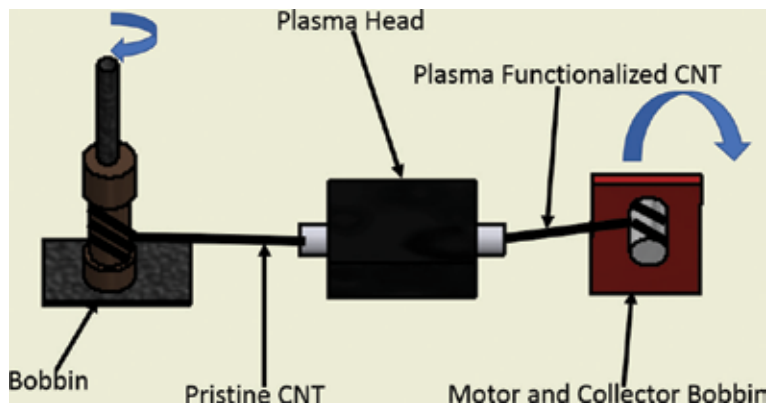


Figure 2.
Oxygen plasma functionalization set-up for CNT fibers.

2.3 Chemical oxidation polymerization

The oxidation of aniline in an acidic aqueous medium using ammonium peroxydisulfate (APS) as an oxidant is widely used and reported in the literature [45, 46]. Emeraldine salt (green color) is the form of PANI obtained during this process [32, 47]. PANI can exist in three oxidation states: leucoemeraldine (fully reduced), emeraldine (partially oxidized) and pernigraniline (fully oxidized) [32, 45–47].

At a pH of less than 2.5, the oxidative polymerization of aniline is a chain reaction [48]. The growth of the chains proceeds by the addition of the monomeric aniline molecules to the active chain ends. The chain growth is terminated after at least one of the reactants in the polymerization runs out. If there is an excess of the APS (oxidant), the resulting polymer remains in the pernigraniline form [49], especially at molar ratios of APS to aniline of over 1.5. If the rate of APS to aniline is equal to 1.25 [50] or aniline is in excess, pernigraniline is reduced to emeraldine at the end of the reaction while aniline is oxidized at the same time to emeraldine [48, 51]. We, therefore, ensured in all our tests that we had excess aniline to promote emeraldine growth, the most thermally and environmentally stable form of PANI [52–54].

The oxygen plasma functionalized CNT (OPFCNT) fibers were cut into 7.5 cm portions and affixed to copper tapes with fast drying silver paint (TedPella Inc.). The copper tapes served as the leads used to connect the devices for electrochemical testing. These electrodes were then placed into 10 ml beakers and put into an ice bath. Aniline monomer dissolved in 1 mol/L HCl and the ammonium persulphate (APS) solution also dissolved in 1 mol/L HCl were then put in the various beakers with fibers at different ratios of aniline to APS. The amount of PANI formed on the fibers was controlled by the ratio of aniline to APS used as well as the time the solution was allowed to polymerize. The fibers were taken out after the polymerization time and rinsed in a beaker with deionized water to wash off the excess PANI.

2.4 Electrode and device fabrication

Fiber supercapacitors were created using poly (vinyl alcohol) and sulfuric acid (PVA- H_2SO_4), as well as polyvinylidene fluoride-co-hexafluoropropylene and 1-ethyl-3-ethylimidazolium (PVDF-EMIMBF₄) gel electrolytes. The PVA- H_2SO_4 was made with 10 ml DI water, 2 ml H_2SO_4 and 1 g PVA. The PVDF-EMIMBF₄ gel electrolyte was prepared with 15 ml acetone, 1.5 g PVDF, and 3 ml EMIMBF₄. The PVA- H_2SO_4 was operated at a 1 V window, while the PVDF-EMIMBF₄ was operated at a 3.2 V window. The larger voltage window the PVDF-EMIMBF₄ allowed enabled

us to reach larger energy densities. Devices were made from these fibers by coating them with the gel electrolyte (PVA-H₂SO₄ or PVDF-EMIMBF₄). The fibers were then placed parallel to each other on a weighing sheet, with more electrolyte and sealed with Kapton tape.

2.5 Electrode and device characterization

Electrochemical measurements were carried out with an electrochemical workstation (Gamry, Interface 1000) at room temperature. The electrochemical characteristics of the electrodes and devices were evaluated by cyclic voltammetry at various scan rates, galvanostatic charge-discharge tests, and electrochemical impedance spectroscopy measurements from 10⁶ to 10⁻¹ Hz using sinusoidal voltage amplitude of 10 mV at the open circuit potential. In a three-electrode configuration test, Ag/AgCl was used as the reference electrode, platinum served as the counter electrode and the experiments were run in 1 M Na₂SO₄.

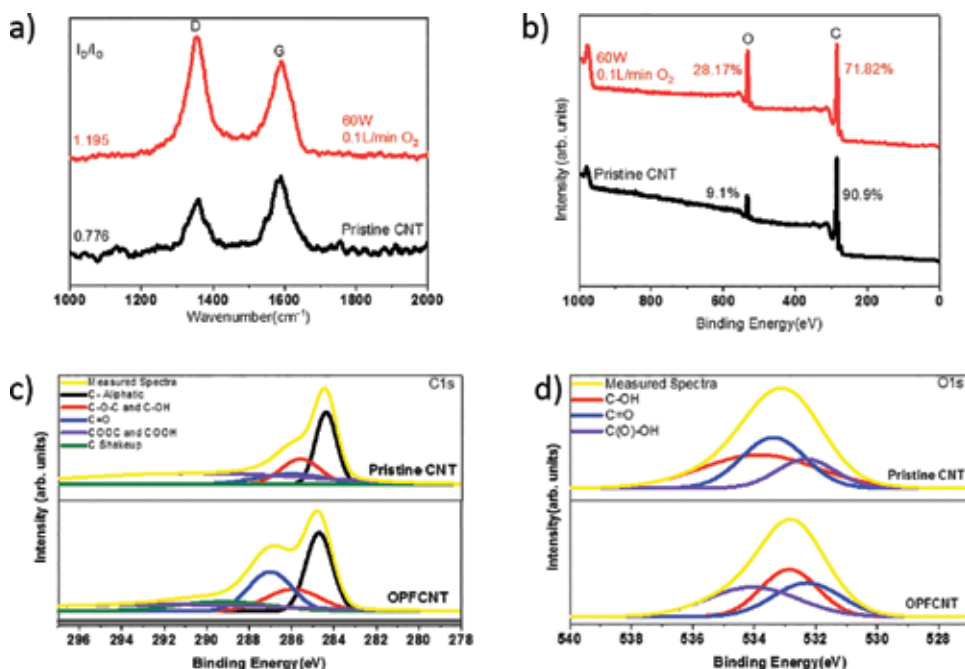
The capacitance (*C*) of the electrodes and fiber supercapacitors was calculated from the galvanostatic discharge curves at different current densities by using the equation: $C = I\Delta t / \Delta V$. The gravimetric capacitance (*C_m*) and areal capacitance (*C_A*) were calculated by the following formula: $C_m = C/m$ and $CA = C/A$, respectively. The gravimetric energy density (*E_m*) and power density (*P_m*) were calculated by the expressions: $E_m = 1/2(C_m(\Delta V)^2)/3.6$ and $P_m = 3600Em/t$. $P_m = 3600 \frac{E_m}{t}$. The areal energy density (*E_A*) and power density (*P_A*) were calculated by the expressions: $EA = 1/2(CA(\Delta V)^2)/3.6$ $E_v = \frac{1}{2} * \frac{Cv(\Delta V)^2}{3.6}$ and $PA = 3600EA/t$, $P_v = 3600 \frac{E_v}{t}$ where *I* is the discharge current, *t* is the discharge time, ΔV is the operating voltage window, *m* and *A* refer to the mass and volume of the device, respectively [40, 55].

Scanning electron microscopy (SEM) (FEI XL30, 5 kV) and Raman spectroscopy (Renishaw inVia, 514 nm Ar-ion laser with a laser spot of ~1μm²) were used to characterize the CNT-PANI. The masses of the fibers were taken on a Sartorius SE2 ultra-microbalance. X-ray photoelectron spectroscopy (XPS) data were obtained using a VG Thermo-Scientific MultiLab 3000 ultra-high vacuum surface analysis system, with ~10⁻⁹ Torr base pressure using an Al Kα source of 1486.6 eV excitation energy. The high-resolution scans for carbon and low-resolution survey scans were taken for each sample on at least two different locations.

3. Results and discussion

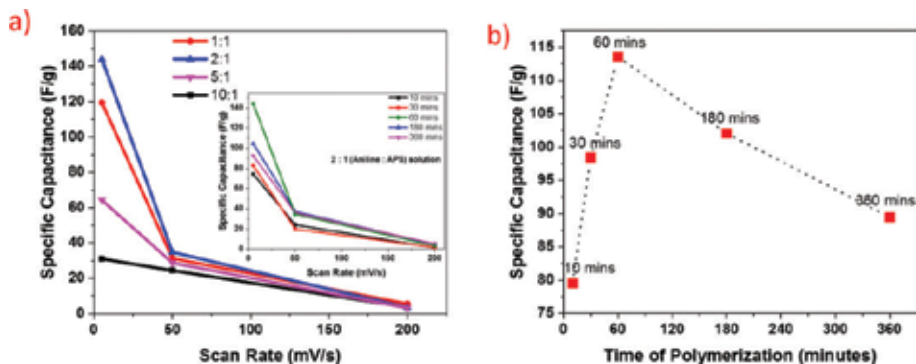
The plasma functionalization of the fiber was confirmed by Raman data **Figure 3a** and XPS data **Figure 3b–d**. From the Raman spectra in **Figure 3a**, we observe an increment in the ratio of intensities between the D and G peak, from 0.776 to 1.195, signifying the destruction of the carbon sp² bonds during plasma functionalization. In **Figure 3b**, there is a documented increase in the atomic weight percent of oxygen from 9.1% in the pristine state to 28.17% for the oxygen plasma functionalized thread. **Figure 3c** and **d** is deconvoluted high-resolution C1s and O1s peaks from the XPS data, showing the various oxygen functional groups found on the surface of the fiber which is in close agreement with data reported in the literature [39, 56].

PANI-CNT composite fibers were created from four ratios of aniline to APS (1:1, 2:1, 5:1 and 10:1). The OPFCNT fibers were placed with the chemicals as they polymerized for an hour. From our electrochemical half-cell tests, we observed that a 2:1 aniline to APS ratio gave the best specific capacitance, as seen in **Figure 4a**. Further testing of OPFCNT fibers with varying durations (10 minutes to 6 hours) of polymerization revealed that the composite fibers that


Figure 3.

(a) Raman spectra of pristine and plasma functionalized fiber; (b) XPS survey scans of pristine CNT fiber and plasma functionalized fiber; (c) high-resolution C1s scan of the pristine and plasma functionalized CNT; (d) high-resolution O1s scan of the pristine and plasma functionalized CNT.

underwent polymerization for an hour had the best electrochemistry data, as seen in the inset of **Figure 4a** and in **Figure 4b**. We observed that the polymerization of PANI increased with a higher concentration of APS as well as duration of polymerization. A 1:1 ratio therefore produced more PANI than a 2:1 ratio in the same time frame. PANI in the right amounts improves capacitance of the fibers, however when it becomes deposited in agglomerate morphologies, it leads to the inefficient usage of PANI and reduced capacitance [35–37, 46]. Thus, in the same manner, if polymerization is allowed to take place for longer time these agglomerate morphologies will form and subtract from the synergistic effects of the PANI-CNT composite.


Figure 4.

Half-cell test data for PANI-CNT composite. (a) Specific capacitance vs. scan rates for fibers created at different ratios of aniline to APS for an hour; Inset: specific capacitance vs. scan rate for 2:1 aniline to APS ratio at different times; (b) specific capacitance vs. different times for 2:1 aniline to APS ratio polymerization at 1 A/g.

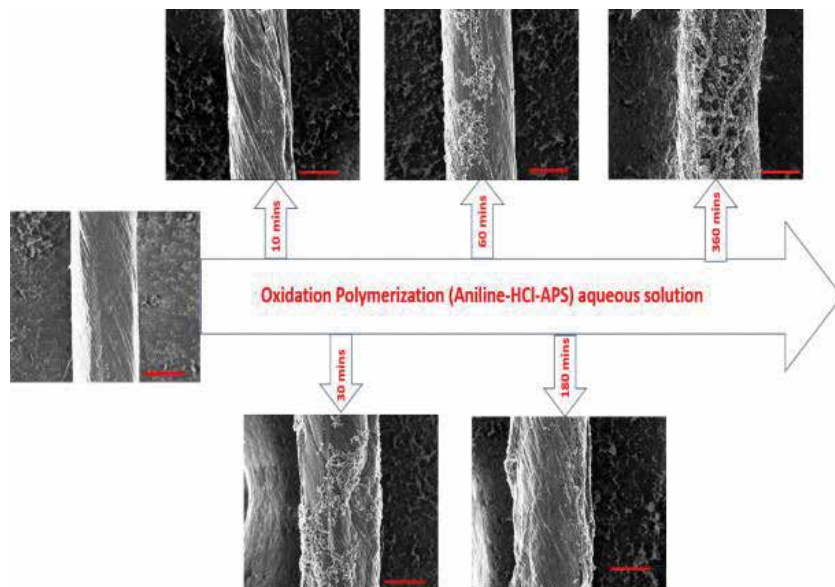


Figure 5. SEM images showing the route of polymerization of fibers up to 6 hours (magnification 1000, scale: 25 μm).

The structures of the PANI-CNT fibers were observed by SEM. The morphologies and amount of PANI formed were found to correlate strongly to the duration of the polymerization. At 10 minutes, a thin film of PANI forms across the surface of the fiber and as the duration of polymerization increases, PANI nanorods begin to develop in dendritic structures on the fiber. **Figure 5** shows SEM images of the fiber as it progresses from its pristine state to 6 hours of oxidation polymerization.

For ease of referencing, we have labeled the fibers by the number of minutes they were polymerized (minutes-PANI-CNT). **Figure 6** compares pristine CNT, 10-PANI-CNT and 360-PANI-CNT at higher magnifications to reveal the PANI structures being formed. **Figure 6a** shows the pristine fiber which has no PANI on it. In **Figure 6b** we find the onset of the formation of PANI as thin films in the fiber. The agglomerate morphologies of PANI are observed in **Figure 6c**. This shows the increment of PANI morphologies on the surface of the fibers with increasing time for polymerization.

From the Raman data presented in **Figure 7**, we observe the gradual increment in PANI formation on the composite fibers as the duration of polymerization increases. The spectra for pristine CNT and pure PANI are also incorporated, so the gradual transformation from one extreme to the other can be seen. We observe as the duration of polymerization increases the spectra becomes less like CNT and more like PANI.

Devices were created with PANI-CNT fibers, pristine CNT fibers, and OPFCNT fibers. Asymmetrical supercapacitors were also fabricated combining a PANI-CNT fiber and an OPFCNT fiber. The energy density of the PANI-CNT fiber supercapacitor was 3.77 Wh/kg at 0.5 A/g and a power density of about 188 W/kg when using PVA-H₂SO₄. These parameters were dramatically increased to 6.16 Wh/kg and 630 W/kg when using EMIMBF₄ corresponding to an almost 64% increment in energy density and 235% increment in power density. **Figure 8** presents a Ragone plot to give a more holistic view of the data as well as a comparison to other previously reported in the literature fiber supercapacitor devices. For ease of comparison, this plot was presented with the areal capacitance, as most fiber supercapacitor data is published with respect to the surface area of the electrodes [57]. The best

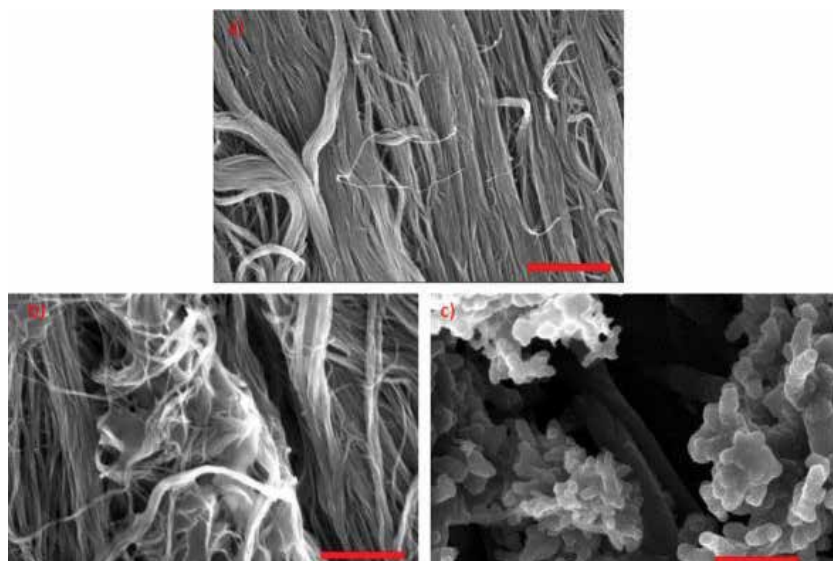


Figure 6. SEM Images at 25000 magnification (scale: 1 μm). a) Pristine CNT; b) 10-PANI-CNT; c) 360-PANI-CNT.

devices (superior energy density and power density) from this Ragone plot were observed in our asymmetric devices. The latter was attributed to the combined redox reactions between the PANI and oxygen functional groups on the surface of the fibers, as well as to the synergistic effect of the pseudocapacitance (PANI-CNT) and EDLC (OPFCNT). Oxygen functional groups have been reported in other works to have improved capacitance of carbon-based materials [58–61] and this also plays a role in the enhanced electrochemical properties of the asymmetrical device.

Figure 9 shows cyclic voltammetry graphs of all the devices at 200 and at 5 mV/s. It can be clearly seen from these graphs that the devices had the characteristic curves

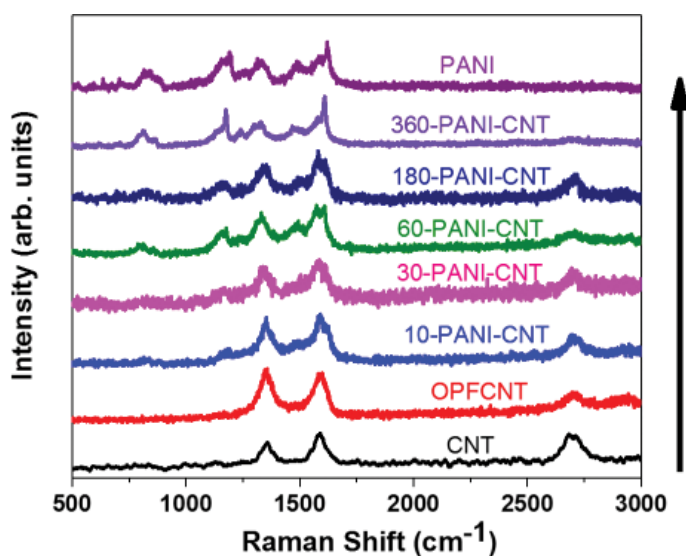


Figure 7. Raman spectra of CNT, OPFCNT and PANI-CNT composites polymerized at different times.

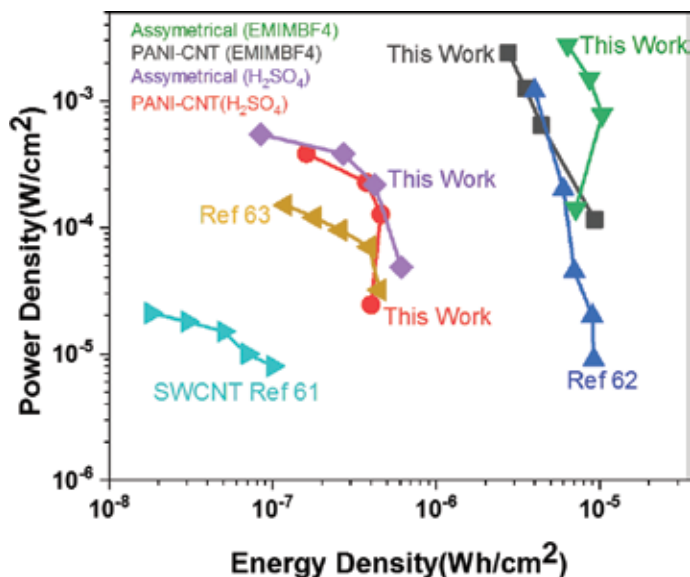


Figure 8.
 Ragone plot comparing devices with others in literature [61–63].

of supercapacitors. At lower scan rates (5 mV/s), where redox reactions are more visible, we see larger voltammetry curves for PANI doped threads.

The stability of a supercapacitor is an important parameter since its practical application can be evaluated from this data. **Figure 10** shows the cycling stability of the PANI-CNT (EMIMBF4) device over 1000 cycles. The device retains 88% of its capacitance even after 1000 charge-discharge cycles. This shows good stability and long lifetime of devices.

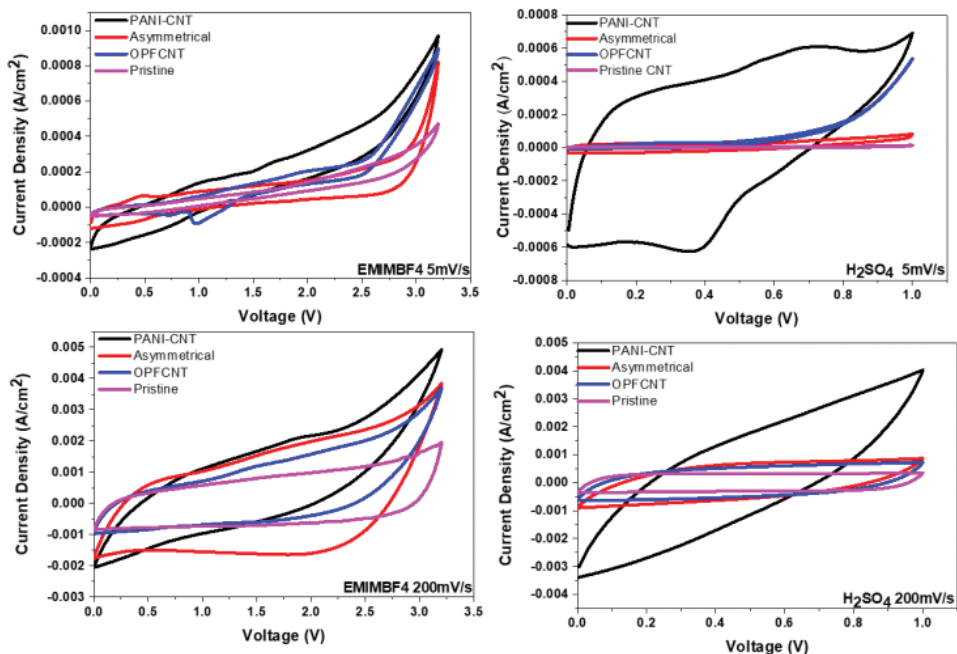


Figure 9.
 Cyclic voltammetry curves of devices at 5 and 200 mV/s.

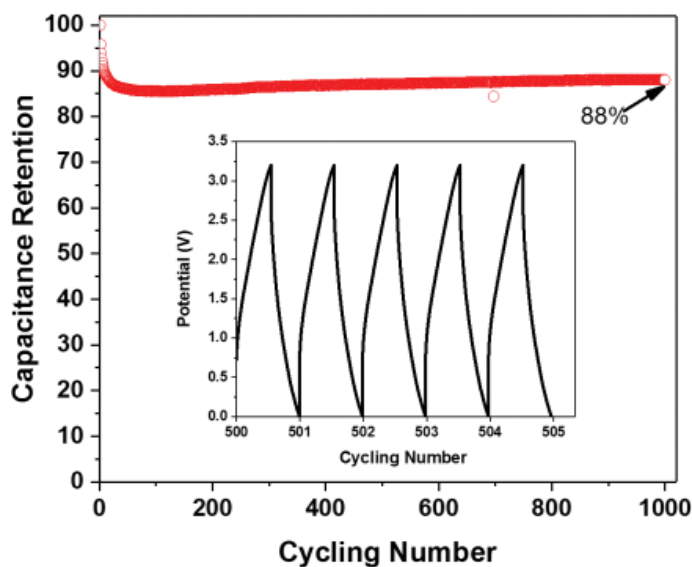


Figure 10. Cyclic stability for PANI-CNT EMIMBF₄ device Inset: galvanostatic charge/discharge curve after 500 cycles.

4. Conclusion

In this chapter, we have discussed the increased attention being given to fiber supercapacitors and their relevance to wearable electronics. We also revealed the role of carbon nanostructured fiber as energy storage devices and the challenges they face. We have successfully synthesized CNT fibers by CVD and dry spinning, applied a post-processing technique to these fibers (oxygen plasma functionalization) and by means of oxidation polymerization doped these fibers with PANI. These fibers were characterized electrochemically, by Raman spectroscopy and with SEM. These fibers were then used as electrodes to create simple fiber devices. The obtained devices produced energy densities of up to 6.16 Wh/kg and 630 W/kg when using EMIMBF₄ as electrolytes corresponding to almost a 64% increment in energy density and 335% increment in power density from devices fabricated with PVA-H₂SO₄ (3.77 Wh/kg, 188 W/kg). These devices also maintained excellent capacitance retention (88%) over 1000 charge-discharge cycles. When a comparison was however made with other devices with respect to areal energy density and power density it was observed that the asymmetrical device comprising of an OPFCNT and PANI-CNT showed the best data. This was attributed to the combined redox reactions of both the OPFCNT and PANI-CNT electrodes with the electrolyte.

Acknowledgements

This work was funded by NASA NNX13AF46A and the National Institute for Occupational Safety and Health through the Pilot Research Project Training Program of the University of Cincinnati Education and Research Center Grant # T42OH008432. One of the authors (P. K. A.) would like to thank the Department of Chemical and Environmental Engineering at UC for a partial financial support.

Conflict of interest

The authors declare there is no conflict of interest.

Author details

Paa Kwasi Adusei¹, Yu-Yun Hsieh¹, Sathya Narayan Kanakaraj¹, Yanbo Fang¹, Kevin Johnson², Noe T. Alvarez³ and Vesselin Shanov^{1,2*}

1 Department of Mechanical and Materials Engineering, University of Cincinnati, Cincinnati, OH, USA

2 Department of Chemical and Environmental Engineering, University of Cincinnati, OH, USA

3 Department of Chemistry, University of Cincinnati, OH, USA

*Address all correspondence to: vesselin.shanov@uc.edu

IntechOpen

© 2018 The Author(s). Licensee IntechOpen. This chapter is distributed under the terms of the Creative Commons Attribution License (<http://creativecommons.org/licenses/by/3.0/>), which permits unrestricted use, distribution, and reproduction in any medium, provided the original work is properly cited. 

References

- [1] Bruce PG, Freunberger SA, Hardwick LJ, Tarascon J-M. Li-O₂ and Li-S batteries with high energy storage. *Nature Materials*. 2012;**11**:19-29. DOI: 10.1038/nmat3191
- [2] Burke A. Ultracapacitors: Why, how, and where is the technology. *Journal of Power Sources*. 2000;**91**:37-50. DOI: 10.1016/S0378-7753(00)00485-7
- [3] Conway BE. *Electrochemical Supercapacitors: Scientific Fundamentals and Technical Applications*; New York: Kluwer Academics/Plenum; 1999
- [4] Beidaghi M, Gogotsi Y. Capacitive energy storage in micro-scale devices: Recent advances in design and fabrication of micro-supercapacitors. *Energy & Environmental Science*. 2014;**7**:867. DOI: 10.1039/c3ee43526a
- [5] Simon P, Gogotsi Y. Capacitive energy storage in nanostructured carbon-electrolyte systems. *Accounts of Chemical Research*. 2013;**46**:1094-1103. DOI: 10.1021/ar200306b
- [6] Frackowiak E, Khomenko V, Jurewicz K, Lota K, Béguin F. Supercapacitors based on conducting polymers/nanotubes composites. *Journal of Power Sources*. 2006;**153**:413-418. DOI: 10.1016/j.jpowsour.2005.05.030
- [7] Simon P, Gogotsi Y. Materials for electrochemical capacitors. *Nature Materials*; **2008**, **7**:845-854. DOI: 10.1038/nmat2297
- [8] Gelinck GH, Huitema HEA, van Veenendaal E, Cantatore E, Schrijnemakers L, van der Putten JBPH, et al. Flexible active-matrix displays and shift registers based on solution-processed organic transistors. *Nature Materials*. 2004;**3**:106-110. DOI: 10.1038/nmat1061
- [9] Wang X, Song W, Liu B, Chen G, Chen D, Zhou C, et al. High-performance organic-inorganic hybrid photodetectors based on P3HT:CdSe nanowire heterojunctions on rigid and flexible substrates. *Advanced Functional Materials*. 2013;**23**:1202-1209. DOI: 10.1002/adfm.201201786
- [10] Tian B, Cohen-Karni T, Qing Q, Duan X, Xie P, Lieber CM. Three-dimensional, flexible nanoscale field-effect transistors as localized bioprobes. *Science (80-)*. 2010;**329**:830-834. DOI: 10.1126/science.1192033
- [11] Lu X, Zhai T, Zhang X, Shen Y, Yuan L, Hu B, et al. WO_{3-x}@Au@MnO₂ core-shell nanowires on carbon fabric for high-performance flexible supercapacitors. *Advanced Materials*. 2012;**24**:938-944. DOI: 10.1002/adma.201104113
- [12] Huang L, Chen D, Ding Y, Feng S, Wang ZL, Liu M. Nickel-cobalt hydroxide nanosheets coated on NiCo₂O₄ nanowires grown on carbon fiber paper for high-performance pseudocapacitors. *Nano Letters*. 2013;**13**:3135-3139. DOI: 10.1021/nl401086t
- [13] Wang X, Liu B, Liu R, Wang Q, Hou X, Chen D, et al. Fiber-based flexible all-solid-state asymmetric supercapacitors for integrated photodetecting system. *Angewandte Chemie, International Edition*. 2014;**53**:1849-1853. DOI: 10.1002/anie.201307581
- [14] Liu B, Zhang J, Wang X, Chen G, Chen D, Zhou C, et al. Hierarchical three-dimensional ZnCo₂O₄ nanowire arrays/carbon cloth anodes for a novel class of high-performance flexible lithium-ion batteries. *Nano Letters*. 2012;**12**:3005-3011. DOI: 10.1021/nl300794f

- [15] Chen T, Yang Z, Peng H. Integrated devices to realize energy conversion and storage simultaneously. *Chemphyschem*. 2013;**14**:1777-1782. DOI: 10.1002/cphc.201300032
- [16] Wang X, Lu X, Liu B, Chen D, Tong Y, Shen G. Flexible energy-storage devices: Design consideration and recent progress. *Advanced Materials*. 2014;**26**:4763-4782. DOI: 10.1002/adma.201400910
- [17] Meng Y, Zhao Y, Hu C, Cheng H, Hu Y, Zhang Z, et al. All-graphene core-sheath microfibrils for all-solid-state, stretchable fibriform supercapacitors and wearable electronic textiles. *Advanced Materials*. 2013;**25**:2326-2331. DOI: 10.1002/adma.201300132
- [18] Liu B, Tan D, Wang X, Chen D, Shen G. Flexible, planar-integrated, all-solid-state fiber supercapacitors with an enhanced distributed-capacitance effect. *Small*. 2013;**9**:1998-2004. DOI: 10.1002/smll.201202586
- [19] Xiao X, Li T, Yang P, Gao Y, Jin H, Ni W, et al. Fiber-based all-solid-state flexible supercapacitors for self-powered systems. *ACS Nano*. 2012;**6**:9200-9206. DOI: 10.1021/nn303530k
- [20] Le VT, Kim H, Ghosh A, Kim J, Chang J, Vu QA, et al. Coaxial fiber supercapacitor using all-carbon material electrodes. *ACS Nano*. 2013;**7**:5940-5947. DOI: 10.1021/nn4016345
- [21] Fu Y, Cai X, Wu H, Lv Z, Hou S, Peng M, et al. Fiber supercapacitors utilizing pen ink for flexible/wearable energy storage. *Advanced Materials*. 2012;**24**:5713-5718. DOI: 10.1002/adma.201202930
- [22] Xu P, Gu T, Cao Z, Wei B, Yu J, Li F, et al. Carbon nanotube fiber based stretchable wire-shaped supercapacitors. *Advanced Energy Materials*. 2014;**4**:1300759(1-6). DOI: 10.1002/aenm
- [23] Wang K, Meng Q, Zhang Y, Wei Z, Miao M. High-performance two-ply yarn supercapacitors based on carbon nanotubes and polyaniline nanowire arrays. *Advanced Materials*. 2013;**25**:1494-1498. DOI: 10.1002/adma.201204598
- [24] Ren J, Li L, Chen C, Chen X, Cai Z, Qiu L, et al. Twisting carbon nanotube fibers for both wire-shaped micro-supercapacitor and micro-battery. *Advanced Materials*. 2013;**25**:1155-1159. DOI: 10.1002/adma.201203445
- [25] Su F, Miao M, Niu H, Wei Z. Gamma-irradiated carbon nanotube yarn as substrate for high-performance fiber supercapacitors. *ACS Applied Materials & Interfaces*. 2014;**6**:2553-2560. DOI: 10.1021/am404967x
- [26] Zhao X, Zheng B, Huang T, Gao C. Graphene-based single fiber supercapacitor with a coaxial structure. *Nanoscale*. 2015;**7**:032001-20. DOI: 10.1039/c5nr01737h
- [27] Aboutalebi SH, Jalili R, Esrafilzadeh D, Salari M, Gholamvand Z, Yamini SA, et al. High-performance multifunctional graphene yarns: Toward wearable all-carbon energy storage textiles. *ACS Nano*. 2014;**8**:2456-2466. DOI: 10.1021/nn406026z
- [28] Su F, Miao M. Asymmetric carbon nanotube-MnO₂ two-ply yarn supercapacitors for wearable electronics. *Nanotechnology*. 2014;**25**:135401. DOI: 10.1088/0957-4484/25/13/135401
- [29] Choi C, Kim SH, Sim HJ, Lee JA, Choi AY, Kim YT, et al. Stretchable, weavable coiled carbon nanotube/MnO₂/polymer fiber solid-state supercapacitors. *Scientific Reports*. 2015;**5**:1-6. DOI: 10.1038/srep09387
- [30] Bae J, Park YJ, Lee M, Cha SN, Choi YJ, Lee CS, et al. Single-fiber-based hybridization of energy converters

and storage units using graphene as electrodes. *Advanced Materials*. 2011;**23**:3446-3449. DOI: 10.1002/adma.201101345

[31] Chen T, Qiu L, Kia HG, Yang Z, Peng H. Designing aligned inorganic nanotubes at the electrode interface: Towards highly efficient photovoltaic wires. *Advanced Materials*. 2012;**24**:4623-4628. DOI: 10.1002/adma.201201893

[32] Sapurina I, Stejskal J. The mechanism of the oxidative polymerization of aniline and the formation of supramolecular polyaniline structures. *Polymer International*. 2008;**57**:1295-1325. DOI: 10.1002/pi

[33] Gospodinova N, Terlemezyan L. Conducting polymers prepared by oxidative polymerization: Polyaniline. *Progress in Polymer Science*. 1998;**23**:1443-1484. DOI: 10.1016/S0079-6700(98)00008-2

[34] Syed AA, Dinesan MK. Review: Polyaniline-A novel polymeric material. *Talanta*. 1991;**38**:815-837. DOI: 10.1016/0039-9140(91)80261-W

[35] Simotwo SK, Delre C, Kalra V. Supercapacitor electrodes based on high-purity electrospun polyaniline and polyaniline-carbon nanotube nanofibers. *ACS Applied Materials & Interfaces*. 2016;**8**:21261-21269. DOI: 10.1021/acsami.6b03463

[36] Wang X, Liu D, Deng J, Duan X, Guo J, Liu P. Improving cyclic stability of polyaniline by thermal crosslinking as electrode material for supercapacitors. *RSC Advances*. 2015;**5**:78545-78552. DOI: 10.1039/C5RA17327B

[37] Cho S, Shin K-H, Jang J. Enhanced electrochemical performance of highly porous supercapacitor electrodes based on solution processed polyaniline thin films. *ACS Applied Materials &*

Interfaces. 2013;**5**:9186-9193. DOI: 10.1021/am402702y

[38] Alvarez NT, Miller P, Haase M, Kienzle N, Zhang L, Schulz MJ, et al. Carbon nanotube assembly at near-industrial natural-fiber spinning rates. *Carbon N Y*. 2015;**86**:350-357. DOI: 10.1016/j.carbon.2015.01.058

[39] Malik R, Mcconnell C, Alvarez NT, Haase M, Shanov V. RSC advances rapid, in situ plasma functionalization of carbon nanotubes for improved CNT/epoxy composites. *RSC Advances*. 2016;**6**:108840-108850. DOI: 10.1039/C6RA23103A

[40] Zhang L, DeArmond D, Alvarez NT, Malik R, Oslin N, McConnell C, et al. Flexible micro-supercapacitor based on graphene with 3D structure. *Small*. 2017;**13**:1-10. DOI: 10.1002/sml.201603114

[41] Lobo AO, Ramos SC, Antunes EF, Marciano FR, Trava-Airoldi VJ, Corat EJ. Fast functionalization of vertically aligned multiwalled carbon nanotubes using oxygen plasma. *Materials Letters*. 2012;**70**:89-93. DOI: 10.1016/j.matlet.2011.11.071

[42] Yu H, Cheng D, Williams TS, Severino J, De Rosa IM, Carlson L, et al. Rapid oxidative activation of carbon nanotube yarn and sheet by a radio frequency, atmospheric pressure, helium and oxygen plasma. *Carbon N Y*. 2013;**57**:11-21. DOI: 10.1016/j.carbon.2013.01.010

[43] Ramana GV, Srikanth VVSS, Padya B, Jain PK. Carbon nanotube-polyaniline nanotube core-shell structures for electrochemical applications. *European Polymer Journal*. 2014;**57**:137-142. DOI: 10.1016/j.eurpolymj.2014.05.018

[44] Zhang Y, Cui X, Zu L, Cai X, Liu Y, Wang X, et al. New supercapacitors based on the synergetic redox effect

between electrode and electrolyte. *Materials* (Basel). 2016;**9**:1-13. DOI: 10.3390/ma9090734

[45] Lim YJ, Park MY, Lee SK, Lee WK, Jo NJ. Polyaniline and multi-walled carbon nanotube composite electrode for rechargeable battery. *Transactions of the Nonferrous Metals Society of China (English Ed)*. 2012;**22**:s717-s721. DOI: 10.1016/S1003-6326(12)61793-2

[46] Wang H, Lin J, Shen ZX. Polyaniline (PANi) based electrode materials for energy storage and conversion. *Journal of Science: Advanced Materials and Devices*. 2016;**1**:225-255. DOI: 10.1016/j.jsamd.2016.08.001

[47] Simotwo SK, Kalra V. Polyaniline-based electrodes: Recent application in supercapacitors and next generation rechargeable batteries. *Current Opinion in Chemical Engineering*. 2016;**13**:150-160. DOI: 10.1016/j.coche.2016.09.001

[48] Stejskal J, Kratochvíl P, Jenkins AD. The formation of polyaniline and the nature of its structures. *Polymer (Guildf)*. 1996;**37**:367-369. DOI: 10.1016/0032-3861(96)81113-X

[49] Manohar SK, Macdiarmid AG, Epstein AJ. Polyaniline: Pernigraniline, an isolable intermediate in the conventional chemical synthesis of emeraldine. *Synthetic Metals*. 1991;**41**:711-714. DOI: 10.1016/0379-6779(91)91165-7

[50] Stejskal J, Gilbert RG. Polyaniline. Preparation of a conducting polymer (IUPAC Technical Report). *Pure and Applied Chemistry*. 2002;**74**:857867. DOI: 10.1351/pac200274050857

[51] Kolla HS, Surwade SP, Zhang X, MacDiarmid AG, Manohar SK. Absolute molecular weight of polyaniline. *Journal of the American Chemical Society*. 2005;**127**:16770-16771. DOI: 10.1021/ja055327k

[52] Brožová L, Holler P, Kovářová J, Stejskal J, Trchová M. The stability of

polyaniline in strongly alkaline or acidic aqueous media. *Polymer Degradation and Stability*. 2008;**93**:592-600. DOI: 10.1016/j.polymdegradstab.2008.01.012

[53] Blinova NV, Sapurina I, Klimovič J, Stejskal J. The chemical and colloidal stability of polyaniline dispersions. *Polymer Degradation and Stability*. 2005;**88**:428-434. DOI: 10.1016/j.polymdegradstab.2004.11.014

[54] Prokeš J, Stejskal J. Polyaniline prepared in the presence of various acids: 2. Thermal stability of conductivity. *Polymer Degradation and Stability*. 2004;**86**:187-195. DOI: 10.1016/j.polymdegradstab.2004.04.012

[55] Owusu KA, Qu L, Li J, Wang Z, Zhao K, Yang C, et al. Low-crystalline iron oxide hydroxide nanoparticle anode for high-performance supercapacitors. *Nature Communications*. 2017;**8**:1-11. DOI: 10.1038/ncomms14264

[56] Zschoerper NP, Katzenmaier V, Vohrer U, Haupt M, Oehr C, Hirth T. Analytical investigation of the composition of plasma-induced functional groups on carbon nanotube sheets. *Carbon N Y*. 2009;**47**:2174-2185. DOI: 10.1016/j.carbon.2009.03.059

[57] Gogotsi Y, Simon P. True performance metrics in electrochemical energy storage. *Materials Science*. 2011;**334**:917-918. DOI: 10.1126/science.1213003

[58] Nian YR, Teng H. Influence of surface oxides on the impedance behavior of carbon-based electrochemical capacitors. *Journal of Electroanalytical Chemistry*. 2003;**540**:119-127. DOI: 10.1016/S0022-0728(02)01299-8

[59] Hsieh CT, Teng H. Influence of oxygen treatment on electric double-layer capacitance of activated carbon fabrics. *Carbon N Y*. 2002;**40**:667-674. DOI: 10.1016/S0008-6223(01)00182-8

[60] Centeno TA, Stoeckli F. On the specific double-layer capacitance of activated carbons, in relation to their structural and chemical properties. *Journal of Power Sources*. 2006;**154**:314-320. DOI: 10.1016/j.jpowsour.2005.04.007

[61] Meng J, Nie W, Zhang K, Xu F, Ding X, Wang S, et al. Enhancing electrochemical performance of graphene fiber-based supercapacitors by plasma treatment. *ACS Applied Materials & Interfaces*. 2018::acsami.8b04438. DOI: 10.1021/acsami.8b04438

[62] Huang Y, Hu H, Huang Y, Zhu M, Meng W, Liu C, et al. From industrially weavable and knittable highly conductive yarns to large wearable energy storage textiles. *ACS Nano*. 2015;**9**:4766-4775. DOI: 10.1021/acsnano.5b00860

[63] Meng Q, Wang K, Guo W, Fang J, Wei Z, She X. Thread-like supercapacitors based on one-step spun nanocomposite yarns. *Small*. 2014;**10**:3187-3193. DOI: 10.1002/sml.201303419

Deterioration Factors of Electric Double-Layer Capacitors Obtained from Voltage Hold Test

Daisuke Tashima

Abstract

A chemical analysis was carried out before and after a constant voltage hold test (applied at 2.5, 2.8, 3.0, and 3.2 V individually for 1 week) that was an acceleration deterioration examination to clarify the deterioration factors of electric double-layer capacitors. The results showed that the stress test slightly raised the internal resistances and decreased the capacitances. It was also confirmed that a range of fluorochemicals was formed on the electrode surface for approximately 10–13 nm in depth using electron spectroscopy for chemical analysis. From a chemical analysis of the electrolyte using an inductively coupling plasma-optical emission spectrometer (ICP-OES), it was confirmed that the electrolyte included Si, which is an ingredient element of an electrode, and that the increase in the holding voltage during the stress test decreased the Si density in the electrolyte.

Keywords: deterioration factor, electric double-layer capacitors, voltage hold test

1. Introduction

In contrast to chemical batteries, electric double-layer capacitors (EDLCs) store and release electrical energy by utilizing the physical adsorption and desorption of an electric charge, but without utilizing any chemical reactions. Compared to chemical batteries, EDLCs have superior responsiveness, and since they allow for rapid high-voltage charging and discharging, they are high-performance device, last through a high number of charging/discharging cycles, and theoretically do not deteriorate. Owing to these advantages, EDLCs have recently been utilized as auxiliary power supplies in hybrid electric vehicles (HEVs), which combine an internal combustion engine and an electric motor with the aim of being maintenance free. However, performance degradation has recently been confirmed in commercially used EDLCs owing to overvoltage and high temperatures, including a decrease in capacitance and an increase in internal resistance. To confirm these phenomena and to predict degradation mechanism, chemical and electrochemical aging test were performed using original electrode under acetonitrile (AN)-based electrolyte, propylene carbonate (PC)-based electrolyte [1–7], and ionic liquid as electrolyte [8]. It was also reported that aging model was calculated and aging diagnosis was built up using manufactured EDLCs under overvoltage and high-temperature condition [9–20]. For this chapter, we performed a voltage hold test, which is a type of accelerated degradation test for EDLCs using the application of overvoltage, on

cylindrical EDLCs, which are used in actual applications [21]. We confirmed the degradation behaviors caused by the application of overvoltage by measuring the capacitance and internal resistance before and after the tests. Moreover, we disassembled the EDLCs once testing was complete and ran a variety of analyses on the polarizable electrodes and the electrolytes that form its constituent parts. By comparing and studying the analytical results and the deterioration behaviors, we studied the deterioration mechanism of EDLCs.

2. Experimental method

As shown in **Table 1**, voltage hold tests were conducted by applying overvoltages of 2.8, 2.9, 3.0, 3.2, and 3.5 V continuously for 1 week to commercially used cylindrical EDLCs with a rated voltage of 2.5 V. Using a Sanyo Electric Co., Ltd., incubator (MIR-254) and a charging/discharging tester (PS-97010) by PowerSystem Co., Ltd., three accelerated deterioration samples were produced for each voltage at a constant temperature of 25°C.

Rated voltage [V]	2.5				
Rated capacitance [kF]	1.2				
Size	Height: 150 mm, Diameter: 40 mm				
Type	Cylindrical				
Holding voltage [V]	2.8	2.9	3.0	3.2	3.5
Number of samples	3	3	3	3	3

Table 1.
Experimental conditions and sample properties.

3. Measuring capacitance and internal resistance

3.1 Measuring method of capacitance and internal resistance

Before and after the voltage hold test, charging and discharging were performed at a constant current of 6 A and a voltage of 2.5 V using a stabilized DC power supply (PAN60-6A) and an electronic load device (PLZ603WH) by Kikusui Electronics Corp. Using the energy conversion method, the capacitance was calculated based on the obtained charge and discharge waveforms, and the internal resistance was calculated based on the voltage drop.

3.2 Measuring results of capacitance and internal resistance

Figure 1 shows the variance in the capacitance and internal resistance before and after the voltage hold test for each holding voltage. The internal resistance increased most for a holding voltage of 3.5 V, with a rise of approximately 30% compared to

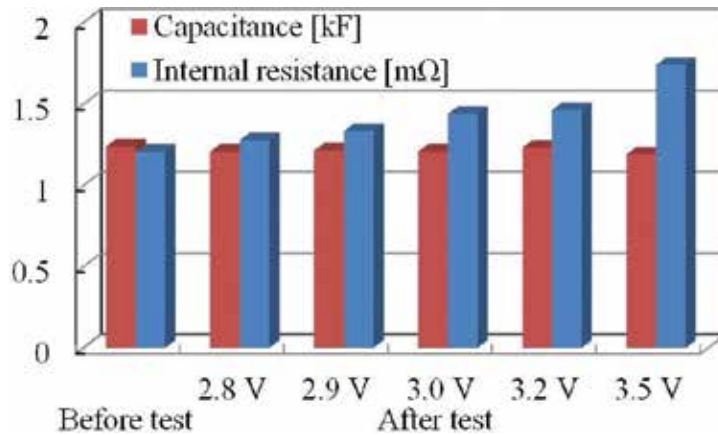


Figure 1.
Pre/postvoltage hold test properties for each applied voltage.

the value prior to the voltage hold test. Regardless of the holding voltage, the capacitance did not vary significantly from that before the test. Based on this, it was found that the rise in the holding voltage during the voltage hold test greatly affected the factors that cause an increase in the internal resistance.

4. Chemical analysis of polarizable electrodes

For qualitative and state analyses of the polarizable electrodes, we used an X-ray photoelectron spectroscopy (XPS) analysis device [electron spectroscopy for chemical analysis (ESCA-3300)] by Shimadzu Corporation. A scanning electron microscope (S-5500) by Hitachi Ltd. was used to observe the polarizable electrode surfaces.

4.1 Polarizable electrode surface observation

Figure 2(a) and **(b)** shows scanning electron microscopy (SEM) images for the polarizable electrode surfaces during the pretest. Granular electrically conducting material can be confirmed through the images. Furthermore, it was found that the polarizable electrodes consist of activated carbon and electrically conducting material, and it was confirmed that there is no variance between the positive and negative electrodes. **Figure 2(c)–(1)** is SEM images for the posttest polarizable electrode surfaces for each holding voltage. It is clear from **Figure 2(a)** and **(d)** that when comparing the pretest polarizable electrode surfaces with those after testing at a holding voltage of 2.8 V, there is no variance in the activated carbon and electrically conducting materials. However, based on **Figure 2(e)–(1)**, for polarizable electrode surfaces after tests at holding voltages of 2.9, 3.0, 3.2, and 3.5 V, both an increase in the holding voltage and a deformation of the surfaces of the positive and negative electrodes can be confirmed. Surface irregularities can be confirmed for the positive electrodes, as well as the generation of a deposit layer on the surface. Moreover, the generation of granules smaller than the electrically conducting material can be confirmed on the negative electrodes. Accordingly, it is believed that deposits produced through a reaction of some sort inside the EDLC cell cause an increase in the internal resistance [5–7, 12].

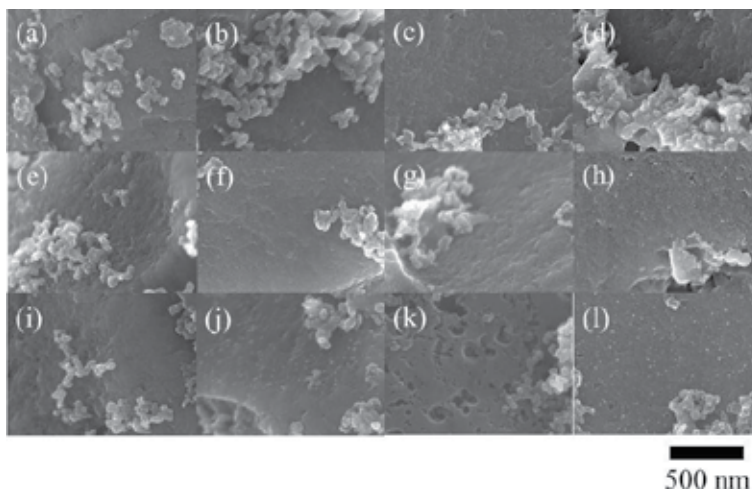


Figure 2.

Polarizable electrode surface (a) positive electrode (PE) before test, (b) negative electrode (NE) before test, (c) PE after test at holding voltage of 2.8 V, (d) NE after test at holding voltage of 2.8 V, (e) PE after test at holding voltage of 2.9 V, (f) NE after test at holding voltage of 2.9 V, (g) PE after test at holding voltage of 3.0 V, (h) NE after test at holding voltage of 3.0 V, (i) PE after test at holding voltage of 3.2 V, (j) NE after test at holding voltage of 3.2 V, (k) PE after test at holding voltage of 3.5 V, and (l) NE after test at holding voltage of 3.5 V.

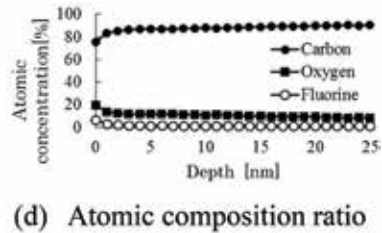
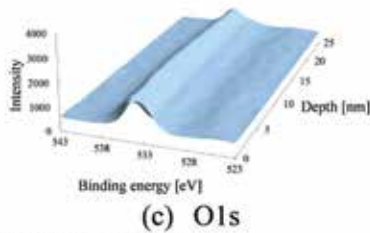
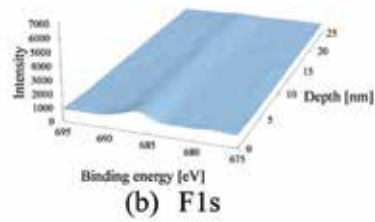
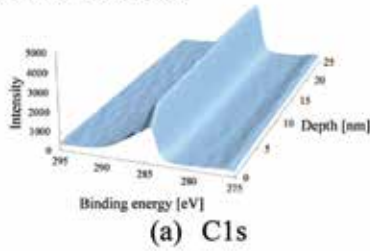
4.2 Analysis of elements existing on polarizable electrodes

Qualitative analysis results show that no major spectral differences can be seen based on observations of the pretest polarizable electrodes and posttest polarizable electrodes for each holding voltage, and that the observations chiefly consist of three elements: carbon, fluorine, and oxygen. It follows that the deposits observed on the electrode surface are fluorine, oxygen, and carbon derived. To reveal how the deposits, which consist of the same elements as the polarizable electrodes, cause a reduction in performance of the EDLC, we conducted a more detailed state analysis of the electrode surfaces. It is believed that owing to the holding voltage in the voltage hold test (an accelerated deterioration test), a change of some sort is caused in the binding states of carbon, fluorine, and oxygen. We, therefore, applied an etching process to the electrode surface and measured the changes in spectral intensity in the depth direction for C1s, O1s, and F1s, thus studying to what depth the electrode surface deposits were produced.

Figures 3–8 show the variance in the observed spectral intensity in the depth direction for (a) C1s, (b) F1s, and (c) O1s on positive electrode and (e) C1s, (f) F1s, and (g) O1s on negative electrode. Furthermore, (d) and (h) show the atomic composition ratios on positive electrode and negative electrode, respectively. It is clear from **Figure 3** that for the polarizable electrodes before the voltage hold test, the positive and negative electrodes consist of carbon, oxygen, and fluorine until a depth of 25 nm from the surface. Furthermore, since the composition ratio from approximately 2–3 nm below from the electrode surface is stable, it is thought that a 2–3 nm film exists on the polarizable electrodes. It is believed that since the cell interior was exposed to electrolytes prior to the polarizable electrodes being chosen, the polarizable electrodes reacted with the oxygen and the fluorine in the electrolyte at the solid-fluid interface.

No large difference is seen between the pre- and postvoltage hold-test polarizable electrodes at a holding voltage of 2.8 V. However, as shown in **Figure 5**, after the

Positive electrode



Negative electrode

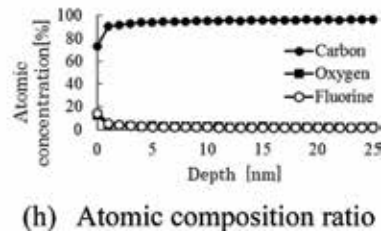
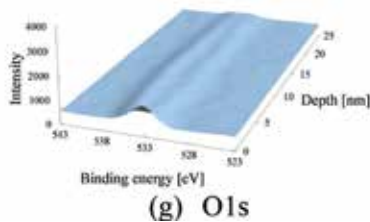
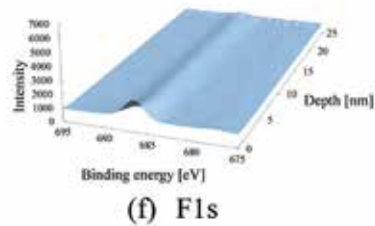
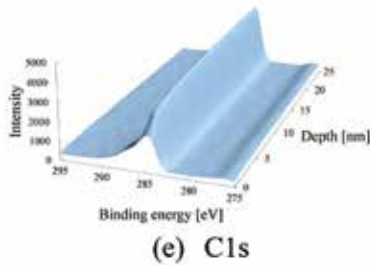
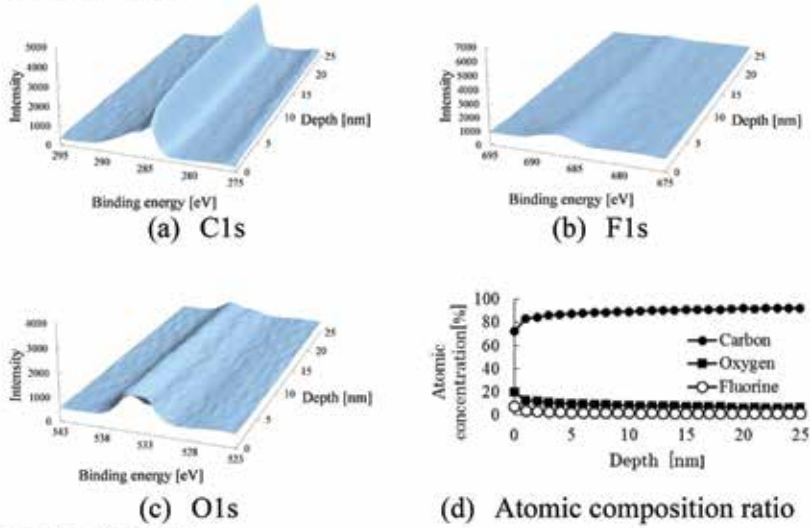


Figure 3.
Pretest polarizable electrode.

voltage hold test at a holding voltage of 2.9 V, the O1s spectral intensity decreased and the F1s spectral intensity increased. Graphs (d) in **Figure 5** show that they almost only consist of carbon and fluorine up to a depth of 15 nm. Accordingly, it is believed that through the application of voltages of 2.9 V and higher, the bond between carbon and oxygen in the polarizable electrodes is broken, and oxygen atoms are released. Moreover, since there is virtually no change in the composition ratio at a depth of approx. 10–13 nm from the surface, it is clear that the fluorine compound layer has increased in thickness compared to that before the test. Since this reactant consists of carbon and fluorine [5], it is believed to be graphite fluoride. It can be inferred from the fact that graphite fluoride is an insulator that the electrode resistance was caused to increase, thus causing the internal resistance

Positive electrode



Negative electrode

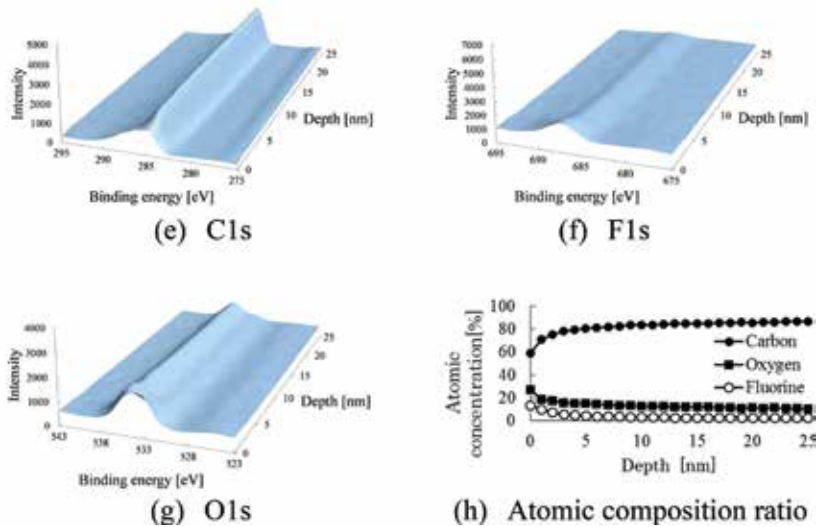


Figure 4. Polarizable electrode after test with holding voltage of 2.8 V

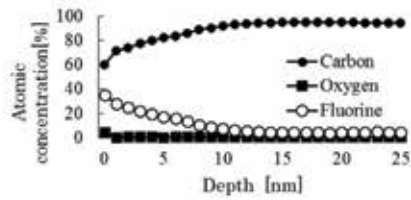
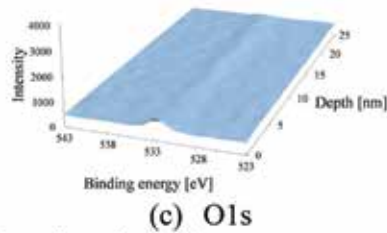
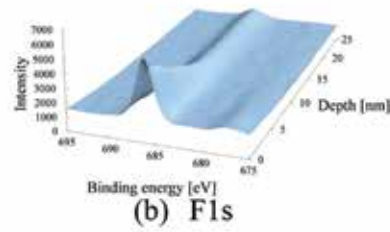
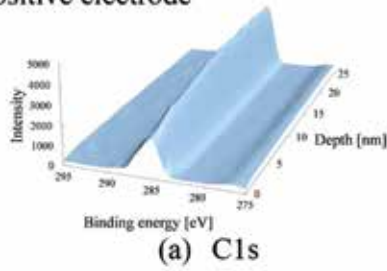
to increase. Furthermore, it was shown that no major difference was seen in the composition changes in the depth direction of the positive and negative electrodes.

5. Chemical analysis of electrolyte

5.1 Measuring moisture content of electrolyte

It was shown that in samples subject to high voltage, the electrolyte reacts with the polarizable electrode at the solid-fluid interface, altering the atomic composition ratio of the polarizable electrode. Moreover, since the reaction at the solid-fluid interface accelerates with an increase in the applied voltage, it can be inferred that some sort of change is also occurring in the electrolyte. We, therefore, measured the

Positive electrode



Negative electrode

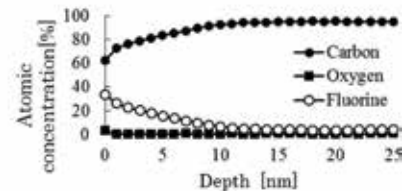
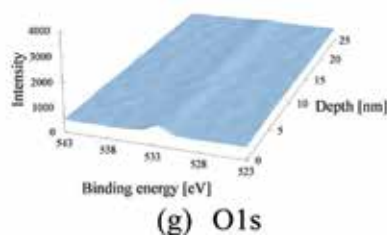
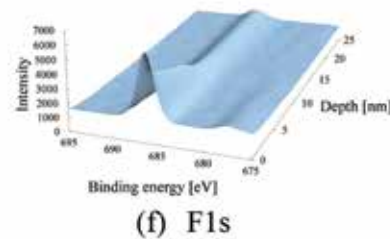
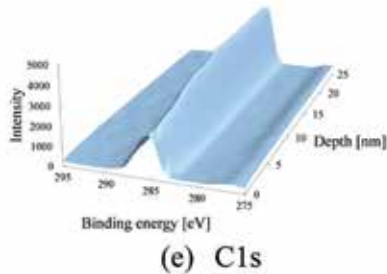


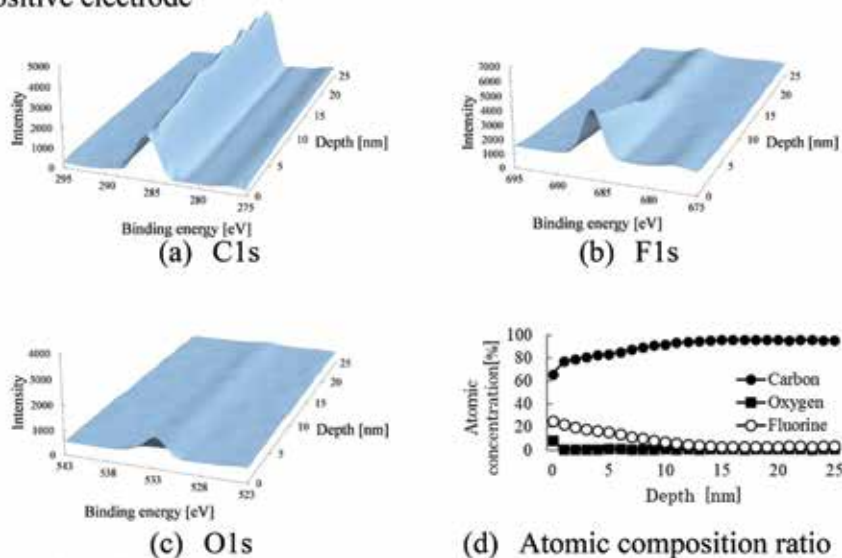
Figure 5. Polarizable electrode after test with holding voltage of 2.9 V.

moisture content in the electrolyte taken from the EDLCs. A Karl Fischer Moisture Titrator (MKC-610) by Kyoto Electronics Manufacturing Co., Ltd., was used for these measurements.

5.2 Moisture content of electrolyte: measurement results

Figure 9 shows the moisture content in the electrolyte taken from the EDLCs before the tests and after the tests at each applied voltage. A comparison of moisture content in the electrolyte before and after the test when 2.8 V is applied found an increase of approximately 14.4%. However, it was found that compared to the value before the test, the moisture content decreased after tests that applied 2.9, 3.0, 3.2, and 3.5 V. The lowest moisture content was seen in the electrolyte after the 2.9-V

Positive electrode



Negative electrode

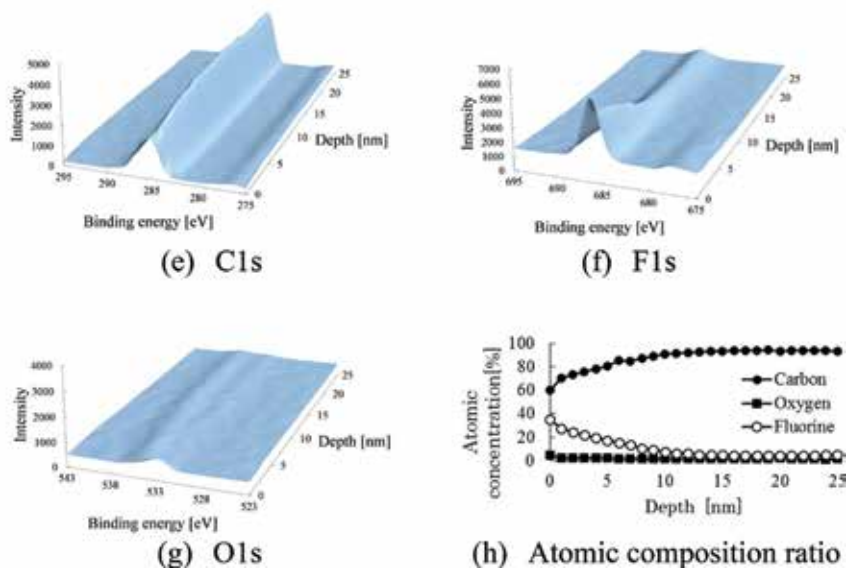


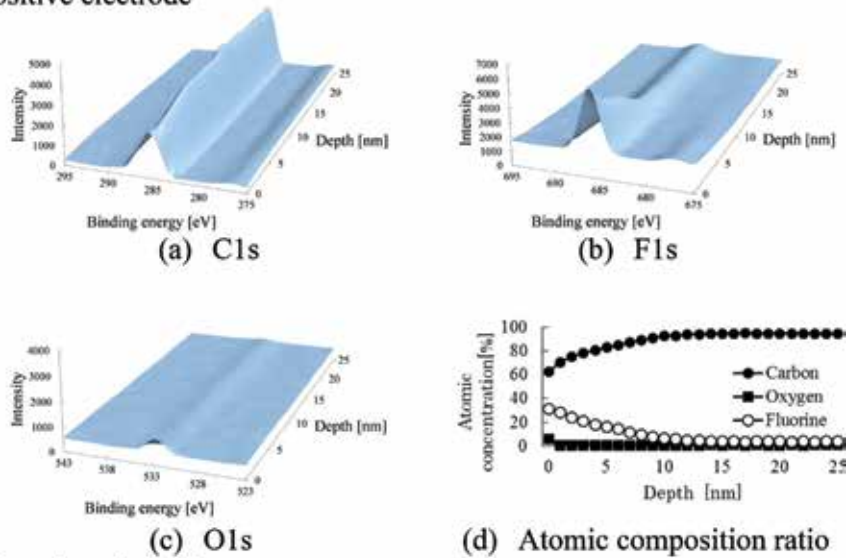
Figure 6. Polarizable electrode after test with holding voltage of 3.0 V.

test, with a 16.9% decrease compared to that before the test. Based on these results, it is believed that there is no correlation between increasing the applied voltage and decreasing the moisture content, and that the moisture content included when the EDLCs were built is retained.

5.3 Measuring electrolyte element concentrations

It was revealed that there was no correlation between an increase in the holding voltage in the voltage hold test and an increase or decrease in the moisture content shown in **Figure 9**. Accordingly, any chemical changes in the electrolyte owing to an increased holding voltage can be considered to be other than moisture related. The elution of electrode material into the electrolyte sometimes occurs during

Positive electrode



Negative electrode

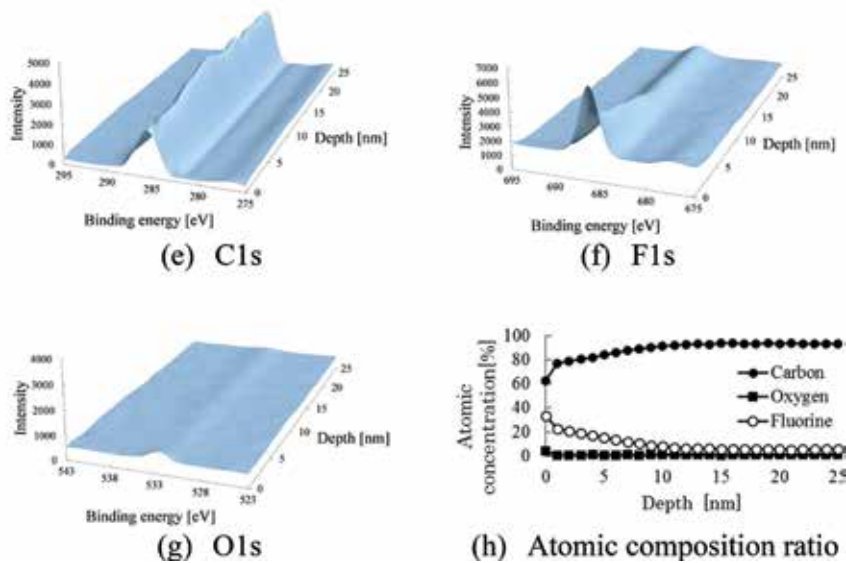
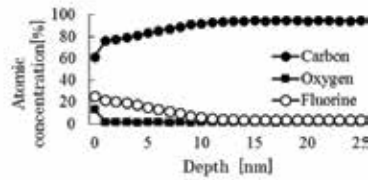
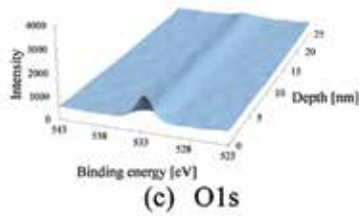
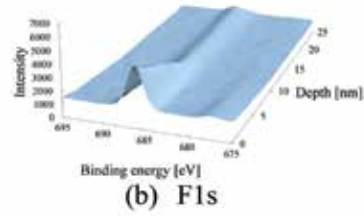
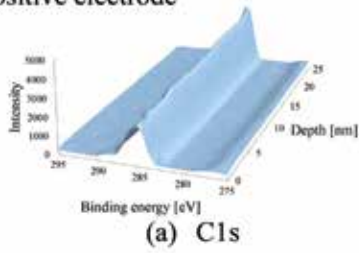


Figure 7.
 Polarizable electrode after test with holding voltage of 3.2 V.

electrolysis and is also applied in electrolytic refining. Chemical reactions of the electrodes are not desirable in EDLCs, and a mere action through physical adsorption and desorption are considered ideal [14]. However, the behavior of components contained in ash that cannot be eliminated in the activated carbon generation process is worth noting.

Owing to the difference in viscosity between the harvested electrolyte and the oil-based 23 element standard solution by Seishin Trading Co., Ltd., used in the calibration curve method, the interference must be suppressed. Moreover, since the volume required for analysis (15 ml) was not reached, this needed to be adjusted. To that end, microwave-assisted decomposition was performed using a microwave digestion device (SpeedWave MS3) by Actac Project Services Corporation, adding 8 ml of nitric acid to 0.1 ml of electrolyte. Since this decomposition treatment was performed in a closed

Positive electrode



Negative electrode

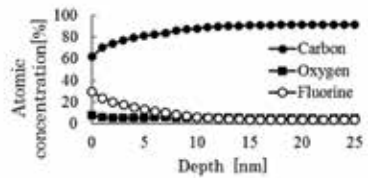
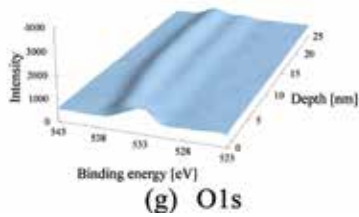
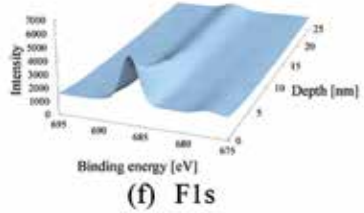
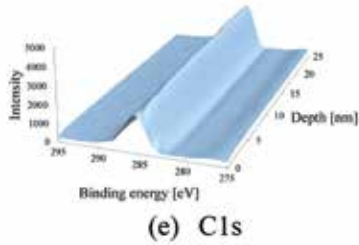


Figure 8. Polarizable electrode after test with holding voltage of 3.5 V.

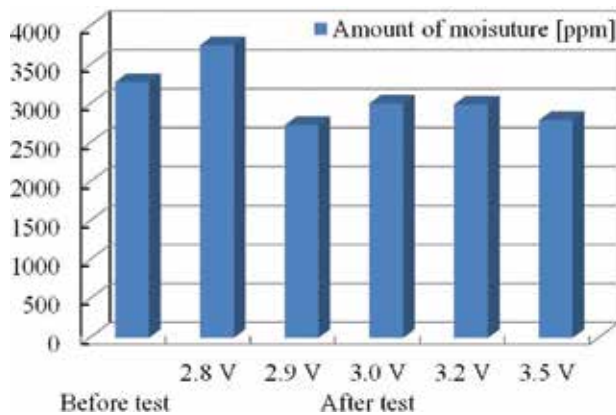
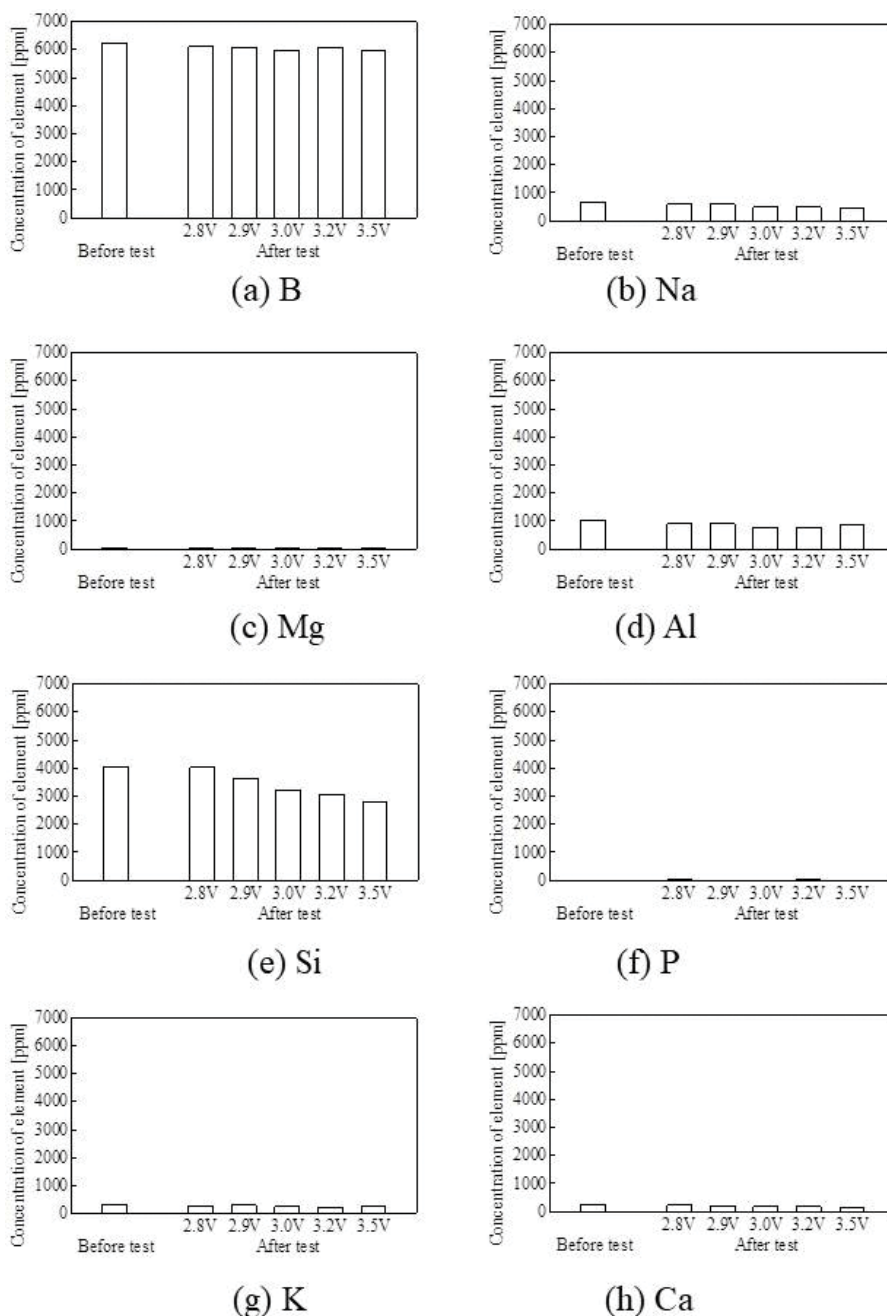


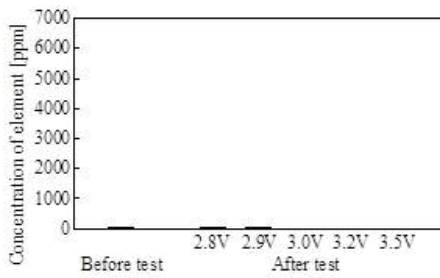
Figure 9. Moisture content in electrolyte before and after test for each applied voltage.

system, we considered external element contamination to be almost nil. Subsequently, the solution was adjusted to 15 ml by diluting it with ultrapure water. After adjusting the volume as described above, the element concentration in the electrolyte was measured by introducing it into the inductively coupled plasma emission spectrometer (ICPS-8100) by Shimadzu Corporation.

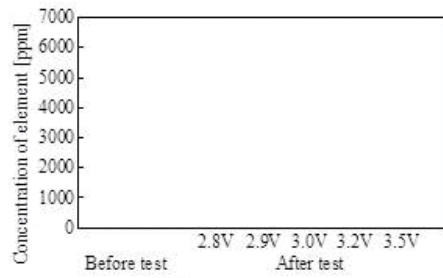
5.4 Element concentrations in electrolyte: measurement results

Figure 10 shows the element concentrations in the electrolyte taken from the EDLCs before and after the tests for each applied voltage. An analysis showed that the electrolyte contained boron, sodium, aluminum, silicon, potassium, calcium,

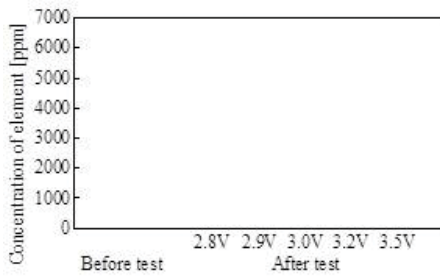




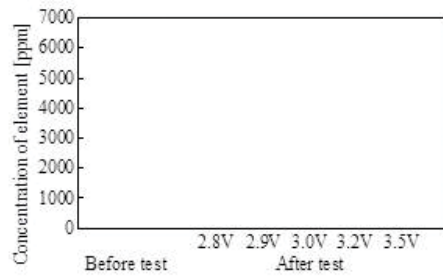
(i) Ti



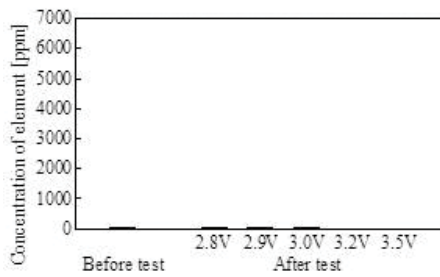
(j) V



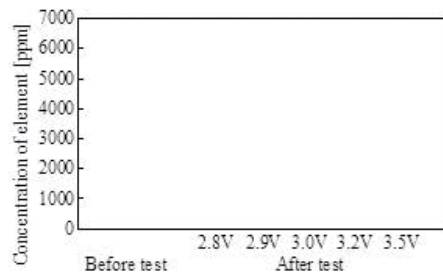
(k) Cr



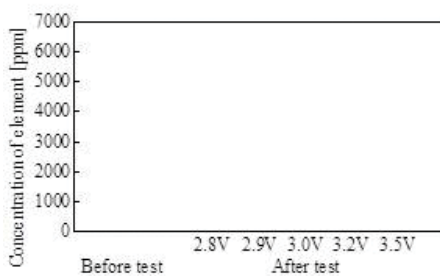
(l) Mn



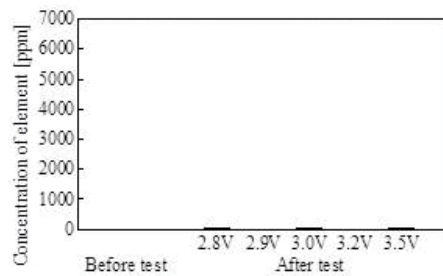
(m) Fe



(n) Ni



(o) Cu



(p) Zn

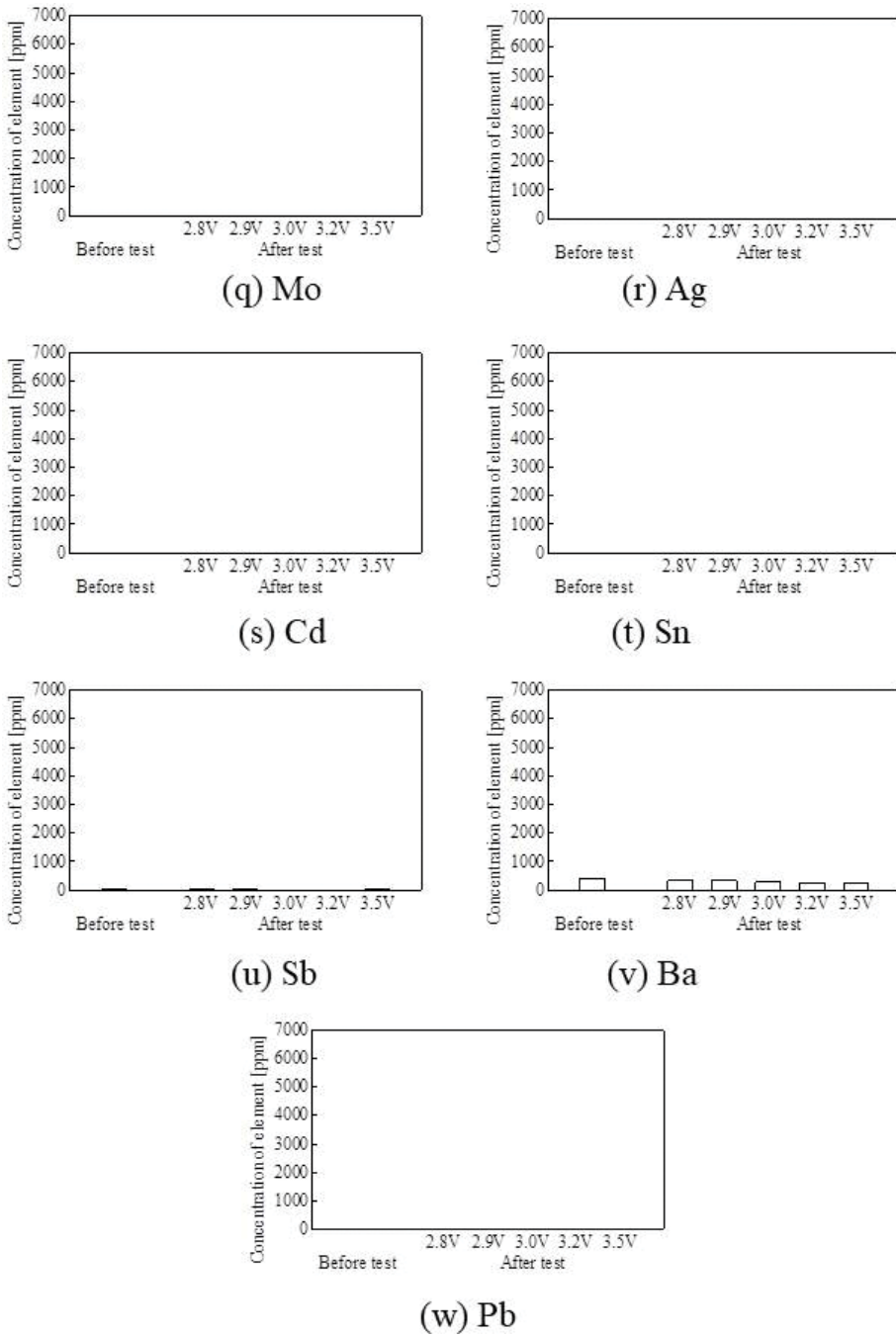


Figure 10. Element concentrations in electrolyte before and after test for each applied voltage.

and barium. The electrolyte commonly used for EDLCs is tetraethylammonium tetrafluoroborate $[(C_2H_5)_4NBF_4/C_4H_6O_3]$, which does not contain the elements above. However, activated carbon, which is the polarizable electrode material, is over 90% carbon, and part of carbon consists of oxygen and hydrogen compounds. Carbon also contains, as components characteristic to the raw material, sodium, silicon, potassium, calcium, iron, etc., as ash content. Therefore, it is possible that these dissolved into the electrolyte.

Furthermore, the possibility that these components are included as additives to improve the EDLC performance can also be considered. It is clear from the analytical results that whereas almost none of the dissolved element concentrations showed any variance between before and after the test at any holding voltage, only the silicon concentration decreased in relation to an increase in the holding voltage. A decreased concentration in the electrolyte signifies deposits onto the electrode surface. It is surmised that tetravalent silicon, similar to carbon (which is the main component of activated carbon), deposits onto the electrode surface and is a primary factor in the deterioration that increases the internal resistance of the EDLC.

6. Conclusion

For this chapter, we performed a voltage hold test, which is an accelerated deterioration test, on a commercial cylindrical electric double-layer capacitor (EDLC) by applying overvoltage. We confirmed behaviors of deterioration induced by the application of overvoltage. Furthermore, we disassembled the EDLCs after testing and conducted chemical analyses on the polarizable electrodes and the electrolyte, which are the main components of the EDLCs. This resulted in the three findings:

1. It was found that the internal resistance tended to increase with a rise in the holding voltage applied in the voltage hold test. On the other hand, the capacitance was not affected by the holding voltage and did not change significantly. This also revealed that some factors leading to an increase in internal resistance also increase with a rise in the holding voltage.
2. It was found for polarizable electrodes that as the holding voltage rises, the polarizable electrodes react at the solid-fluid interface with the fluorine in the electrolyte, and fluorine compounds are generated up to a depth of 10–13 nm from the electrode surface in the depth direction. It is surmised that this fluorine compound layer closes the micropores, reduces the surface area, reduces the EDLC capacitance, and is a deteriorating factor that increases the internal resistance.
3. It was found that as the holding voltage increases, the silicon concentration in the electrolyte decreases. It is believed that as the electrochemical reaction progresses, deposited silicon becomes a deteriorating factor and, by hampering the charge transfer, leads to an increase in the internal resistance of the EDLC.

Acknowledgements


The author thanks Mr. Mikio Taguchi and Dr. Hiromu Yoshitama, the graduate students from the Department of Electrical and Electronic Engineering at the Graduate School of Engineering of the University of Miyazaki, for their help with conducting this study.

Author details

Daisuke Tashima
Fukuoka Institute of Technology, Fukuoka, Japan

*Address all correspondence to: tashima@fit.ac.jp

IntechOpen

© 2018 The Author(s). Licensee IntechOpen. This chapter is distributed under the terms of the Creative Commons Attribution License (<http://creativecommons.org/licenses/by/3.0>), which permits unrestricted use, distribution, and reproduction in any medium, provided the original work is properly cited. 

References

- [1] Tokita M, Yoshimoto N, Fujii K, et al. Degradation characteristics of electric double-layer capacitors consisting of high surface area carbon electrodes with organic electrolyte solutions. *Electrochimica Acta*. 2016;**209**:210-218. DOI: 10.1016/j.electacta.2016.05.041
- [2] Weingarh D, Foelske-Schmitz A, Kötz R. Cycle versus voltage hold—Which is the better stability test for electrochemical double layer capacitors? *Journal of Power Sources*. 2013;**225**:84-88. DOI: 10.1016/j.jpowsour.2012.10.019
- [3] Bittner AM, Zhu M, Yang Y, et al. Ageing of electrochemical double layer capacitors. *Journal of Power Sources*. 2012;**203**:262-273. DOI: 10.1016/j.jpowsour.2011.10.083
- [4] Cericola D, Kötz R, Wokaun A. Effect of electrode mass ratio on aging of activated carbon based supercapacitors utilizing organic electrolytes. *Journal of Power Sources*. 2011;**196**:3114-3118. DOI: 10.1016/j.jpowsour.2010.11.157
- [5] Ruch PW, Cericola D, Foelske-Schmitz A, et al. Aging of electrochemical double layer capacitors with acetonitrile-based electrolyte at elevated voltages. *Electrochimica Acta*. 2010;**55**:4412-4420. DOI: 10.1016/j.electacta.2010.02.064
- [6] Ruch PW, Cericola D, Foelske A, et al. A comparison of the aging of electrochemical double layer capacitors with acetonitrile and propylene carbonate-based electrolytes at elevated voltages. *Electrochimica Acta*. 2010;**55**:2352-2357. DOI: 10.1016/j.electacta.2009.11.098
- [7] Zhu M, Weber CJ, Yang Y, et al. Chemical and electrochemical ageing of carbon materials used in supercapacitor electrodes. *Carbon*. 2008;**46**:1829-1840. DOI: 10.1016/j.carbon.2008.07.025
- [8] Dagousset L, Pognon G, Nguyen GTM, et al. Electrochemical characterisations and ageing of ionic liquid/ γ -butyrolactone mixtures as electrolytes for supercapacitor applications over a wide temperature range. *Journal of Power Sources*. 2017;**359**:242-249. DOI: 10.1016/j.jpowsour.2017.05.068
- [9] Zheng F, Li Y, Wang X. Study on effects of applied current and voltage on the ageing of supercapacitors. *Electrochimica Acta*. 2018;**276**:343-351. DOI: 10.1016/j.electacta.2018.04.153
- [10] Vališ D, Nováček O, Hasilová K, et al. Modelling of degradation and a soft failure moment during the operation of a supercapacitor applying selected diffusion processes. *Engineering Failure Analysis*. 2017;**82**:566-582. DOI: 10.1016/j.engfailanal.2017.04.019
- [11] Oz A, Gelman D, Goren E, et al. A novel approach for supercapacitors degradation characterization. *Journal of Power Sources*. 2017;**355**:74-82. DOI: 10.1016/j.jpowsour.2017.04.048
- [12] Huang Y, Zhao Y, Gong Q, et al. Experimental and correlative analyses of the ageing mechanism of activated carbon based supercapacitor. *Electrochimica Acta*. 2017;**228**:214-225. DOI: 10.1016/j.electacta.2017.01.059
- [13] Williard N, Baek D, Park JW, et al. A Life Model for Supercapacitors. *IEEE Transactions on Device and Materials Reliability*. 2015;**15**:519-528. DOI: 10.1109/TDMR.2015.2479466
- [14] Torregrossa D, Toghil KE, Amstutz V, et al. Macroscopic indicators of fault diagnosis and ageing in electrochemical double layer capacitors. *The Journal of Energy Storage*. 2015;**2**:8-24. DOI: 10.1016/j.est.2015.05.001

[15] Oukaour A, Pouliquen M, Tala-Ighil B, et al. Supercapacitors aging diagnosis using least square algorithm. *Microelectronics Reliability*. 2013;**53**:1638-1642. DOI: 10.1016/j.microrel.2013.07.032

[16] Ayadi M, Briat O, Eddahech A, et al. Thermal cycling impacts on supercapacitor performances during calendar ageing. *Microelectronics Reliability*. 2013;**53**:1628-1631. DOI: 10.1016/j.microrel.2013.07.079

[17] Kötzt R, Ruch PW, Cericola D. Aging and failure mode of electrochemical double layer capacitors during accelerated constant load tests. *Journal of Power Sources*. 2010;**195**:923-928. DOI: 10.1016/j.jpowsour.2009.08.045

[18] Bohlen O, Kowal J, Sauer DU. Ageing behaviour of electrochemical double layer capacitors: Part I. Experimental study and ageing model. *Journal of Power Sources*. 2007;**172**:468-475. DOI: 10.1016/j.jpowsour.2007.07.021

[19] Bohlen O, Kowal J, Dirk Uwe S. Ageing behaviour of electrochemical double layer capacitors: Part II. Lifetime simulation model for dynamic applications. *Journal of Power Sources*. 2007;**173**:626-632. DOI: 10.1016/j.jpowsour.2007.07.059

[20] Schiffer J, Linzen D, Sauer DU. Heat generation in double layer capacitors. *Journal of Power Sources*. 2006;**160**:765-772. DOI: 10.1016/j.jpowsour.2005.12.070

[21] Yoshitama H, Tashima D, Sakoda T, et al. Chemical analysis of casual elements for deterioration of cylindrical EDLC. *Electronics and Communications in Japan*. 2016;**99**:36-43. DOI: 10.1002/ecj.11911

Performance and Applications of Lithium Ion Capacitors

Xiaogang Sun, Wei Chen, Xu Li, Jie Wang, Hao Hu, Guodong Liang, Yapan Huang and Chengcheng Wei

Abstract

Lithium-ion capacitors (LICs) have a wide range of applications in the fields of hybrid electric vehicles (HEVs) and electric vehicles (EVs) for their both high energy density and high power density. Lithium-ion capacitors have become a potential alternative for next-generation chemical energy storage equipment owing to high energy density, high power density, and excellent cycle performance. The prelithiated multiwalled carbon nanotubes (MWCNTs) electrode was prepared by internal short circuit (ISC) and doping to intercalate lithium into MWCNTs. SLMP and lithium metal were used as lithium resources, respectively. The prelithiated carbon nanotubes were used as anode and activated carbon electrode as cathode. The capacitors were assembled in a glove box filled with argon. The prelithiated MWCNTs electrode eliminated irreversible capacity and improved substantially electrochemical performance of lithium-ion capacitors.

Keywords: prelithiation, stabilized lithium metal powder, graphite, multiwalled carbon nanotubes, activated carbon, lithium-ion capacitors

1. Introduction

The fossil energy's shortage and the use of fossil fuels cause environmental pollution and climate anomalies. The development and utilization of new energy sources, especially renewable energy, such as solar energy, wind energy, biomass, and hydrogen energy, have attracted increasing attention [1, 2]. And the development of new energy and energy storage equipment has become the focus of the investigation [3, 4]. Lithium-ion batteries (LIBs) and electrochemical capacitors (EC) are two important chemical energy storage devices. LIBs have high energy density but lower power density and cycle performance. EC has high power density and long cycle performance, but much lower energy density than the LIBs [5–8].

Lithium-ion capacitors, which combined the merits of lithium-ion batteries and electrochemical capacitors, are a new type of energy storage devices between the lithium-ion batteries and the electrochemical capacitors [9, 10]. In LICs, the anions adsorption and desorption in the electrolyte occurs on surface of positive electrode and simultaneously cations redox reaction occurred in the negative electrodes [11–15]. The ionic adsorption of electrical double layer and the faradaic electrochemical process (redox reaction) caused by lithium-ion intercalation and deintercalation contribute to high energy and powder density of lithium-ion capacitors than traditional capacitors [16–20].

In the carbon-based lithium-ion capacitors, the lithium ions are mainly derived from the electrolyte. But the solid-electrolyte interface (SEI) film formed during cycles will consume an amount of lithium ions which are irreversibly embedded in negative materials. That will bring down the capacity and cycle performance of LICs. So it is particularly important for the lithium predoping in negative electrode [21]. MWCNTs composed of unique one-dimensional systems with nanostructure have better stability, excellent conductivity, and lithium capacitance. It has become a popular research object for lithium-ion batteries [22]. SLMP applied to negative electrode can effectively prevent the problem of lithium ions deficiency and increase the capacity and rate performance of the LICs [23]. There is a potential difference between carbon electrode and lithium metal, which will promote the continuous flow of lithium ions into the carbon electrode when the carbon electrode and lithium metal are connected by short circuiting [9, 24, 25]. The final potential of the carbon anode will drop close to 0 V (vs. Li/Li+). Here, we introduce two new type LICs with different preintercalated lithium anodes.

It is generally known that graphite has a high theoretical Li intercalation capacity and widely was used as anode materials for lithium-ion capacitors because of natural abundance and relatively low cost [26–30]. However, lithium-ion intercalation tended to the same direction, and the dynamics of lithium-ion intercalation is slow. So it is difficult to perform charge/discharge work for lithium-ion capacitor at high current density with a poor rate performance [31, 32]. Compared to graphite, MWCNTs have higher stability. In this chapter, we report internal short circuit (ISC) approach was applied to high-performance LICs with activated carbon as cathode and prelithiated multiwalled carbon nanotubes/graphite composite as anode. Electrochemical performance of lithium-ion capacitors was investigated.

2. Fabrication and characterization of MWCNTs

MWCNTs were prepared by chemical vapor deposition (CVD), and benzene (Aladdin Co. Ltd., Shanghai) was used as carbon source, ferrocene (Aladdin Co. Ltd., Shanghai) as catalyst, and thiophene (Aladdin Co. Ltd., Shanghai) as accelerant. Ferrocene and thiophene were added into benzene and stirred uniformly; the flow rate was controlled by a micropump. Hydrogen and argon were used as carrier gas. The flow rate was controlled by a mass flow meter. The carbon source was fed into reactor with carrier gas. The MWCNTs were synthesized in a tube furnace with appropriate contents of ferrocene and thiophene and the ratio of benzene to

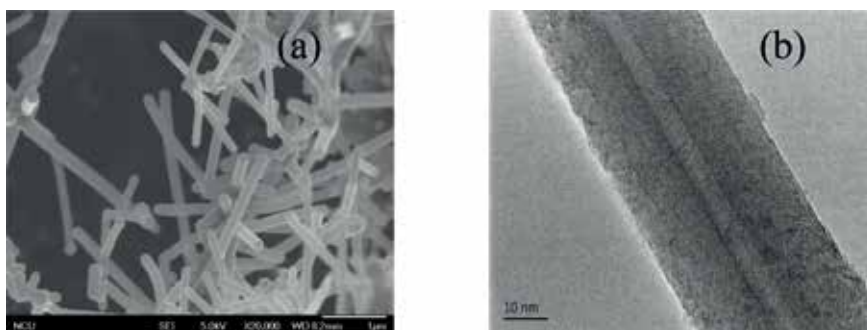


Figure 1. (a) FESEM and (b) HRTEM images of MWCNTs.

hydrogen in a certain temperature gradient. The obtained MWCNTs were further graphitized under the condition of vacuum at 2800°C for 24 h with the heating rate of 10°C/min. Finally, the graphitized MWCNTs were milled in a planetary ball mill at 200 r/min for 3 h [33].

Figure 1(a) showed FESEM image of MWCNTs. The MWCNTs presented linear and smooth structure. The diameters of the MWCNTs range from 100 to 120 nm with a large aspect ratio, and the MWCNTs have a small probability of bending around each other in space. Because of this particular microstructure makes the MWCNTs dispersed easily, simultaneously excellent conductivity and lithium-ions adsorption capacity, and other characteristics. **Figure 1(b)** showed HRTEM image of graphitized MWCNTs; the MWCNTs exhibited one-dimensional hollow structure, smooth wall, low defects, thin wall thickness, and regular and orderly arrangement of carbon atoms

3. SLMP/MWCNTs composite anode for lithium-ion capacitors

3.1 Experiment

3.1.1 Preparation of cathode electrode

The activated carbon (AC) was dispersed by sonication in N-methyl-2-pyrrolidone (NMP) for 2 h. The surfactant of polyvinylpyrrolidone (PVP, YueMei chemical Co. Ltd., Guangzhou) was added to improve the dispersion performance. The polyvinylidene fluoride (PVDF) was used as binder. The super carbon black (SP) was added to improve the conductivity. The activated carbon slurry was completed after a high-speed (FA25) cutting under 10,000 r/min for 1 h, and the mass ratio of AC:SP:PVDF was 85:5:10. The prepared slurry was coated on Al foil and dried at 60°C under vacuum, and cut into a disc of 14 mm diameter.

3.1.2 Preparation of anode electrode

The MWCNT powders were dispersed by sonication in N-methyl-2-pyrrolidone (NMP) for 2 h. The surfactant of polyvinylpyrrolidone was added to improve the dispersion performance. The polyvinylidene fluoride (PVDF) was used as binder. The slurry was completed after a high-speed (FA25) cutting under 10,000 r/min for 1 h. The mass ratio of MWCNTs:SP:PVDF was 8:1:1. The prepared slurry was coated on Cu foil and dried at 60°C under vacuum. A mixture of 0.5% polystyrene (PS) and 0.5% styrene butadiene rubber (SBR) was selected as a polymer binder, xylene as a solvent, and two groups were mixed to produce a binder solution. SLMP (FMC Corporation) was dispersed in the binder solution to obtain SLMP suspension with 0.5 wt%. Then the SLMP suspension was evenly coated on anode. After dried in vacuum, the SLMP coating is pressed between two glass plates for activating SLMP and then cut into a disc of 14 mm diameter.

3.1.3 Fabrication and characterization of lithium-ion capacitors

The two-electrode CR-2025 button lithium-ion capacitors were assembled with activated carbon as cathode and SLMP/MWCNT composites as anode in an argon-filled dry glove box. The electrolyte was 1 mol/L LiPF₆ in a mixed solvent system of EC/DMC (ethylene carbonate/diethyl carbonate) at a ratio of 1:1, and polypropylene microporous membrane was used as the separator.

The MWCNTs were characterized by field-emission scanning electron microscopy (FE-SEM, JSM-6701F), transmission electron microscopy (TEM, JEOL JEM-2010FEF), X-ray diffraction (XRD, DI SYSTEM), Raman spectrometer (SENTERRA), and thermogravimetry (TGA, PYRIS DIAMOND). The galvanostatic charge-discharge test of lithium-ion capacitors was performed after placed at room temperature for 24 h by a cell tester (CT-3008W-5V5mA-S4).

3.2 Results and discussion

3.2.1 The micromorphology of SLMP and AC

Figure 2(a) showed the micromorphology of SLMP. The diameters of the SLMP range from 30 μm , and outside coated with a thin layer of Li_2CO_3 protective coating, which can exist in a relatively low air humidity environment. **Figure 2(b)** showed the micromorphology of AC; it was observed that AC particles show irregular morphology and the average size of the particles is about 4 μm .

3.2.2 XRD and Raman spectroscopy analysis of MWCNTs

Figure 3(a) showed the X-ray diffraction (XRD) pattern of MWCNTs. The main diffraction peaks of MWCNTs were both at $2\theta = 26^\circ$, which coincide with the (002) planes. The main diffraction peak of MWCNTs is sharp and narrow, which indicates that the MWCNTs have a more regular and orderly arrangement of carbon atoms. Moreover, MWCNTs have a higher degree of crystallinity and conductivity. The

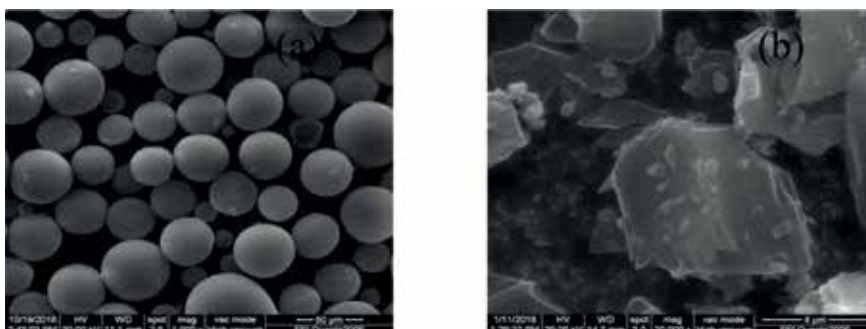


Figure 2. Micromorphology of (a) SLMP and (b) AC.

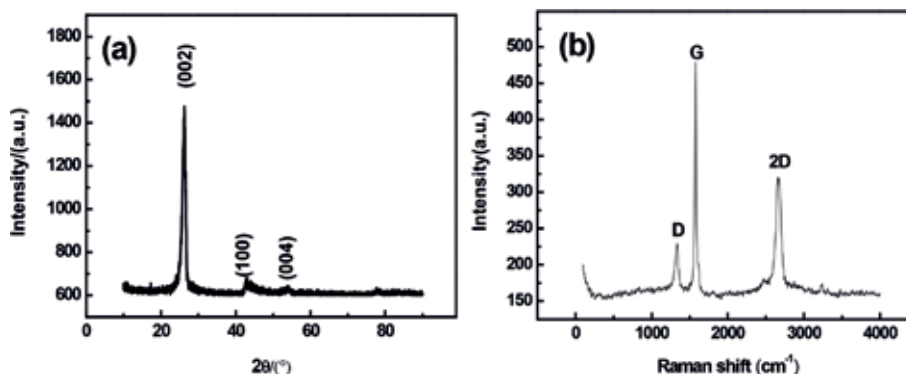


Figure 3. XRD (a) and Raman spectroscopy (b) of MWCNTs.

(100) and (004) diffraction peaks are the catalyst components in the preparation of MWCNTs. **Figure 3(b)** showed the Raman spectroscopy of MWCNTs. There exhibited two distinct peaks corresponding to about 1351 cm⁻¹D band and about 1585 cm⁻¹G band, respectively. The MWCNTs have higher and sharper G peaks, which indicate that the degree of crystallinity and structure integrity of MWCNTs are great. In addition, the 2D peak appears at 2752 cm⁻¹, which indicates that the MWCNTs have higher degree of crystallinity.

3.2.3 TG of the MWCNTs

Figure 4 showed the TG curves of MWCNTs. The TG test was performed under air atmosphere with the heating rate of 5°C/min to 1000°C. The TG curves of MWCNTs were divided into two stages. In the first stage, the weight loss of 0.11% is caused by the oxidation of a small amount of amorphous carbon during the synthesis of MWCNTs. The weight loss of the second stage is caused by the ablation of impurities in the MWCNTs. The initial reaction temperature of MWCNTs was 585°C, which indicates that the antioxidant capacity and thermal stability of MWCNTs were great. Meanwhile, the residual amounts of MWCNTs were 0.2%, which confirm that the purity of these MWCNTs is great.

3.2.4 Galvanostatic charge and discharge

Figure 5(a) and **(b)** showed the galvanostatic charge-discharge curves of none-lithiated and prelithiated LICs at different current densities, respectively. The tests were performed using two-electrode system at voltage profile of 2–4 V. The energy density of LICs can be calculated by $E_{sp} = (C_{sp} * V^2) / 2$ (C_{sp} represents the specific capacitance and V represents the discharge potential excluding IR drop). The power density of LICs can be calculated by $P_{sp} = E_{sp} / t$ (t represents the discharge time), and the specific capacitance C_{sp} can be calculated by the formula $C = (2I * t) / (m * \Delta V)$ (I represents the discharge current, m is the active material mass of a single pole, ΔV is the potential of discharge, and t is the discharge time). The charge-discharge curves of prelithiated LICs showed a good linear relationship and exhibited a shape of isosceles triangle. On the contrary, the charge-discharge curves of nonlithiated LICs presented a distorted shape, and the internal resistance obviously increases with the improving current density and the discharge time is obviously shortened, which related a poor

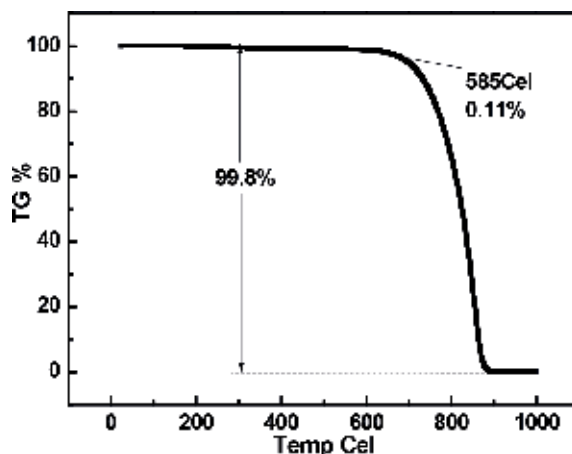


Figure 4.
TG curve of MWCNTs.

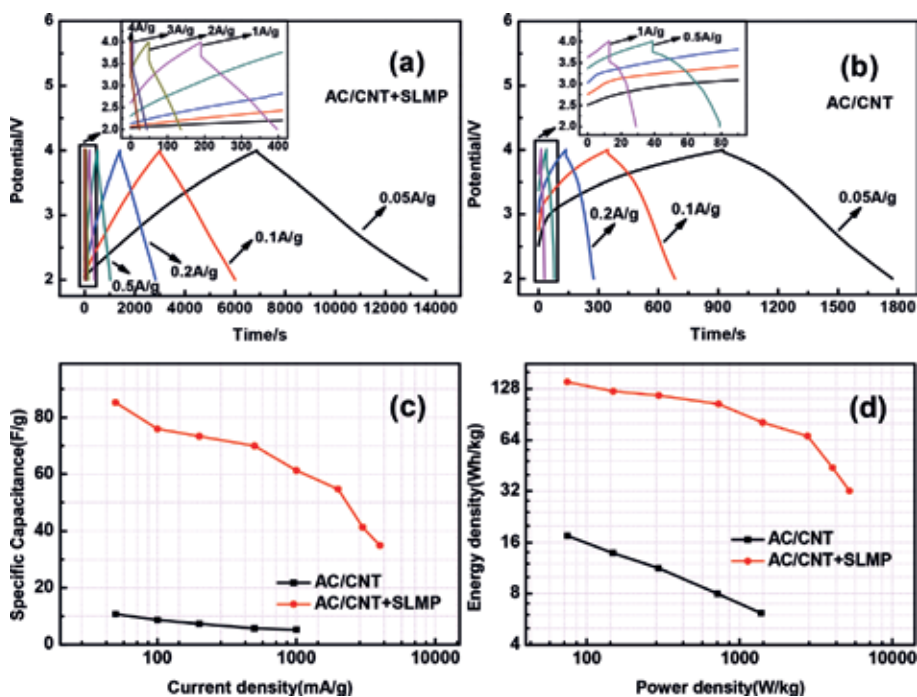


Figure 5. Galvanostatic charge/discharge curves of LICs with nonlithiated (a) and prelithiated (b) specific capacitance with different current density (c) and the ragone plots (d) for the LICs.

power density. Generally, the power density of lithium-ion capacitors is determined by the negative materials; when the negative electrode consists of nonlithiated MWCNTs, the rate of intercalation and deintercalation of lithium ions is slow, resulting in a poor power density. The intercalation and deintercalation rate of lithium ions will be accelerated with the addition of SLMP. **Figure 5(c)** showed the discharging specific capacity at different rates. The prelithiated LICs showed higher discharging specific capacity and rate performance than those of nonlithiated LICs. The nonlithiated and prelithiated LICs exhibited discharging specific capacity of 10.74 and 85.18 F/g at current density of 0.1 A/g. **Figure 5(d)** showed the ragone plots of LICs. Prelithiated LICs presented the best electrochemical performance. The maximal energy density and power density of prelithiated LICs reached 140.4 Wh/kg and 5.25 W/kg in the range of current density from 0.05 to 4 A/g [34, 35].

Figure 6(a) showed the charge and discharge cycle performance of LICs with nonlithiated and prelithiated. The 3000 cycles test was performed in the range of 2~4 V at the current density of 0.4 A/g. After 3000 cycles of constant current charge and discharge, the cycling performance of LICs with nonlithiated drops significantly. In contrast, **Figure 6(b)** showed the discharge cycle performance of LICs with prelithiated after 3000 cycles. The capacitance retention still holds 82%, the charge and discharge curves without twist and distortion, which still maintained a good isosceles triangle shape and shows good cycle performance.

3.3 Conclusions

In the chapter, lithium-ion capacitors have been assembled with SLMP/MWCNTs composite as anode and activated carbon as cathode, respectively. The results showed that prelithiated LICs exhibit excellent electrochemical performance. The addition of SLMP to anode can increase the electrochemical

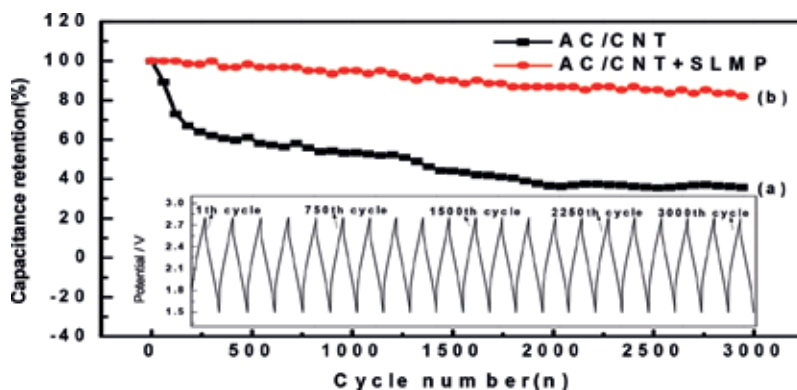


Figure 6.
Charge and discharge cycle performance of LICs with nonlithiated (a) and prelithiated (b).

performance of the LICs and eliminate irreversible capacity. Especially, the prelithiated LICs exhibited optimal electrochemical performance, with a specific capacity of 85.18 F/g at current density of 0.1 A/g, and the maximal energy and power density reached 140.4 Wh/kg and 5.25 W/kg in the range of current density from 0.05 to 4 A/g, respectively. After 3000 charge-discharge cycles, the prelithiated LICs maintained about 82% capacity retention rate. Therefore, the prelithiated LICs with a SLMP addition in the anode have a potential application for energy storage device.

4. Lithium-ion capacitors using prelithiated MWCNTs/graphite composite as anode

4.1 Experiment

4.1.1 The preparation of anode and prelithiation procedure

The slurry of composite active material (MWCNTs/graphite) was prepared by ultrasonically dispersing and high-speed shearing with super carbon black (SP) as conductive agent, polyvinylidene difluoride (PVDF) as binder, and NMP as solvent, with the ratio of 8:1:1. The slurry was coated on the copper foil. Then, the anode was dried at 60°C under vacuum for 12 h. The MWCNTs content in composite active material was 0, 25, 50, 75, 100 wt%, respectively. The prelithiation was accomplished through direct physical contact between as-prepared MWCNTs/graphite electrode and lithium metal with electrolyte in pressure; the degree of prelithiation was controlled by contact time.

4.1.2 The preparation of cathode

The ratio of AC:SP:PVDF is 8:1:1, subsequently followed by ultrasonically dispersing, high-speed shearing, and coating on aluminum foil. Then, the cathode was dried at 60°C under vacuum for 12 h and was cut into a disc of 14 mm diameter.

4.1.3 The fabrication of MWCNTs/Li half-cells and lithium-ion capacitors

The tailored MWCNTs/graphite anodes were used as working electrodes. Lithium foil was used as the counterelectrode and Celgard 2300 was used as the separator. The solution of 1.0 M LiPF₆ in EC:DMC (1:1, vol.) was utilized as the electrolyte. Based

on the content of MWCNTs, the half-cells were signed as CNT0, CNT25, CNT50, CNT75, and CNT100, respectively. The two-electrode LICs were assembled with AC cathode and MWCNTs anode, and the corresponding LICs were recorded as LIC0, LIC25, LIC50, LIC75, LIC100. All cells were assembled in an argon-filled glove box.

4.1.4 Characterizations

The SEM of anode and that of cathode were characterized by FE-SEM (JSM-6701F). The electrochemical characterization of the LICs was performed by a cell tester (CT-3008W-5V5mA-S4). The specific capacitance was calculated based on total mass of the MWCNTs, graphite, AC, and SP.

4.2 Results and discussion

4.2.1 The SEM of anode and cathodes

Figure 7(a) shows the SEM image of AC anode, which shows irregular structure and occupies the vast majority of space. Meanwhile, SP uniformly dispersed between gaps of AC particles can provide good conductivity. **Figure 7(b)** shows the SEM image of graphite cathode, and **Figure 7(c)** shows the SEM image of MWCNTs/graphite composite cathode; comparison shows that MWCNTs and graphite are well connected and present a web-like network structure and three-dimensional conduction system. This structure was applied to the negative electrode to shorten the diffusion path of lithium ions and improve the kinetics of lithium-ion intercalation.

4.2.2 Galvanostatic charge and discharge

Figure 8(a) shows the first charge and discharge curves of raw MWCNTs and graphite half-cells at 1C rate; for graphite half-cells, the voltage plateau of SEI film formation is at about 0.7 V [36]. In comparison, for MWCNT half-cells, the

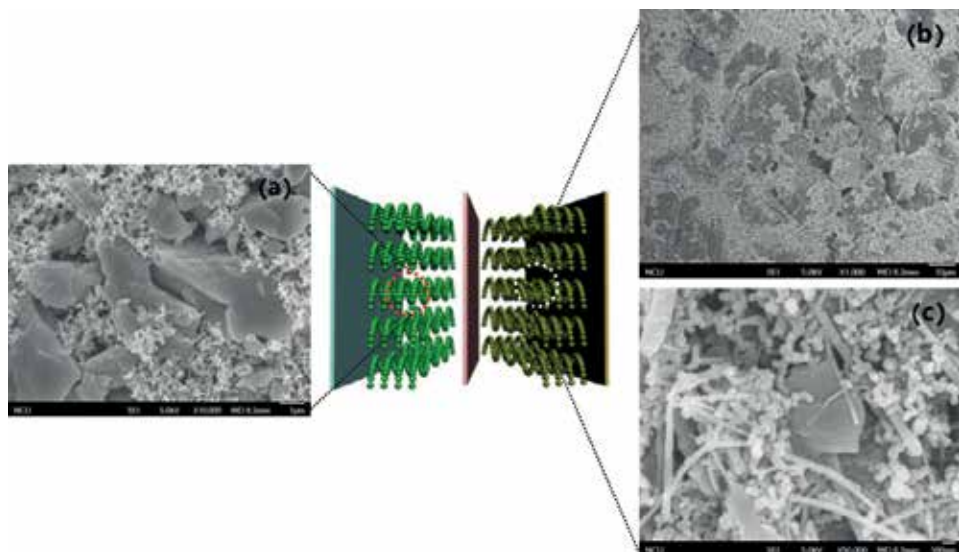


Figure 7. Illustration of lithium-ion capacitors and corresponding SEM images of the electrode materials. (a) SEM image of AC anode, (b) SEM image of graphite cathode, (c) SEM image of MWCNTs/graphite composite cathode.

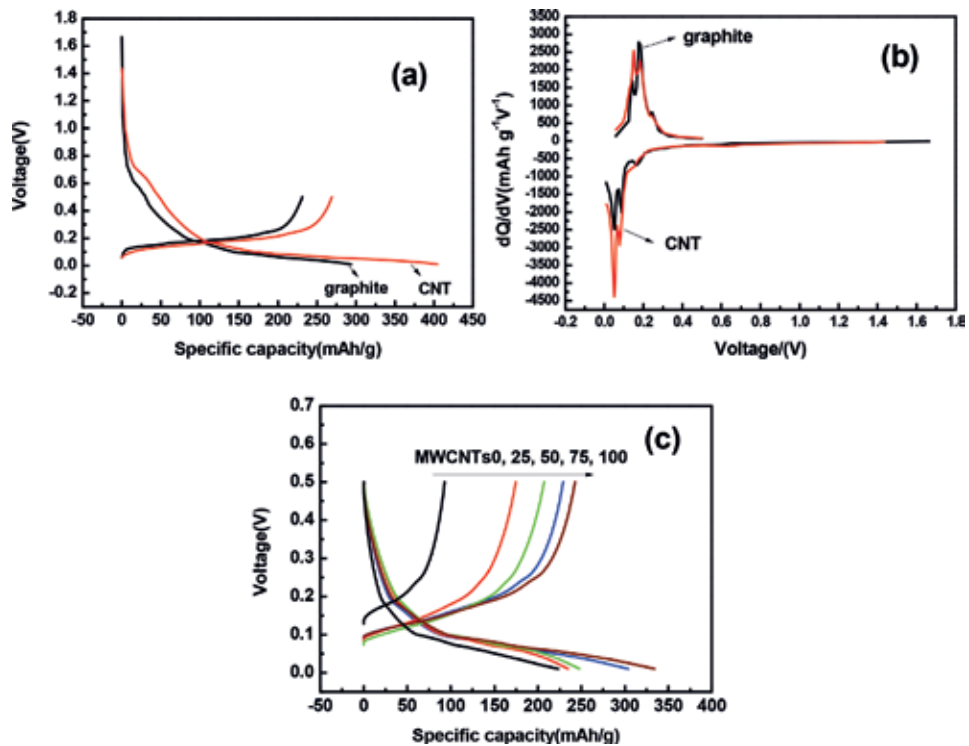


Figure 8. The first charge-discharge curves of MWCNTs and graphite electrodes before being predoping (a), the differential capacity versus voltage (dQ/dV) curves of the MWCNTs/Li and graphite/Li coin cells (b) and the first charge curves of MWCNTs/graphite electrodes with different content of MWCNT at a prelithiation time of 60 min (c).

voltage plateau of SEI film formation is at about 0.7 V too. Meanwhile, MWCNTs have a higher irreversible capacity and first discharge capacity than graphite. **Figure 8(b)** shows the differential capacity versus voltage (dQ/dV) curves of MWCNTs and graphite half-cells. Three stages of lithium-ion intercalation voltage were local on 0.16, 0.08, and 0.055 V, respectively. **Figure 8(c)** shows the first delithiation (charge) capacity of CNT0, CNT25, CNT50, CNT75, and CNT100 at 60 min prelithiation time. In the same prelithiation time, the open-circuit voltage (OCV) of pure graphite half-cell was significantly superior to other half-cells. The delithiation capacity increases with the gradual increase of MWCNTs, which indicates the kinetics of intercalation of MWCNTs is higher than pure graphite.

Figure 9(a–e) showed the galvanostatic charge-discharge curves of LIC0, LIC25, LIC50, LIC75, and LIC100 at different current densities, respectively. The tests were performed using two-electrode system at voltage profile of 2–4 V. The energy density of LICs can be calculated by $E_{sp} = (C_{sp} \cdot V^2) / 2$ (C_{sp} represents the specific capacitance and V represents the discharge potential excluding IR drop). The power density of LICs can be calculated by $P_{sp} = E_{sp} / t$ (t represents the discharge time), and the specific capacitance C_{sp} can be calculated by the formula $C = (2I \cdot t) / (m \cdot \Delta V)$ (I represents the discharge current, m is the active material mass of a single pole, ΔV is the potential of discharge, and t is the discharge time). The charge-discharge curves of LIC25 showed a good linear relationship and exhibited a shape of isosceles triangle. The LIC25 had the longest discharge time than other LICs and showed good capacitance characteristics. Meanwhile, the charge-discharge curves of LIC75 also showed a good linear relationship and

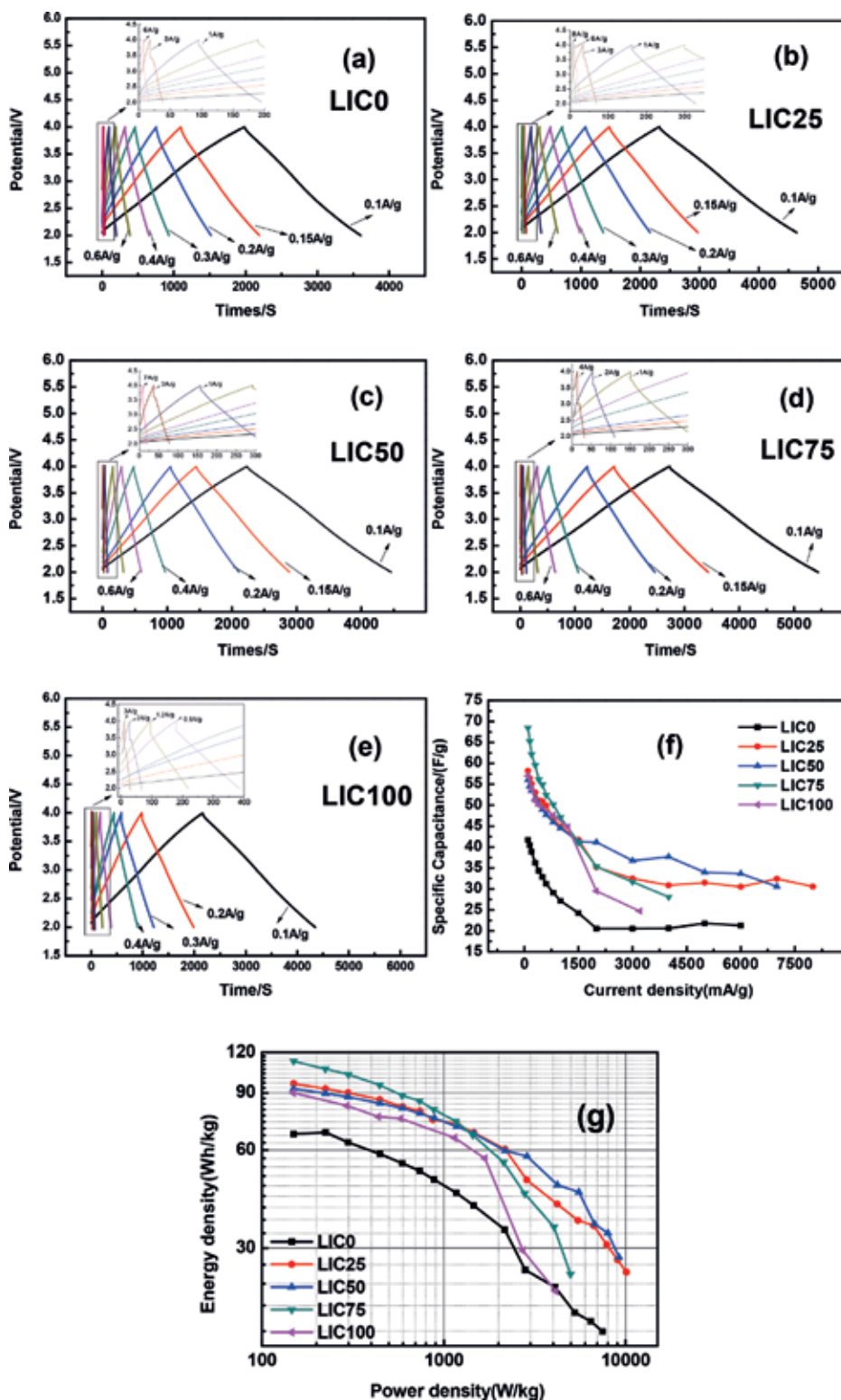


Figure 9. Galvanostatic charge-discharge curves of lithium-ion capacitors with different content of WCNT at a different current density, (a) LIC0, (b) LIC25, (c) LIC50, (d) LIC75, (e) LIC100, and specific capacitance with different current density (f), the ragone plots for the LICs (g).

exhibited high power performance. On the contrary, the charge-discharge curves of LIC0 and LIC100 presented a distorted shape, and the internal resistance obviously increases with the improving current density and the discharge time is obviously shortened, which related a poor power density. Generally, the power density of LICs is determined by the negative materials; when the negative electrode consists of pure graphite, the rate of intercalation and deintercalation of lithium ions is slow, resulting in a poor power density. The intercalation and deintercalation rate of lithium ions will be accelerated with the addition of MWCNTs. However, excessive amounts of carbon nanotubes will consume large amounts of lithium ions, and the formation of thick solid electrolyte interface (SEI) film will greatly impede the migration of lithium ions. That is, the appropriate MWCNTs content to improve the power density is of crucial importance.

Figure 9(f) showed the specific capacitance of LICs at various current densities. The LIC25 showed higher discharging specific capacitance and rate performance than other LICs. **Figure 9(g)** showed the ragone plots of LICs. LIC25 presented the best electrochemical performance. The maximal energy density and power density of LIC25 reached 96 Wh/kg and 10.1 kW/kg in the range of current density from 0.1 to 8 A/g.

Figure 10 showed the charge and discharge cycle performance of LIC0 and LIC25. The 3000 cycles test was performed in the range of 2.2~3.8 V at the current density of 0.8 A/g. After 5000 cycles of constant current charge and discharge, the cycling performance of LIC0 drops significantly, which is related to the cracking and pulverization of graphite materials, lithium, and organic solvents common into the graphite layer, and then influences the performance of cycle. As opposed to LIC0, the capacitance retention of LIC25 still holds 86%, the charge and discharge curves without twist and distortion, which still maintained a good isosceles triangle shape and shows good cycle performance.

4.3 Conclusions

In the chapter, lithium-ion capacitors have been assembled with prelithiated MWCNTs/graphite composite as anode and activated carbon as cathode. The results showed that LICs with prelithiated exhibit excellent electrochemical performance. Especially, the LIC25 exhibited optimal electrochemical performance, with a specific capacitance of 58.2 F/g at current density of 0.1 A/g, and the maximal energy and power density reached 96 Wh/kg and 10.1 kW/kg in the range of current

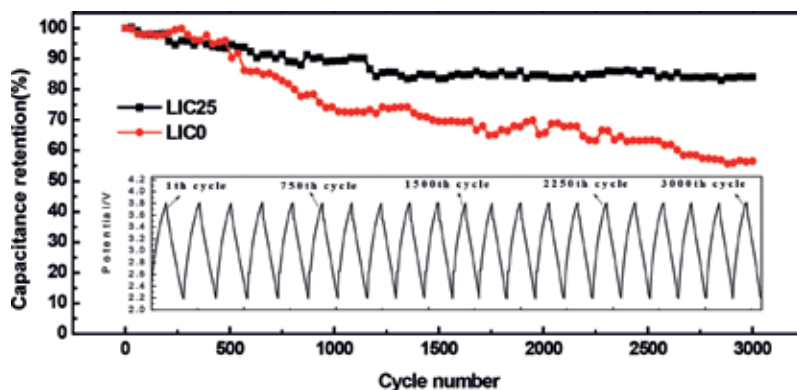


Figure 10. Long-term cycle performance for the LIC in the voltage range of 2.2~3.8 V at 800 mA/g current density.

density from 0.1 to 8 A/g, respectively. After 3000 charge-discharge cycles, the LIC25 maintained about 86% capacity retention rate. Therefore, the LICs with the prelithiated MWCNTs/graphite composite materials have a potential application for energy storage device.

Author details

Xiaogang Sun*, Wei Chen, Xu Li, Jie Wang, Hao Hu, Guodong Liang, Yapan Huang and Chengcheng Wei
College of Mechantronics Engineering, Nanchang University, Nanchang, China

*Address all correspondence to: xiaogangsun@163.com

IntechOpen

© 2018 The Author(s). Licensee IntechOpen. This chapter is distributed under the terms of the Creative Commons Attribution License (<http://creativecommons.org/licenses/by/3.0>), which permits unrestricted use, distribution, and reproduction in any medium, provided the original work is properly cited. 

References

- [1] Miller JR, Simon P. Electrochemical capacitors for energy management. *Science Magazine*. 2008;**321**(5889):651-652
- [2] Kang YJ, Kim B, Chung H, et al. Fabrication and characterization of flexible and high capacitance supercapacitors based on MnO₂/CNT/papers. *Synthetic Metals*. 2010;**160**(23):2510-2514
- [3] Liu M, Zhang L, Han P, et al. Controllable formation of niobium nitride/nitrogen-doped graphene nanocomposites as anode materials for lithium-ion capacitors. *Particle & Particle Systems Characterization*. 2016;**32**(11):1006-1011
- [4] Wang H, Zhang Y, Ang H, et al. A high-energy lithium-ion capacitor by integration of a 3D interconnected titanium carbide nanoparticle chain anode with a pyridine-derived porous nitrogen-doped carbon cathode. *Advanced Functional Materials*. 2016;**26**(18):3082-3093
- [5] Hosseinzadeh E, Genieser R, Worwood D, et al. A systematic approach for electrochemical-thermal modelling of a large format lithium-ion battery for electric vehicle application. *Journal of Power Sources*. 2018;**382**:77-94
- [6] Hao ZQ, Cao JP, Wu Y, et al. Preparation of porous carbon sphere from waste sugar solution for electric double-layer capacitor. *Journal of Power Sources*. 2017;**361**:249-258
- [7] Ren JJ, Su LW, Qin X, et al. Pre-lithiated graphene nanosheets as negative electrode materials for Li-ion capacitors with high power and energy density. *Journal of Power Sources*. 2014;**264**(264):108-113
- [8] Fan K, Tian Y, Zhang X, et al. Application of stabilized lithium metal powder and hard carbon in anode of lithium-sulfur battery. *Journal of Electroanalytical Chemistry*. 2016;**760**:80-84
- [9] Du H, Yang H, Huang C, et al. Graphdiyne applied for lithium-ion capacitors displaying high power and energy densities. *Nano Energy*. 2016;**22**:615-622
- [10] Sun X, Zhang X, Liu W, et al. Electrochemical performances and capacity fading behaviors of activated carbon/hard carbon lithium ion capacitor. *Electrochimica Acta*. 2017;**235**:158-166
- [11] Amatucci GG, Badway F, Pasquier AD, et al. An asymmetric hybrid nonaqueous energy storage cell. *Journal of the Electrochemical Society*. 2001;**148**(8):A930-A939
- [12] Pasquier AD, Plitz I, Menocal S, et al. A comparative study of Li-ion battery, supercapacitor and nonaqueous asymmetric hybrid devices for automotive applications. *Journal of Power Sources*. 2003;**115**(1):171-178
- [13] Dahn JR, Steel JA. Energy and capacity projections for practical dual-graphite cells. *Journal of the Electrochemical Society*. 2000;**147**(3):899-901
- [14] Yoshino A, Tsubata T, Shimoyamada M, et al. Development of a lithium-type advanced energy storage device. *Journal of the Electrochemical Society*. 2004;**151**(12):A2180-A2182
- [15] Sang-Wook W, Dokko K, Nakano H, et al. Bimodal porous carbon as a negative electrode material for lithium-ion capacitors. *Electrochemistry*. 2007;**75**(8):635-640
- [16] Lee SW, Yabuuchi N, Gallant BM, et al. High-power lithium batteries

- from functionalized carbon-nanotube electrodes. *Nature Nanotechnology*. 2010;5(7):531-537
- [17] Jin Z, Liu X, Jing W, et al. Different types of pre-lithiated hard carbon as negative electrode material for lithium-ion capacitors. *Electrochimica Acta*. 2016;187:134-142
- [18] Zhang P, Ma J, Mani S, et al. High Performance Anode Material for Lithium-Ion Battery: US, US7722991. 2010
- [19] Byeon A, Glushenkov AM, Anasori B, et al. Lithium-ion capacitors with 2D Nb₂CT_x, (MXene)—Carbon nanotube electrodes. *Journal of Power Sources*. 2016;326:686-694
- [20] Hsieh CL, Tsai DS, Chiang WW, et al. A composite electrode of tin dioxide and carbon nanotubes and its role as negative electrode in lithium ion hybrid capacitor. *Electrochimica Acta*. 2016;209:332-340
- [21] Tropy NL, Cao W, Zheng JP. Comparison Study of Various Anode Materials for Li-Ion Capacitors[C]// Meeting Abstracts. The Electrochemical Society. 2014;(2):227-227
- [22] Jayasinghe R, Thapa AK, Dharmasena RR, et al. Optimization of multi-walled carbon nanotube based CF_x, electrodes for improved primary and secondary battery performances. *Journal of Power Sources*. 2014;253(5):404-411
- [23] Howe JY, Boatner LA, Kolopus JA, et al. Vacuum-tight sample transfer stage for a scanning electron microscopic study of stabilized lithium metal particles. *Journal of Materials Science*. 2012;47(3):1572-1577
- [24] Kim M, Xu F, Jin HL, et al. A fast and efficient pre-doping approach to high energy density lithium-ion hybrid capacitors. *Journal of Materials Chemistry A*. 2014;2(26):10029-10033
- [25] Park H, Kim M, Xu F, et al. In situ synchrotron wide-angle X-ray scattering study on rapid lithiation of graphite anode via direct contact method for Li-ion capacitors. *Journal of Power Sources*. 2015;283:68-73
- [26] Aurbach D, Levi MD, Elena Levi A, et al. Failure and stabilization mechanisms of graphite electrodes. *Journal of Physical Chemistry B*. 1997;101(12):2195-2206
- [27] Ng SH, Vix-Guterl C, Bernardo P, et al. Correlations between surface properties of graphite and the first cycle specific charge loss in lithium-ion batteries. *Carbon*. 2009;47(3):705-712
- [28] Spahr ME, Buqa H, Würsig A, et al. Surface reactivity of graphite materials and their surface passivation during the first electrochemical lithium insertion. *Journal of Power Sources*. 2006;153(2):300-311
- [29] Gao X, Zhan C, Yu X, et al. A high performance lithium-ion capacitor with both electrodes prepared from Sri Lanka graphite ore. *Materials*. 2017;10(4):414
- [30] Barcellona S, Ciccarelli F, Iannuzzi D, et al. Overview of lithium-ion capacitor applications based on experimental performances. *Electric Machines & Power Systems*. 2016;44(11):1248-1260
- [31] Khomenko V, Raymundo-Piñero E, Béguin F. High-energy density graphite/AC capacitor in organic electrolyte. *Journal of Power Sources*. 2008;177(2):643-651
- [32] Sivakkumar SR, Nerkar JY, Pandolfo AG. Rate capability of graphite materials as negative electrodes in lithium-ion

capacitors. *Electrochimica Acta*.
2010;55(9):3330-3335

[33] Sun XG, Qiu ZW, Chen L, et al.
Industrial synthesis of whisker carbon
nanotubes. *Materials Science Forum*.
2016;852:514-519

[34] Zhang J, Shi Z, Wang J, et al.
Composite of mesocarbon microbeads/
hard carbon as anode material for
lithium ion capacitor with high
electrochemical performance. *Journal
of Electroanalytical Chemistry*.
2015;747:20-28

[35] Zhang J, Shi Z, Wang C. Effect
of pre-lithiation degrees of
mesocarbon microbeads anode on
the electrochemical performance of
lithium-ion capacitors. *Electrochimica
Acta*. 2014;125(12):22-28

[36] Ai G, Wang Z, Zhao H, et al.
Scalable process for application of
stabilized lithium metal powder in
Li-ion batteries. *Journal of Power
Sources*. 2016;309:33-41

Transition Metal Oxide-Based Nano-materials for Energy Storage Application

Apurba Ray, Atanu Roy, Samik Saha and Sachindranath Das

Abstract

With improvement of global economy, the fatigue of energy becomes inevitable in twenty-first century. It is expected that the increase of world energy requirements will be triple at the end of this century. Thus, there is an imperative need for development of renewable energy sources and storage systems. Among various energy storage systems, supercapacitors are ascertained one of the most significant storage devices. But the development of supercapacitor devices with high power and energy density are the greatest challenges for modern research. In this article, transition metal oxides such as $\text{TiO}_2\text{-V}_2\text{O}_5$, NiMn_2O_4 etc. with porous structure are considered as high performance supercapacitors electrode. The effects of its structural, morphological and electrochemical properties have been studied extensively. A $\text{TiO}_2\text{-V}_2\text{O}_5$ and NiMn_2O_4 based electrode delivered specific capacitance of 310 and 875 F g^{-1} , respectively at a scan rate 2 mV s^{-1} . This $\text{TiO}_2\text{-V}_2\text{O}_5$ based asymmetric supercapacitor also exhibits excellent device performance with specific energy $20.18 \text{ W h kg}^{-1}$ at specific power 5.94 kW kg^{-1} , and retained 88.0% specific capacitance at current density of 10 A g^{-1} after 5000 cycles.

Keywords: supercapacitor, transition metal oxides, nanostructure, energy density, power density

1. Introduction

Rapidly depleting level of fuel reservoir along with the increasing effect of environmental pollution are the two most important concerns of twenty-first century. The rate at which the fossil fuel is being consumed today, it will take around 40 more years to run all the known oil deposits dry leaving the whole world into complete darkness. Fossil fuel is a very rich form of energy containing around 30–50 MJ of energy per kilogram. Combustion of fossil fuels results in the emission of CO_2 , CH_4 , N_2O etc. in the atmosphere which trap the solar radiation in the atmosphere [1, 2]. Although the natural trapping of solar radiation is vital for all the lives on the earth but due to excessive emissions of these gases the earth is getting hotter. According to the study conducted by NASA's Goddard institute, the Earth's average temperature has risen by 0.8°C since the beginning of the industrial revolution. Although this increment may seem very small but the alarming fact is that a little

more increase in the global temperature will cause the polar ice caps and glaciers to melt, causing the sea level to rise flooding the coastal lines [3]. In order to sustain human growth these issues have to address as soon as possible. To reduce the world's hunger for fossil fuels while maintaining the same life standards we have to focus on the alternative green energy sources like solar, wind, tidal etc. Although these sources have the ability to meet the world's energy requirements but the intermittent nature of these energy sources is an unavoidable problem which significantly stimulates the motivation of research on the energy storage systems. Today a variety of energy storage and conversion devices are available such as batteries, conventional capacitors, fuel cell and supercapacitors etc. But among such energy storage systems electrochemical capacitors or supercapacitors have drawn attention as one of the most promising energy storage systems because of their high power density, short charging time and long life span although having moderate energy density 10–15 mWh/g which is still very less compared to batteries. Different research groups in the world are trying to improve the energy density and overall life span of the device by suitably choosing different electrode materials [4–8].

2. Brief history of supercapacitor

Electrical charge storage by a surface was first discovered from the phenomena of rubbing amber with fur which attracts dust in ancient age. Invention of the Leiden jar in 1757 is the first developed technology for capacitor. This Leiden jar was further improved to flat capacitor by Benjamin Franklin. This resulted in the reduction of volume as well as increase in reliability and convenience. In the late nineteenth century Helmholtz solved the electrical charge storage by a capacitor by using Faraday's law. He proved the existence of two parallel sheets of opposite charges on the surface of metal and the solution side. He proposed the model of charge/ion distribution near metal surface. It is the foundation stone for the development of fundamental aspects of capacitive technology as well as the quantitative science which describe the nature of electrostatic behavior. In the General Electric Laboratories (1957), they have developed a capacitor by using two porous carbon electrodes and aqueous electrolyte. Later it is known as electrochemical double layer capacitor. They got the U.S. Patent for this (US Patent 2,800,616). Almost a decade later (1966), Standard Oil of Ohio's (SOHIO) scientists and engineers have developed the modern electrochemical supercapacitor (SC) capacitor using porous carbon and non-aqueous electrolyte [9–12]. The non-aqueous electrolyte enables to have wide potential window for SC, which results in the increase in storage capacity. SOHIO sold this technology to Nippon Electric Company (NCE, Japan) and they used it commercially for the first time as the backup power for computer memory and also named as the supercapacitor. Presently, NEC/TOKIN, ELNA, Maxwell Technologies, Panasonic and several other companies invest in the development of supercapacitors. In 2004, the worldwide market of supercapacitor was 100 million US dollars, while the worldwide sales of supercapacitor reached to 400 million US dollars by the end of 2010. It was estimated that the market of supercapacitor will rise to 2 billion US dollars by 2020 [13–15].

3. Different types of supercapacitor

The importance of supercapacitor as an energy storage was significantly increased in the last decade of twentieth century and it witnessed significant advances in the field. Several works by Conway et al. and others [United States Pat., 1996] have investigated and identified the underlying chemistry and developed the

model for charge storage. Due to the charge storage mechanism, supercapacitors are categorized into two different types, electrochemical double layer capacitors (EDLCs, non-Faradic electrostatic storage) and pseudocapacitors (Faradic, redox reaction based capacitors). In addition, there is another class of supercapacitors known as hybrid supercapacitors which is the combination of both storage mechanisms. In this chapter, the storage mechanism, electrode materials, electrolytes of different supercapacitors will be discussed.

3.1 Electrochemical double layer capacitor (EDLC)

EDLCs have a similar structure to that of conventional capacitors except the dielectric is being replaced by electrolyte. Two highly porous carbon electrodes are separated by a porous separator and electrolyte. The energy storage mechanism of EDLC relies on the non-Faradic process i.e. electrostatic adsorption ions at the electrode/electrolyte interface. During the charging, the positive and negative ions of the electrolyte are separated and adsorbed by negative and positive electrodes, respectively. The energy storage mechanism is based on the formation of double layers of electrolyte ions at the interface of electrode and electrolyte. This is similar to the parallel plate capacitor and the capacitance of EDLC can be calculated by Eq. (1)

$$C = \frac{\epsilon\epsilon_0 A}{d} \quad (1)$$

where, C is the capacitance, ϵ_0 is the dielectric constant in vacuum, ϵ is the dielectric constant of the double layer, A is the area of the electrode and d is the thickness of double layer. Various models have been proposed to explain the formation of double layer. In 1853, Helmholtz first introduced the idea of double layer. When a charged conductor is placed in contact with electrolyte, the distribution of electric charges will be modified. Two layers of opposite charges will be formed at the interface of electrode and electrolyte. These two layers are separated by molecular dimensions but there is no exchange of ions between the layers. Hence the capacitance of the double layer can be obtained from the aforementioned Eq. (1). This model is widely used to explain the storage of supercapacitor. But this model did not taken care of the effects of ions behind the first layer of the ions at the electrode/electrolyte interface. Various carbonaceous materials (activated carbons, graphene, CNT etc.) store charges via EDLC mechanism. Carbon based materials were the first choice for the commercial applications because of their rapid response, good electrical conductivity, high chemical stability, non-toxicity, high abundance and simplicity of design. Carbonaceous materials have very high specific surface area ($1000\text{--}3500 \text{ m}^2 \text{ g}^{-1}$) which is very useful for the charge storage since EDLC is a surface dependent phenomenon. But with the increase of specific surface area and porosity the stability and conductivity of the material decreases. In spite of this, mesoporous nature with high specific surface area is very much important for its application as an active electrode [9, 16–18].

3.2 Pseudocapacitor

Another class of supercapacitor is pseudocapacitors which rely on the reversible redox reaction or Faradic reaction to store energy. Mainly transition metal oxides (e.g. ruthenium oxide, nickel oxide, manganese oxide, vanadium pent oxide etc.) and conducting polymer (polyaniline, polypyrrole, PEDOT:PSS, etc.) belongs to this group. Close surface to the electrolyte take part in redox reactions and this process can be classified into three distinct types which are underpotential deposition (adsorption pseudocapacitance), redox pseudocapacitance and intercalation

pseudocapacitance. Underpotential deposition arises when reversible adsorptions as well as removal of atoms occur at metal surface in two dimensional Faradic reactions. Redox pseudocapacitance exists when reversible redox reactions taken place at the electrode surface. In case of intercalation pseudocapacitance, ions are electrochemically intercalated into the structure of redox materials.

Although these three mechanisms are physically different from each other but they can be electrochemically governed by the Nernst equation. According to this equation, if the reaction potential E can be approximated by a linear function of $(1 + Q_r)/Q_r$, the specific capacitance can be obtained from Eq. (2)

$$C_m = \frac{nF}{mE} \left(\frac{1 + Q_r}{Q_r} \right) \quad (2)$$

where, n is the number of electron, F is the Faraday constant, m is the molecular weight of active electrode and Q_r is the reaction quotient. Transition metal oxides are chosen as the active materials for supercapacitor electrode and they store charge via Faradic or redox mechanism. They exhibit large theoretical specific capacitance with multiple valence states which enables them one of the most studied materials group in the field of supercapacitor [1, 19].

3.3 Hybrid supercapacitor

Hybrid supercapacitors are third type of supercapacitors which combine the features of both EDLCs and pseudocapacitors. The electrodes of hybrid supercapacitors are made with composite materials that include EDLC materials (carbonaceous materials such as activated carbon, graphene, CNT etc.) and pseudocapacitive materials (transition metal oxides and conducting polymers). There can also be asymmetric supercapacitor with one pseudocapacitive electrode and another EDLC electrode or hybrid electrode or vice-versa. Several binary and ternary composite based on polymer and CNTs have been prepared for electrochemical capacitive energy storage application. They offer large specific capacitance compare to individual one, which is due to the strong interaction between polymer and CNTs. Gupta and Miural were the first to propose that SWNT/PANI composite can be effectively used as the electrodes for supercapacitors. The highest specific capacitance value of 463 F g^{-1} was obtained for 27 wt% CNT.

4. Electrolytes

Besides the electrodes, another most important factor which can expressively influence the electrochemical performance of supercapacitor device is electrolyte. Generally, electrolyte exists in inside the separator as well as inside the active material layers. The important factors for an electrolyte are one wide potential window which is key factors to achieve higher energy density and the other is the high ionic concentration, low resistivity, low viscosity etc. which can also influence the power density of the supercapacitor device. There are three types of electrolyte usually used in supercapacitors: aqueous electrolyte, organic electrolytes and ionic electrolytes. Aqueous electrolytes (such as H_2SO_4 , KOH , Na_2SO_4 , HCl , NaCl and NH_4Cl aqueous solution and so on) limit the cell voltage window of supercapacitor to typically 0–1 V due to their low electrochemical stability, which effectively reduces the energy density of the cell. It can also provide a higher ionic concentration with conductivity up to 1.0 S cm^{-1} . Supercapacitors containing aqueous electrolyte may exhibit higher charge storage capacity but the main drawback is in terms of improving both energy and power densities due to their narrow working

potential window. To overcome this drawback now-a-days researchers are interested in using organic electrolytes as the main advantage of an organic electrolyte is it can provide wide potential window ~ 3.5 V. Since the energy density of a supercapacitor is directly proportional to the square of the cell voltage thus the organic electrolyte is much more suitable compared to other electrolytes. Among various organic electrolytes, acetonitrile and propylene carbonate (PC) are commonly used solvents. Propylene carbonate (PC)-based electrolytes are eco-friendly and can offer a wide electrochemical window, a wide range of operating temperature, as well as good electrical conductivity. In addition to promising advantages, the high cost, safety concern and toxic in nature still limit their commercial applications. Ionic electrolyte also known as room temperature molten salts-ionic liquids is one of the most promising electrolytes for the next generation energy storage application. Ionic electrolyte have lots of advantages such as high thermal stability, non-toxicity, non-flammability, high electrochemical stability and various combination of choices of cations and anions. But the low ionic conductivity at room temperature of ionic liquids is a great issue for practical application [20, 21].

5. Method for calculation of specific capacitance

The cyclic voltammetry (CV) curve of active working electrode materials measured in any suitable electrolyte solution (organic, ionic and aqueous electrolyte) epitomizes the total stored charge which ascends from both Faradic and non-Faradic process. The presence of oxidation/reduction peaks in CV curve represents the Faradic charge transfer reaction between electrolyte and electrode material. The total charge stored in electrode material can be calculated using Eq. (3):

$$C_m = \frac{i}{2mv} \quad (3)$$

where m and v are the mass of the electroactive material and potential scan rate, respectively. Current (i) can be obtained by integrating the area of the curves using Eq. (4)

$$i = \frac{\int_{V_a}^{V_c} i(v)dv}{V_c - V_a} \quad (4)$$

where V_a and V_c are the lowest and highest voltage of the potential range, respectively.

The specific capacitance value of the material can also be calculated from Galvanostatic charge discharge (GCD) profiles by using Eq. (5)

$$C_m = \frac{i}{m \left(-\frac{dV}{dt} \right)} \quad (5)$$

where 'i' is the current applied, dV/dt is the average slope of the discharge curve and m is the mass of active electrode materials [22, 23].

6. TiO₂-V₂O₅ nanocomposites as supercapacitor applications

Among various transition metal oxides, vanadium oxides (V₂O₅) also known as vanadium pentoxides have already been studied as a promising supercapacitor electrode material for energy storage application due to its excellent physical properties,

layered structure, non-toxic in nature, easy synthesis process, presence of several oxidation states (+2 to +5) and high specific capacity. But its low electrical conductivity limits its practical device application. The charge storage mechanism of a supercapacitor strongly depends on the surface properties of the electrode materials so the nanomaterial is suitable for electrode fabrication. Nanomaterial possesses high surface area along with high surface energy but the aggregation of nanoparticles is the most challenging problem. This effectively increases the strain for electrolyte ions diffusion within the nanoparticles at the surface of the electrode. Therefore, people are working to design and fabricate three-dimensional (3D), ordered and mesoporous nanomaterial to overcome such type of problem. There are four fundamental steps to control the charge storage behaviors of nanomaterials: (i) electron hopping between two nanoparticles; (ii) electron hopping within single nanoparticle; (iii) electron hopping between active electrode materials and current collectors; finally (iv) diffusion of proton within nanoparticles. It is well known that the proton diffusion and electron hopping within the nanoparticles are intrinsic properties of nanoparticles but the resistance due to intra-particle electron hopping can be diminished by loading it on a stable metal oxide [2]. It has also been observed practically that the loading on a stable metal oxide affects the increase of diffusion barrier of proton within the active materials and which follows the loss of effective sites. Because of the combination of TiO_2 with V_2O_5 Ti-O-V bonds are formed instead of metal-metal bonds which can result in an overall improvement of electrochemical activity and chemical stability due to the drop in the intra-particle electron-hopping resistance. Thus, TiO_2 - V_2O_5 nanocomposite can be a promising candidate for supercapacitor electrode in the near future. In this work, interconnected mesoporous TiO_2 - V_2O_5 nanocomposite has been synthesized which demonstrate tube like structure. The as synthesized electrodes of TiO_2 - V_2O_5 composite demonstrate kinetically fast charge-discharge properties along with long-cycle stability, which are commanding properties for supercapacitors [12, 23].

6.1 Morphological analysis

The field emission scanning electron microscopy (FESEM) images (**Figure 1(a)**) of TiO_2 - V_2O_5 nanocomposite shows ordered array of tube-like mesoporous structure. Because of large surface area, these mesoporous tube-like nanostructure can provide large number of active sites for competent ion diffusion. Due to increase in the contact area of the material with electrolyte ions, such type of surface improves the electrochemical activities of the electrode material. The active specific surface

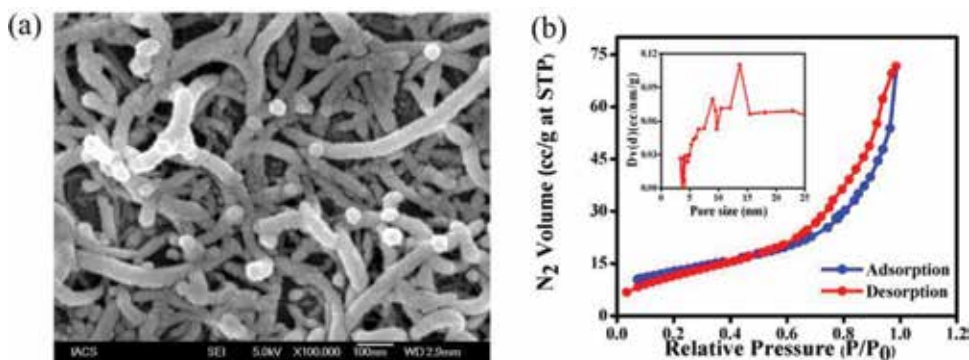


Figure 1. (a) FESEM image of TiO_2 - V_2O_5 composite; (b) N_2 adsorption-desorption isotherms and pore size distribution curve (inset) of as prepared TiO_2 - V_2O_5 .

area of this material has also been further characterized by nitrogen adsorption and desorption BET surface area measurement. The adsorption-desorption plot (**Figure 1(b)**) of the composite reveals the typical type-IV isotherm and also demonstrates the mesoporous nature of $\text{TiO}_2\text{-V}_2\text{O}_5$ nanostructure. The specific surface area calculated from the BET measurement is around $44\text{m}^2\text{ g}^{-1}$. This large surface area provides large contact area between the electrode/electrolyte interface enabling fast ion transfer which can improve the electrochemical performances of the electrode material. The corresponding pore size distribution of this electrode material measured from the isotherm BJH model is shown in **Figure 1b** (inset). The average pore size for this $\text{TiO}_2\text{-V}_2\text{O}_5$ nanostructure is around 8.90 nm, which implies that the material possesses a mesoporous like wide pore size distribution.

6.2 Electrochemical analysis

The CV curves of $\text{TiO}_2\text{-V}_2\text{O}_5$ composite (**Figure 2(a)**) with different scan rates (2, 10, 50 and 100 mV s^{-1}) signify a good electrochemical redox process. There is no O_2 or H_2 gas evolution observed at the ends of the potential windows which infers that this electrode can work in the wide potential window (-0.5 to $+1.3$ V) without suffering any degradation. The total charge stored in the electrode due to the redox reactions and pseudocapacitive behavior can be obtained from the total area enclosed by the CV curve for a particular scan rate. Same nature of CV curve for all scan rates reveals the good electrochemical performance of the electrode. This composite offers maximum specific capacitance of 310 F g^{-1} at a scan rate 2 mV s^{-1} . The synergistic effect of these two metal oxides enhances the conductivity of the composition.

The plot of variation of specific capacitance with scan rate (**Figure 2(b)**) shows that at lower scan rate the $\text{TiO}_2\text{-V}_2\text{O}_5$ nanocomposite electrode demonstrate higher capacitance value and it falls with increase of scan rate. This variation can be explained on the basis of movement of ions from electrolyte to electrode material. At lower scan rate, the electrolyte ions get enough time to contact the outer and interior active sites of the material which lead a large number of charge accumulation correspond to high specific capacitance value. Consequently, as the scan rate increase the mobility of charges per unit time increase as well as capacitance decrease due to less number of charge accretions on the outer surface of the electrode material. The charge storage mechanism of the electrode material can be studied according to the Power law, which explains that the total CV current is the sum of non-Faradic capacitive current and adsorptions/desorption currents. According to the Power law, scan rate dependent CV current of the electrode can be written as Eq. (6)

$$i = av^n \quad (6)$$

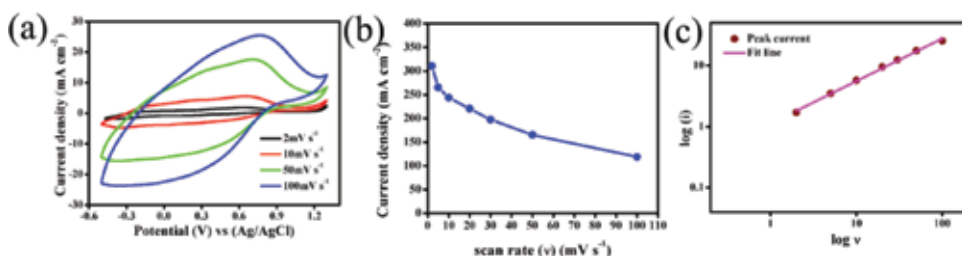


Figure 2. (a) CV curves at different scan rates; (b) specific capacitance vs. scan rate plot and (c) $\log(i_p)$ vs. $\log(v)$ plot for the $\text{TiO}_2\text{-V}_2\text{O}_5$ composite.

where, 'a' and 'n' are adjustable parameters and ν is scan rate [1, 22]. The value of 'n' can be obtained from slope of the linear fit $\log(i)$ vs. $\log(\nu)$ at a fixed potential. The 'n' value varies from zero to one. For pure resistor $n = 0$, for ideal diffusion control process $n = 0.5$ and for ideal capacitive process $n = 1.0$ i.e. non Faradic process. **Figure 2(c)** shows the plot of $\log(i)$ vs. $\log(\nu)$ of $\text{TiO}_2\text{-V}_2\text{O}_5$ nanocomposite. For this case, the 'n' value 0.69 reveals that the adsorption/desorption process dominates over capacitive mechanism i.e. the total current can be written as the combination of capacitive and adsorption/desorption current as

$$i = k_1(\nu) + k_2(\nu^{1/2}) \quad (7)$$

where $k_1(\nu)$ and $k_2(\nu^{1/2})$ signify the non-Faradic capacitive current and adsorption/desorption current, respectively. To calculate the value of k_1 and k_2 one can plot $i(\text{V})/\nu^{1/2}$ along y-axis and $\nu^{1/2}$ along x-axis. The slope and intercept of the linear fit gives the values of k_1 and k_2 , which can explain the contribution of the Faradic adsorption/desorption current and capacitive current to the total current. It can be concluded that the maximum amount of charge in the working electrode is accumulated based on the adsorption/desorption mechanism instead of capacitive mechanism. On the other hand, Trassati et al. first time reported that the total specific capacitance of an electrode material is the sum of two specific capacitance values provided by the outer and inner surface of the electrode i.e.

$$C_{total} = C_{in} + C_{out} (\text{Fg}^{-1}) \quad (8)$$

The two specific capacitances due to the influence of inner and outer surface of the electrode strongly depend on the scan rate (ν). The intercept of the linear fit of specific capacitance vs. $\nu^{1/2}$ plot at $\nu = 0$ gives the value of total specific capacitance (320 F g^{-1}) due to the diffusion of ions into the electrode which is nearly equal to the value obtained from CV curve (310 F g^{-1}). Similarly, the value of specific capacitance due to the outer surface of the electrode can be calculated from the plot of total specific capacitance vs. $\nu^{-1/2}$ plot and taking the intercept at $\nu = \infty$ and the value in this case is given by 81 F g^{-1} . Thus it can be concluded that the maximum capacitance value is mainly due to the contribution of inner active sites of the electrode which suggests that the charge storage mechanism is strongly based on adsorption/desorption process rather than capacitive process [1, 24].

To investigate the high performance electrochemical properties and kinetic information of $\text{TiO}_2\text{-V}_2\text{O}_5$ nanocomposite electrode materials EIS measurements have been done in the frequency range of 0.1 Hz to 100 kHz with AC perturbation amplitude of 10 mV. The EIS plot (**Figure 3(a)**) show frequency dependent three regions which can provide information about the kinetic nature of the electrode material. The small distorted semicircular curve at high frequency is due to the

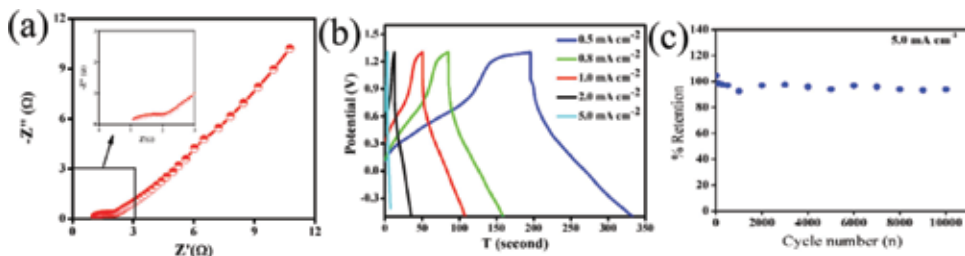


Figure 3. (a) EIS plot; (b) GCD plot at different current densities and (c) 10000-cycle stability analysis for the $\text{TiO}_2\text{-V}_2\text{O}_5$ composites.

charge transfer resistance within the electrode material. The diameter of the semi-circular portion gives the value of charge transfer resistance of the material. This semi-circular loop at high frequency can be modeled by a combination of parallel "RC" (R_{ct} - C_{dl}) circuit along with a series resistance (R_s). But, to describe the impedance behavior on the whole frequency range a more detailed circuit have to be considered. Moreover, as seen in FESEM, the electrode materials are particle in nature, the electrolyte can easily access the active material and thus a thin electrolyte film can locally separate the nanoparticles from each other resisting the electronic contact between the materials as well as with the current collector. Because of these two effects the interface resistance R_{ct} is increased. The high frequency loop is formed due to the current collector/ active material interface capacitance C_{dl} in association with the interface resistance R_{ct} . The electrolyte can easily penetrate within the porous electrode materials in the mid frequency range. A straight line corresponding to the frequency dependent Warburg impedance (W) is observed which arises due to the linear diffusion process of ions at the outer surface of the electrode material from electrolyte solution. At very low frequency almost a straight vertical line is observed which mainly originated due to the ions diffusion behavior, indicating very low diffusion resistances.

In order to further study the charge storage ability of synthesized TiO_2 - V_2O_5 nanocomposites electrode, GCD at various current densities (0.5, 0.8, 1.0, 2.0 and 5 mA cm^{-2}) has been performed. **Figure 3(b)** represents the GCD plots with potential windows from -0.5 to $+1.3$ V, which is reliable with the potential range of CV measurement. At lower current densities the composite exhibits good pseudocapacitive behavior and superior capacitive retention. Very small IR drop is also observed at the starting point of discharge time even at high current densities signifies that the electrode material offers very low internal series resistance (R_s) due to the electrolyte solution. However, the sample, due to its mesoporous morphology, accelerated the movement of K^+ and Cl^- ions through its channels inside the pores and reveals superior redox nature at higher current densities. The GCD cycling curves have a nearly symmetric shape at high current densities, indicating that the composite has a good electrochemical capacitive characteristic and superior capacitive retention. The maximum specific capacitance of 307 F g^{-1} has been obtained for TiO_2 - V_2O_5 nanocomposites at 0.5 mA cm^{-2} current density, which is almost equal to the value calculated from CV plots. It is also observed that the specific capacitance value decreases with increase of current densities which is mainly due to the decrease of accessibilities of electrolyte ions into the inner surface of the electrode material. The long-term cycle stabilities of prepared TiO_2 - V_2O_5 nanocomposite has been studied up to 10,000 cycles at a current density of 5.0 mA cm^{-2} as shown in **Figure 3(c)**. The electrode exhibits very good cycle life of 94% over 10,000 cycles. It has been well explained that both the transition metal oxide play significant role for improvement of excellent electrochemical behavior providing additional possibility of fast redox process even at higher current densities [23, 25].

6.3 Asymmetric supercapacitor device performance

6.3.1 Fabrication of asymmetric supercapacitor

The asymmetric supercapacitor (ASC) was fabricated with activated porous carbon (AC) as negative electrode, TiO_2 - V_2O_5 nanocomposite as positive electrode and 1 M Na_2SO_4 as the electrolyte with Whatman filter paper (pore diameter ~ 25 μm) as separator. The mass ratio of the active materials for negative and positive electrodes was around 2. All the supercapacitive studies of ASCs were

performed at 300 K. The specific energy (E_{cell}) ($W h kg^{-1}$) and specific power (P_{cell}) ($W kg^{-1}$) of the device have been calculated by using the Eqs. (9–11)

$$C_s = \frac{I \times \Delta t}{m(V_f - V_i)} \quad (9)$$

$$E_{cell} = \frac{1}{2} \left[\frac{C_s (V_f - V_i)^2}{3.6} \right] \quad (10)$$

$$P_{cell} = \frac{3600 \times E_{cell}}{\Delta t} \quad (11)$$

where C_s is the specific capacitance of the ASC devices ($F g^{-1}$), I is the discharge current (A), Δt is the discharge time (s), m is the combined mass of the both active electrode materials (g) and $(V_f - V_i)$ is the potential window within which the supercapacitor operate (V) [2]. The cyclic voltammograms (CV) of this fabricated ASCs device have been studied at different potential windows ranging between 0.5 and 1.3 V at a fixed scan rate of $100 mV s^{-1}$ (Figure 4(a)) and it shows no deviation in the shape of the voltammogram at 1.3 V which ensures that the ASC can operate up to 1.3 V. The CV curves of the ASC at different scan rates are shown in Figure 4(b). These curves show the increase of CV current with increasing scan

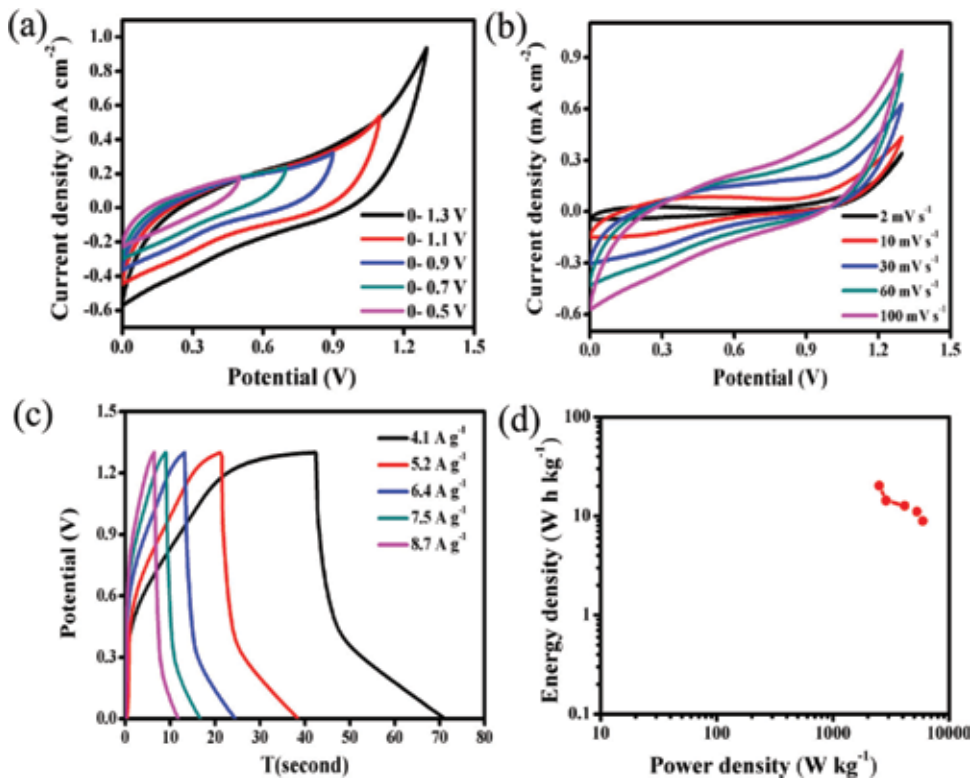


Figure 4. (a) CV curves at $100 mV s^{-1}$ for different window potentials; (b) CV curves at different scan rates for a fixed window; (c) GCD curves at different current densities and (d) energy density vs. power density plot for the $TiO_2-V_2O_5$ composite device.

rate. The GCD data at different current densities are shown in **Figure 4(c)** and the curves represent that the discharge time decrease with increasing current densities. The specific capacitances were calculated by using Eq. (10) and the value of maximum is 86 F g^{-1} at current density of 4.1 A g^{-1} . From the GCD curves it is clear that the specific capacitance decreases with increase of current densities. The specific energy and specific power of this device have also been calculated using Eqs. (10) and (11) and are shown in the form of Ragone plot in **Figure 4(d)**. The highest specific energy (E_{cell}) and specific power (P_{cell}) is of $20.18 \text{ W h kg}^{-1}$ and 5.94 kW kg^{-1} , respectively. Overall electrochemical study of $\text{TiO}_2\text{-V}_2\text{O}_5$ nanocomposite shows that it is an excellent positive electrode material for future applications.

7. NiMn_2O_4 as supercapacitor applications

Recently, single phase spinel-structured NiMn_2O_4 , a low cost, non-toxic ternary metal oxide, has received a great interests over many other metal oxides due to its excellent electrochemical performance. As has been stated earlier, to be used as electrodes in supercapacitors, materials with good electrical conductivity and excellent electrochemical performance are needed for achieving high energy density and high power density. In this context, nanostructured materials are more suitable than traditional bulk materials as electrode materials for supercapacitor, as they offer higher surface to volume ratio and shorter electron-ions transport channels. In fact, metal oxide nanostructures become the target of modern research for their utilization in high performance energy storage devices. Moreover, the morphology of those nanostructures is seen to affect their electrochemical performance. Therefore, designing metal oxide nanostructures of controlled morphology and size with good electrical conductivity is a challenge for their utilization in energy storage devices such as electrochemical supercapacitors [12, 26].

7.1 Morphological characterization

FESEM image shows (**Figure 5(a)**) densely packed agglomerated spherical NiMn_2O_4 nanoparticles of sizes 6–10 nm ($\sim 8 \text{ nm}$ average size) are formed. Formation of such densely packed small NiMn_2O_4 nanoparticles effectively generates

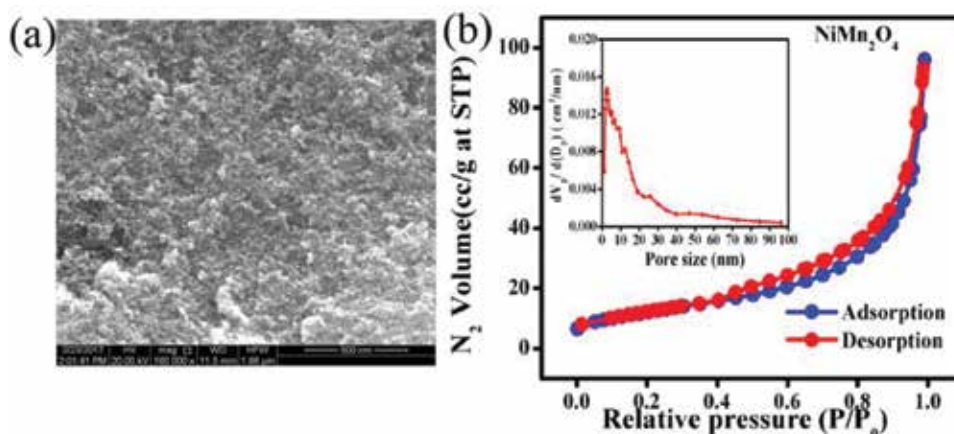
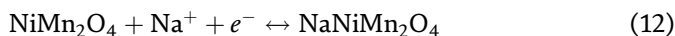


Figure 5.
(a) FESEM image of the NiMn_2O_4 nanoparticles; (b) N_2 adsorption-desorption isotherms and pore size distribution curve (inset) of as prepared NiMn_2O_4 .

porous surface of high specific surface area, which enhances the electrochemical performance of the electrodes due to high contact area of the material with electrolyte. The porous nature of the NiMn₂O₄ nanostructures is confirmed from their Brunauer-Emmett-Teller (BET) surface area measurement. The adsorption-desorption plots of the sample presented in **Figure 5(b)** clearly revealed a typical type IV isotherm which corresponds to the mesoporous nature of NiMn₂O₄ nanocrystals. The BET estimated specific surface area of the material is 43.6 m² g⁻¹ with average pore size 13.3 nm, which offers large number of active sites in the electrochemical process. Such a high specific surface area of the nanostructures can also provide a large contact area between the electrolyte solution and the electrode, ensuing fast ion transfer at the interface.

7.2 Electrochemical characterization

The cyclic voltammogram (CV) curves (**Figure 6(a)**) of the NiMn₂O₄ electrode at various scan rates in the potential range -1.0 to 1.3 V indicate the typical Faradic charge transfer behavior due to the presence of functional groups or pore size distribution. The non-rectangular shape of the CV curves specifies the redox nature of the electrode material and provides the information on the pseudocapacitive behavior of the electrode in a suitable electrolyte solution. There are several oxidation and reduction peaks (Mn³⁺ ↔ Mn⁴⁺ and Ni²⁺ ↔ Ni³⁺) in the CV curves, which can be clearly identified due to the faradic redox processes related to Eq. (12) [27].



The specific capacitance (C_m) of the electrode for each scan rate has been calculated from the CV curves by using Eqs. (7) and (8) and the maximum specific capacitance of 875 F g⁻¹ is obtained for a scan rate 2 mV s⁻¹. The GCD curves at different current densities (**Figure 6(b)**) indicate the pseudocapacitor type behavior with very low current densities at the potential corresponding to the Faradic reactions. A very small potential drop (IR-drop) has also been observed at the beginning of the discharge curve, even at high current densities, which indicates the NiMn₂O₄ electrode has a very low internal series resistance (R_s) within Na₂SO₄ electrolyte solution, as well as low contact resistance at the interface of current collector and electrolyte solution. A decrease of charging/discharging time with increasing current density can be clearly perceived from the GCD curves, which can

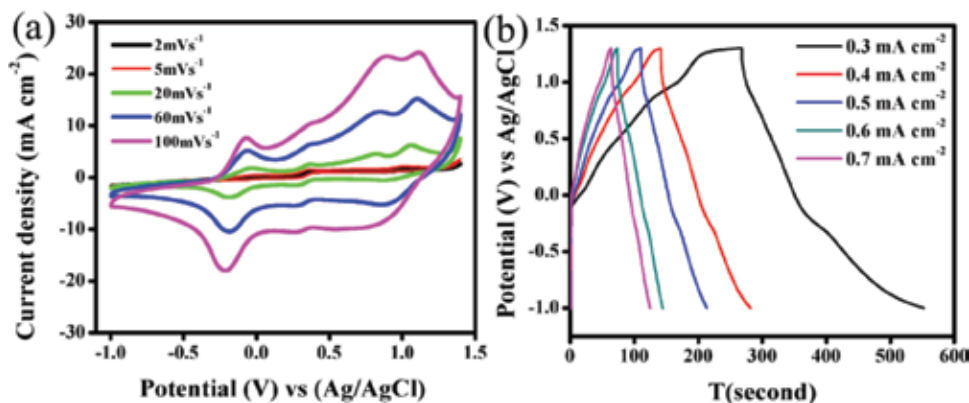


Figure 6. (a) CV curves at different scan rates and (b) GCD curves at different current densities for the NiMn₂O₄ composite.

be explained considering ion diffusion mechanism. At lower current densities, a large surface area of the electrode is occupied by Na^+ ions from electrolyte solution as they get enough time to access the maximum active sites of the electrode material, offering higher specific capacitance value. Conversely, due to limited accessibility of the Na^+ ions inside the electrode material, the specific capacitance of the electrode is lower at higher current densities. The specific capacitance value can also be calculated from the GCD profile at a given current density, using Eq. (8) and the maximum capacitance obtained 820 F g^{-1} at 4.0 A g^{-1} . The electrodes fabricated using NiMn_2O_4 nanoparticles exhibit very high cycle life of about 91% over 10,000 cycles, indicating the oxides of both the elements (Ni and Mn) play significant roles for the improvement of electrochemical performance of the electrode.

7.3 Device characterization

It is known that for asymmetric supercapacitors (ASCs) the charge stored at two opposite electrodes (positive and negative) should be equal and opposite i.e. $q^+ = q^-$ [28, 29]. The amount of charge stored by the each electrode generally depends on the specific capacitance (C_m), mass of the electrode (m) and potential windows (ΔV). The ratio of two electrode mass essential to follow:

$$\frac{m_+}{m_-} = \frac{C_- \times (\Delta E)_-}{C_+ \times (\Delta E)_+} \quad (13)$$

Figure 7(a) represents the cyclic voltammograms (CV) of this fabricated ASCs device at different potential windows (0–0.9V, 0–1.1V, 0–1.3V, 0–1.5V and 0–1.8V). All CV curves show same nature which indicates that this device can performs within

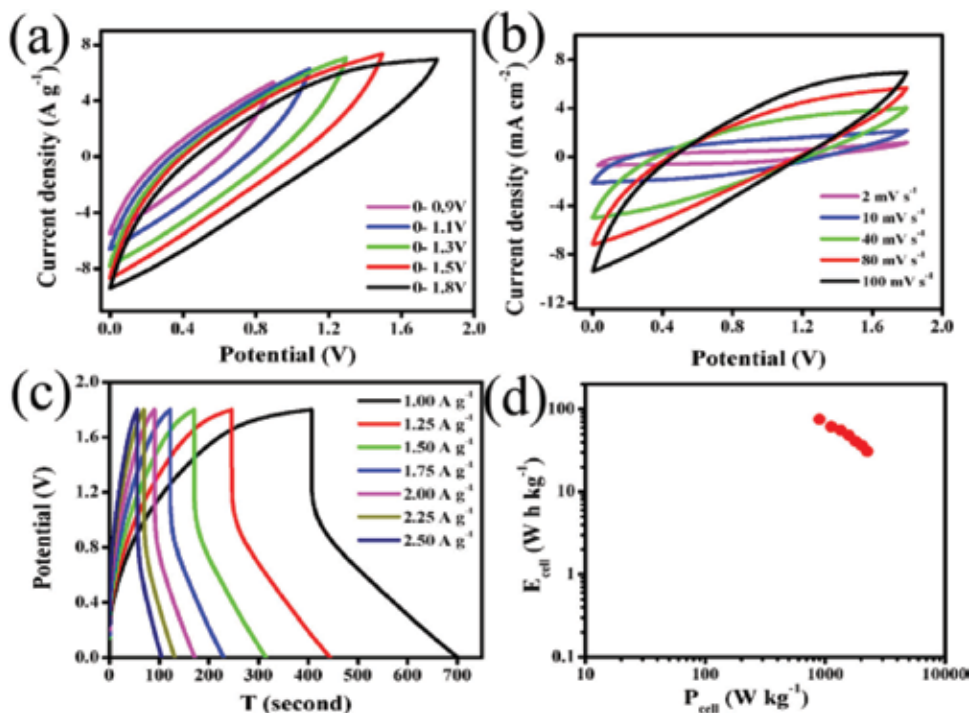


Figure 7. (a) CV curves at 100 mV s^{-1} for different window potentials; (b) CV curves at different scan rates for a fixed window; (c) GCD curves at different current densities and (d) energy density vs. power density plot for the NiMn_2O_4 composite.

maximum potential window 0–1.8 V without any degradation. Thus, all electrochemical studies have been done within maximum potential window from 0 to 1.8 V and the CV curves (**Figure 7(b)**) at different scan rates show relatively rectangular nature without presence of any redox peaks. It clearly indicates that the charge storage mechanism is mainly due to the electric double layer of the device. The CV profiles also remain almost same without any distortion with increasing scan rates, indicating suitable fast charge–discharge property. To study the rate capability of this ASC device, the GCD test at different current densities (1.0, 1.25, 1.50, 1.75, 2.00, 2.25 and 2.50 A g⁻¹) has been performed. The GCD plots (**Figure 7(c)**) show that the discharge time decreases with increasing current density. For practical purpose it is expected that a good supercapacitor device provides high specific capacitance and high energy density. The relationship between specific capacitance vs. current density of the fabricated ASC device shows that the device delivers maximum specific capacitance of 166.7 F g⁻¹ at current density 1 A g⁻¹. The specific capacitance also decreases when current density increases, since diffusion of electrolyte ions and electrons most likely are restricted due to the time constrain. The specific energy and power densities of the ASC have been calculated from the discharge curves at different current densities in the voltage window of 0–1.8 V and the Ragone plot is shown in **Figure 7(d)**. This device delivers offers specific energy density and power density of 75.01 W h kg⁻¹ and 2.25 kW kg⁻¹, respectively. The ASC device configuration (**Figure 7d**) presents a columbic efficiency 97.6% indicating that the device is suitable for high-performance supercapacitor applications in future.

8. Conclusion

In summary, the electrochemical properties of TiO₂-V₂O₅ and NiMn₂O₄ composites have been demonstrated. Three dimensional, mesoporous, interlinked tube-like ordered architecture of TiO₂-V₂O₅ nanocomposite offers large surface area which enhances the specific capacitance. The composite offers maximum specific capacitance of 310 F g⁻¹ in 1 M KCl solution at 2 mV s⁻¹ scan rate. It is found out that the maximum capacitance value arises from the contribution of inner active sites of the electrode rather than the outer surface. The NiMn₂O₄ nanoparticles with ~8 nm average diameter show spherical shape with BET surface area of 43.6 m² g⁻¹. The agglomerated spinel nanoparticles generate highly porous structures, which can be utilized to fabricate working electrodes of the electrochemical supercapacitors. The electrodes made of NiMn₂O₄ nanoparticles possess excellent charge storage characteristics, with specific capacitance of up to 875 F g⁻¹ attainable at a scan rate of 2 mV s⁻¹ in 1.0 M Na₂SO₄ electrolyte solution. The coexistence of Ni and Mn in the lattice of this binary oxide is seen to have a positive effect on the improvement of electrochemical charge storage capability of the electrodes due to enhanced electronic conductivity. Both these two composites demonstrate excellent device performance. The asymmetric device based on TiO₂-V₂O₅ shows specific capacity of 86 F g⁻¹ at 4.2 A g⁻¹ with the maximum energy density (E_{cell}) and power density (P_{cell}) about 20.18 W h kg⁻¹ and 5.94 kW kg⁻¹, respectively. On the other hand the asymmetric device based on NiMn₂O₄ demonstrates 166.7 F g⁻¹ at current density 1 A g⁻¹ with specific energy density and power density of 75.01 W h kg⁻¹ and 2.25 kW kg⁻¹, respectively. These superior performances ensure that these composites can be used as the electrodes for future energy storage devices.

Acknowledgements

A. Ray (File No.–09/096(0927)/2018-EMR-I) and S. Saha (File No.–09/096 (0898)/2017–EMR-I) wish to thank CSIR, Government of India for financial support. S. Das is thankful to the Department of Science and Technology (DST), Government of India, for providing research support through the ‘INSPIRE Faculty Award’ (IFA13-PH-71). A. Roy (IF140920) is also thankful to the Department of Science and Technology (DST), INSPIRE, Government of India, for providing research support through the ‘INSPIRE Fellowship’.

Conflict of interest


All the authors declare that there is no conflict of interest.

Author details

Apurba Ray, Atanu Roy, Samik Saha and Sachindranath Das*
Department of Instrumentation Science, Jadavpur University, Kolkata, India

*Address all correspondence to: sachindas15@gmail.com

IntechOpen

© 2018 The Author(s). Licensee IntechOpen. This chapter is distributed under the terms of the Creative Commons Attribution License (<http://creativecommons.org/licenses/by/3.0>), which permits unrestricted use, distribution, and reproduction in any medium, provided the original work is properly cited. 

References

- [1] Roy A, Ray A, Saha S, Das S. Investigation on energy storage and conversion properties of multifunctional PANI-MWCNT composite. *International Journal of Hydrogen Energy*. 2018;**43**:7128-7139
- [2] Ray A et al. Electrochemical properties of $\text{TiO}_2\text{-V}_2\text{O}_5$ nanocomposites as a high performance supercapacitors electrode material. *Applied Surface Science*. 2018;**443**: 581-591
- [3] NASA. 2009: Second Warmest Year on Record; End of Warmest Decade. 2010, January 21. [Accessed: November 30, 2010]
- [4] Ng CH et al. Cesium lead halide inorganic-based perovskite-sensitized solar cell for photo-supercapacitor application under high humidity condition. *ACS Applied Energy Materials*. 2018. DOI: 10.1021/acs.aem.7b00103
- [5] Ngaotrakanwivat P, Meeyoo V. $\text{TiO}_2\text{-V}_2\text{O}_5$ nanocomposites as alternative energy storage substances for photocatalysts. *Journal of Nanoscience and Nanotechnology*. 2012;**12**:828-833
- [6] Wang J et al. Nanocellulose-assisted low-temperature synthesis and supercapacitor performance of reduced graphene oxide aerogels. *Journal of Power Sources*. 2017;**347**:259-269
- [7] Jampani PH et al. High energy density titanium doped-vanadium oxide-vertically aligned CNT composite electrodes for supercapacitor applications. *Journal of Materials Chemistry A*. 2015;**3**:8413-8432
- [8] Li X. Improved electrocatalytic activity and durability of $\text{NiMn}_2\text{O}_4\text{-CNTs}$ as reversible oxygen reaction electrocatalysts in zinc-air batteries. *ECS Transactions (ECST)—The Electrochemical Society*. 2017;**80**: 129-134
- [9] Conway BE. *Electrochemical supercapacitors. Scientific Fundamentals and Technology Applications*. Ch 9; 1999
- [10] Conway BE. Transition from “supercapacitor” to “battery” behavior in electrochemical energy storage. *Journal of the Electrochemical Society*. 1991;**138**:1539
- [11] Ali GAM, Tan LL, Jose R, Yusoff MM, Chong KF. Electrochemical performance studies of MnO_2 nanoflowers recovered from spent battery. *Materials Research Bulletin*. 2014;**60**:5-9
- [12] Ngo YLT, Sui L, Ahn W, Chung JS, Hur SH. NiMn_2O_4 spinel binary nanostructure decorated on three-dimensional reduced graphene oxide hydrogel for bifunctional materials in non-enzymatic glucose sensor. *Nanoscale*. 2017;**9**:19318-19327
- [13] Liu S et al. Nb_2O_5 quantum dots embedded in MOF derived nitrogen-doped porous carbon for advanced hybrid supercapacitor applications. *Journal of Materials Chemistry A*. 2016;**4**:17838-17847
- [14] Rusi, Majid SR. Green synthesis of in situ electrodeposited rGO/MnO_2 nanocomposite for high energy density supercapacitors. *Scientific Reports*. 2015;**5**:1-13
- [15] Vijaya Sankar K et al. Studies on the electrochemical intercalation/de-intercalation mechanism of NiMn_2O_4 for high stable pseudocapacitor electrodes. *RSC Advances*. 2015;**5**: 27649-27656

- [16] Tully KC, Whitacre JF, Litster S. Spatiotemporal electrochemical measurements across an electric double layer capacitor electrode with application to aqueous sodium hybrid batteries. *Journal of Power Sources*. 2014;**248**:348-355
- [17] Wu N, Low J, Liu T, Yu J, Cao S. Hierarchical hollow cages of Mn-Co layered double hydroxide as supercapacitor electrode materials. *Applied Surface Science*. 2017;**413**:35-40
- [18] De Pauli CP, Trasatti S. Electrochemical surface characterization of IrO₂ + SnO₂ mixed oxide electrocatalysts. *Journal of Electroanalytical Chemistry*. 1995;**396**: 161-168
- [19] Chen LY, Hou Y, Kang JL, Hirata A, Chen MW. Asymmetric metal oxide pseudocapacitors advanced by three-dimensional nanoporous metal electrodes. *Journal of Materials Chemistry A*. 2014;**2**:8448-8455
- [20] Béguin F, Presser V, Balducci A, Frackowiak E. Carbons and electrolytes for advanced supercapacitors. *Advanced Materials*. 2014;**26**:2219-2251
- [21] Akinwolemiwa B, Peng C, Chen GZ. Redox electrolytes in supercapacitors. *Journal of the Electrochemical Society*. 2015;**162**:A5054-A5059
- [22] Ray A et al. Correlation between the dielectric and electrochemical properties of TiO₂-V₂O₅ nanocomposite for energy storage application. *Electrochimica Acta*. 2018;**266**:404-413
- [23] Roy A et al. NiO-CNT composite for high performance supercapacitor electrode and oxygen evolution reaction. *Electrochimica Acta*. 2018;**283**: 327-337
- [24] Ardizzzone S, Fregonara G, Trasatti S. 'Inner' and 'outer' active surface of RuO₂ electrodes. *Electrochimica Acta*. 1990;**35**:263-267
- [25] Lin JY, Huang JJ, Hsueh YL, Zhang YX. Diameter effect of silver nanowire doped in activated carbon as thin film electrode for high performance supercapacitor. *Applied Surface Science*. 2017. DOI: 10.1016/j.apsusc.2017.10.008
- [26] Maiti S, Pramanik A, Dhawa T, Sreemany M, Mahanty S. Bi-metal organic framework derived nickel manganese oxide spinel for lithium-ion battery anode. *Materials Science and Engineering: B*. 2018;**229**:27-36
- [27] Arsent'ev MY, Koval'ko NY, Shmigel' AV, Tikhonov PA, Kalinina MV. NiMn₂O₄ spinel as a material for supercapacitors with a pseudocapacity effect. *Glass Physics and Chemistry*. 2017;**43**:376-379
- [28] Li S et al. High-performance flexible asymmetric supercapacitor based on CoAl-LDH and rGO electrodes. *Nano-Micro Letters*. 2017;**9**:1-10
- [29] Wang R, Sui Y, Huang S, Pu Y, Cao P. High-performance flexible all-solid-state asymmetric supercapacitors from nanostructured electrodes prepared by oxidation-assisted dealloying protocol. *Chemical Engineering Journal*. 2018;**331**: 527-535

CrN Sputtered Thin Films for Supercapacitor Applications

Mohammad Arif, Amit Sanger and Arun Singh

Abstract

The growing demand of energy storage device has attracted significant attention toward transition metal nitrides because of their remarkable mechanical, electronic, and catalytic applications. Here, sputtered chromium nitride thin films deposited on steel substrate have been used as a working electrode for supercapacitor application. The deposited columnar CrN thin films show (111) and (200) planes of cubic phase. The electrochemical properties of CrN working electrode exhibit high specific capacitance of 41.8 F/g at the scan rate of 5 mV/s with excellent capacitance retention up to 2000 cycles. The supercapacitive performance of the CrN films suggests the potential application for supercapacitors.

Keywords: energy storage, supercapacitor, chromium nitride, sputtering

1. Introduction

Increasing impetus for renewable energy has directed the extensive growth of semiconductor technology market during the last decade. Among various energy storage devices, supercapacitor (SC) and lithium-ion battery (LIB) are the most anticipated devices [1]. Comparatively, SCs have better power density, charging/discharging ability, and reversibility to LIBs. Based on the mechanism, SCs are categorized into electrical double-layer capacitors (EDLCs) and pseudocapacitors [2, 3]. Currently, metal oxides are extensively used for SCs because of their high pseudocapacitance. However, these materials suffer low electrical conductivity and fickle stability during long cycles [4].

Therefore, exploring new materials and design for future advancement of the electrochemical properties of supercapacitors is prime requirement. Recently, metal nitrides are found to be prospective contenders for electrochemical applications because of their exceptional thermal and mechanical stability, high melting point, hardness, and excellent electrical conductivity (4000–55,500 S/cm) [5–11]. Among various metal nitrides, cubic CrN films are widely used in optoelectronics and MEMS applications due to its large bandgap [12, 13]. However, electrochemical capabilities of CrN nanostructured films were not emphasized. CrN films can be synthesized by physical vapor deposition methods, chemical vapor deposition, and ammonolysis [14]. Among these, sputtered CrN films are uniform, reproducible, and highly pure.

Herein, sputtered CrN thin films were deposited on steel substrate. The supercapacitive behavior of CrN working electrodes were examined via cyclic voltammetry (CV) and electrochemical impedance spectroscopy (EIS).

2. Experimental details

In this study, supercapacitor working electrodes were fabricated using 304L stainless steel as current collector (0.5 mm thick, 9 cm² area) coated with sputter CrN thin film. Prior to deposition, the steel substrates were polished with SiC abrasive paper and ultrasonically washed with alcohol and acetone, respectively. The thin film deposition was carried out for 60 min by applying 50 W power and 5 mTorr (Ar:N₂::1:1) working pressure using Cr target (99.99% pure, Testbourne Ltd., UK), keeping the current collector at 5 cm and 300°C.

The sputtered CrN thin films were characterized via X-ray diffraction (Bruker AXS, D8 advance), FE-SEM (Carl Zeiss, Ultra plus), energy dispersive X-ray analysis (EDAX, Oxford Instruments), Raman spectroscopy (Renishaw, United Kingdom), and X-ray photoelectron spectroscopy (XPS, PerkinElmer model 1257). The supercapacitive behavior of CrN working electrodes was examined via electrochemical workstation (CHI-660D) in a three-electrode cell in 1 M Na₂SO₄ solution.

The specific capacitance (F/g) of working electrode was calculated from the CV curves using Eq. (1), respectively:

$$C_s = \frac{Q}{m \times \Delta V} = \frac{\int_{-V}^V I(V) dV}{m \times \Delta V \times v} \quad (1)$$

Where specific capacitance C_s is in F/g, Q is charge in coulomb, m is mass of the active material in gram, v is the scan rate in V/s, and ΔV is the potential window between the positive (V+) and negative (V-) electrodes in volt [3]. The loading mass of active material was around ~12 mg.

3. Results and discussion

As depicted in **Figure 1**, the XRD spectrum of sputtered cubic CrN thin films shows three characteristic peaks at 37.45°, 43.35°, and 63.37° corresponding to (111), (200), and (220) planes (JCPDS file no. 110065) [15]. The working electrode also shows three characteristic peaks at 44.54°, 50.56°, and 73.96° corresponding to (111), (200), and (220) planes of cubic phase of 304 L steel substrate (JCPDS file no. 10752128) [16].

As shown in **Figure 2**, the CrN thin film depicts two Raman active modes centered at 238 cm⁻¹ corresponding to vibrations of metal atoms, and 619 cm⁻¹ corresponding to vibrations of lighter nonmetal ions [17].

As depicted in **Figure 3**, XPS measurements were carried out to study the chemical structure of CrN film. The XPS spectra of N1 s depict two binding energies peaks at 396.96 and 398.56 eV, corresponding to the CrN and adsorbed nitrogen, respectively (**Figure 3a**). The XPS spectra of Cr₂P_{3/2} depict a peak at 575.76 eV corresponding to CrN (**Figure 3b**), well corroborated with the XRD and Raman results [18].

As depicted in **Figure 4a** and **b**, the FE-SEM images represent columnar porous morphology of CrN working electrode. The EDS spectra represents the stoichiometric chemical composition (1:1) of CrN working electrode.

To compare the CrN film and current collector, the CV curves were measured at a high scan rate of 200 mV/s. The CV curve depicted that CrN film is key contributor in supercapacitive performance as working electrode swept a more area than that of the current collector (**Figure 5a**). The CV plots of working electrode were tested between 0 and 1.2 V range at scan rates 5–200 mV/s in 1 M Na₂SO₄

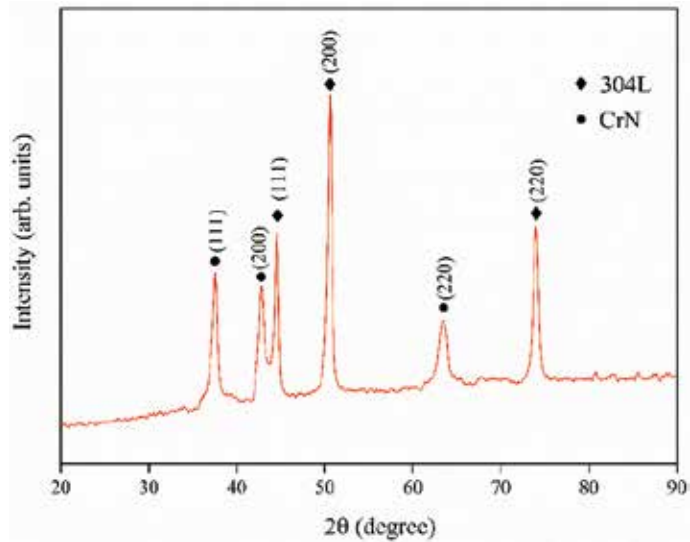


Figure 1. XRD pattern of CrN working electrode. (Adapted from Mohd. Arif et al., with permission from Elsevier. Copyright 2018) [23].

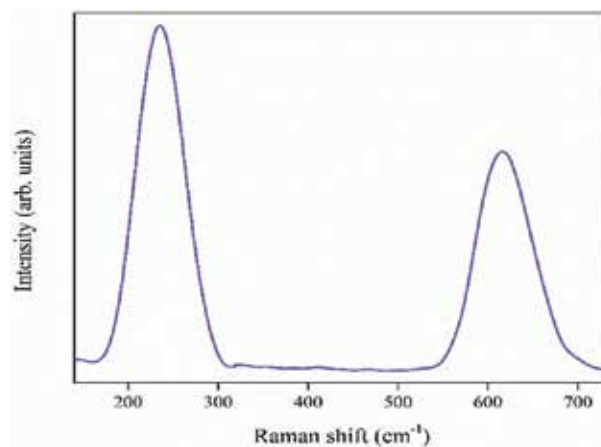


Figure 2. Raman spectrum of CrN thin film. (Adapted from Mohd. Arif et al., with permission from Elsevier. Copyright 2018) [23].

solution (**Figure 5b**). The CV curves of working electrode showed the symmetric and reversible plots with good capacitive behavior [19]. The plot between specific capacitance (C_s) versus scan rates is represented in **Figure 5c**, showing 41.66, 31.25, 16.7, 12.5, and 11.2 F/g at the scan rates of 5, 20, 50, 100, and 200 mV/s, respectively, well corroborated with the available literature [18, 20].

Table 1 shows the specific capacitance values of present case along with previously reported literature. As shown in **Figure 5d**, the CrN working electrode demonstrated excellent capacitance retention of 87% after 2000 cycles at a scan rate of 200 mV/s [21]. The reduction in capacitive retention is due to the dissolution of active sites of CrN films.

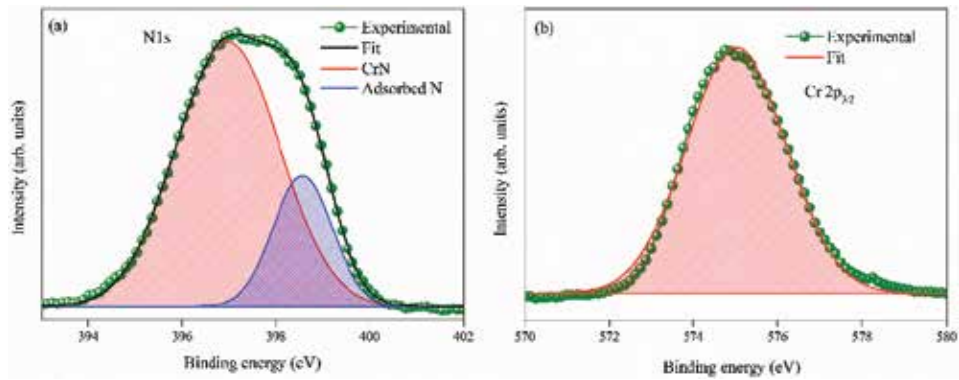


Figure 3. (a) XPS spectra of $N1s$, and (b) XPS spectra of $Cr2p_{3/2}$. (Adapted from Mohd. Arif et al., with permission from Elsevier. Copyright 2018) [23].

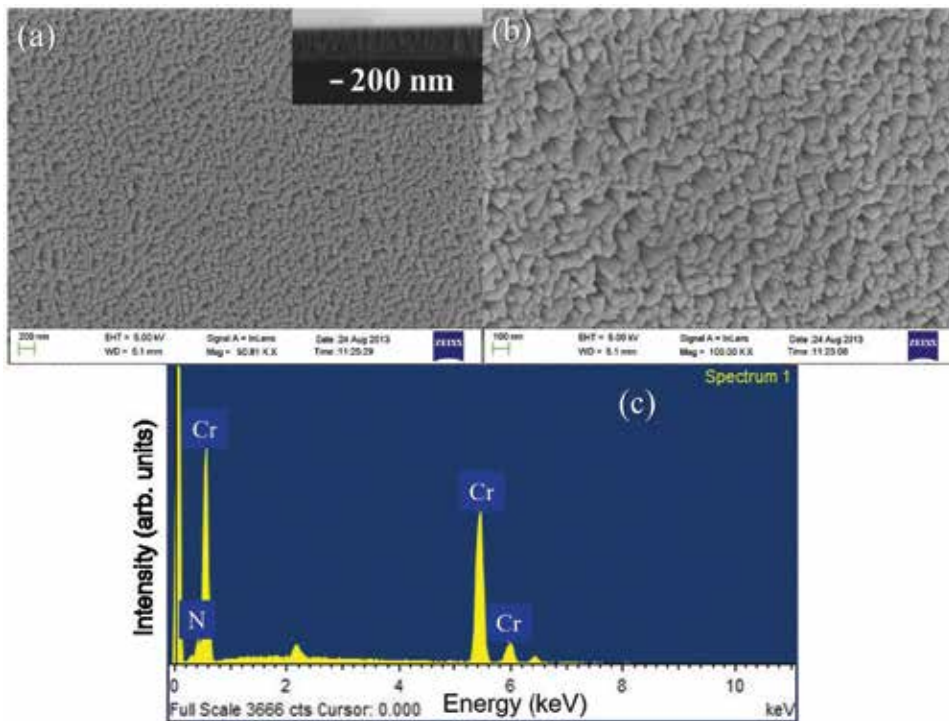


Figure 4. (a and b) FE-SEM images of CrN thin film at different scales, 200 and 100 nm scales, and (c) EDS spectrum of CrN thin film. (Adapted from Mohd. Arif et al., with permission from Elsevier. Copyright 2018) [23].

The EIS spectroscopy of CrN working electrode was measured between the frequency range of 0.01 and 100 kHz. As depicted in **Figure 5e**, the Nyquist plot of CrN working electrode showed a straight line in low frequency range, which represents the diffusion of ions at the electrode-electrolyte interface [22]. The Nyquist plot of CrN working electrodes showed a semicircle in high frequency range, which represents the electronic resistance and contact resistance between active material and current collector (inset of **Figure 5e**). The equivalent circuit model of working electrode is shown in **Figure 5f**. From the EIS circuit model, the electrolyte resistance (R_s) was found to be 1.77Ω , corresponding to good ionic conductivity of the

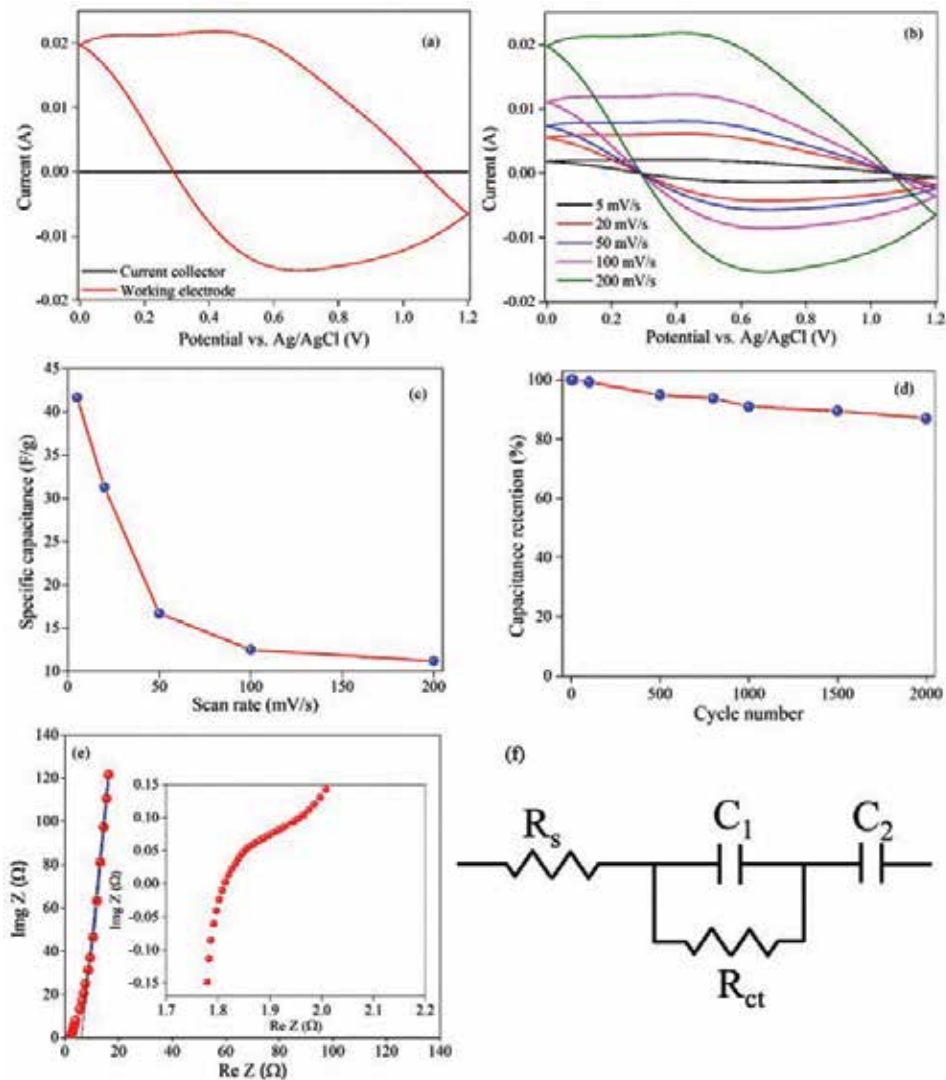


Figure 5. (a) CV curve of CrN working electrode and steel current collector at 200 mV/s, (b) CV curve of CrN working electrode at different scan rates, (c) specific capacitance vs. scan rate graph, (d) capacitive retention curve of CrN thin film working electrode, (e) Nyquist plot (inset shows the enlarged Nyquist plot at the high frequency region), and (f) corresponding equivalent circuit model. (Adapted from Mohd. Arif et al., with permission from Elsevier. Copyright 2018) [23].

Sample	Method	Electrolyte specific	Capacitance	References
CrN thin film	Sputtering	0.5 M H ₂ SO ₄	12.8 mF/cm ² at 1 mA/cm ²	[17]
CrN/activated carbon nanoparticles	Chemical method	1 M LiPF ₆	50 F/g at 1 mV/s	[19]
CrN thin films	Sputtering	1 M Na ₂ SO ₄	41.6 F/g at 5 mV/s	This work

Table 1. Comparison of the specific capacitance of chromium nitride-based supercapacitor electrodes reported in the literature. (Adapted from Mohd. Arif et al., with permission from Elsevier. Copyright 2018) [23].

electrolyte. The charge transfer resistance (R_{ct}) was found to be 6.15Ω , owing to the contact between CrN film and steel substrate.

4. Conclusion

In summary, the supercapacitive behavior of sputter-deposited columnar-type cubic CrN-coated working electrode was tested. The CrN working electrode shows high specific capacitance of 41.6 F/g in $1 \text{ M Na}_2\text{SO}_4$ at the scan rate of 5 mV/s with the excellent capacitance retention (87% after 2000 cycles). These good electro-chemical properties demonstrated that the CrN-based supercapacitor electrode has excellent potential in supercapacitor applications.

Acknowledgements

M. Arif and A. Sanger have equal contribution in this chapter. The authors would like to acknowledge the financial support from the Department of Science & Technology (DST), Ministry of Science & Technology, India.

Conflict of interest

The authors declare no conflict of interest.

Author details


Mohammad Arif¹, Amit Sanger² and Arun Singh^{1*}

1 Advanced Electronic and Nanomaterials Laboratory, Department of Physics, Jamia Millia Islamia, New Delhi, India

2 Department of Materials Science and Engineering, Ulsan National Institute of Science and Technology (UNIST), KIST-UNIST Ulsan Center for Convergent Materials (KUUC), Ulsan, Republic of Korea

*Address all correspondence to: arunsingh07@gmail.com

IntechOpen

© 2019 The Author(s). Licensee IntechOpen. This chapter is distributed under the terms of the Creative Commons Attribution License (<http://creativecommons.org/licenses/by/3.0>), which permits unrestricted use, distribution, and reproduction in any medium, provided the original work is properly cited. 

References

- [1] Wang D, Hu M, Jinag D, Gao X, Fu Y, Wang Q, et al. Preparation and characterization of the CrN nanocone array textured WS₂ film. *Materials Letters*. 2017;**188**:267-270
- [2] Lin J, Sproul WD, Moore JJ, Chistyakov R, Abraham B. Structurally laminated CrN films deposited by multi pulse modulated pulsed power magnetron sputtering. *Surface and Coatings Technology*. 2011;**206**:1780-1786
- [3] Sanger A, Kumar A, Kumar A, Jain PK, Mishra YK, Chandra R. Silicon-carbide nano cauliflowers for symmetric supercapacitor devices. *Industrial and Engineering Chemistry Research*. 2016;**55**:9452-9458
- [4] Zhu C, Yang P, Chao D, Wang X, Zhang X, Chen S, et al. All metal nitrides solid-state asymmetric supercapacitors. *Advanced Materials*. 2015;**27**:4566-4571
- [5] Lu X, Liu T, Zhai T, Wang G, Yu M, Xie S, et al. Improving the cycling stability of metal–nitride supercapacitor electrodes with a thin carbon shell. *Advanced Energy Materials*. 2014;**4**(1300994):1-6
- [6] Balogun M, Qiu W, Wang W, Fang P, Lu X, Tong Y. Recent advances in metal nitrides as high-performance electrode materials for energy storage devices. *Journal of Materials Chemistry A*. 2015;**3**:1364-1387
- [7] Yue Y, Han P, Dong S, Zhang K, Zhang C, Shang C, et al. Nanostructured transition metal nitride composites as energy storage material. *Chinese Science Bulletin*. 2012;**57**:4111-4118
- [8] Singh R, Chakravarty A, Chowdhury U, Bhattacharya D, Biswas SK. Electrical conduction in aluminium nitride-single-walled carbon nanotube nanocomposites. *Materials Letters*. 2018;**215**:144-147
- [9] Guo K, Lu J, Guo Q. A facile method of massively producing three-dimensional silicon nitride nanowire cloth. *Materials Letters*. 2016;**185**:222-225
- [10] Gao T, Gong L, Wang Z, Yang Z, Pan W, He L, et al. Boron nitride/reduced graphene oxide nanocomposites as supercapacitors electrodes. *Materials Letters*. 2015;**159**:54-57
- [11] Xie K, Yang J, Zhang Q, Guo H, Hu S, Zeng Z, et al. Burning the mixture of graphene and lithium nitride for high-performance supercapacitor electrodes. *Materials Letters*. 2017;**195**:201-204
- [12] Figueiredo NM, Louro C, Galindo RE, Climent-Font A, Cavaleiro A. Structural and mechanical properties of Au alloyed AlO sputter deposited coatings. *Surface and Coatings Technology*. 2012;**206**:4463-4466
- [13] Constantin C, Haider MB, Ingram D, Smith AR. Metal/semiconductor phase transition in chromium nitride (001) grown by rf-plasma-assisted molecular-beam epitaxy. *Applied Physics Letters*. 2004;**85**:6371-6373
- [14] Kumbhar VS, Jagadale AD, Shinde NM, Lokhande CD. Chemical synthesis of spinel cobalt ferrite (CoFe₂O₄) nanoflakes for supercapacitor application. *Applied Surface Science*. 2012;**259**:39-43
- [15] Umm-I-Kalsoom RA, Ali N, Khan IA, Saleem S, Ikhlaq U, Khan N. Effect of power and nitrogen content on the deposition of CrN films by using pulsed dc magnetron sputtering plasma. *Plasma Science and Technology*. 2013;**15**:666-672
- [16] Baldenebro-Lopez FJ, Gomez-Esparza CD, Corral-Higuera R,

Arredondo-Rea SP, Pellegrini-Cervantes MJ, Ledezma-Sillas JE, et al. Influence of size on the microstructure and mechanical properties of an AISI 304L stainless steel-a comparison between bulk and fibers. *Materials*. 2015;**8**:451-461

[17] Barata A, Cunha L, Moura C. Characterisation of chromium nitride films produced by PVD techniques. *Thin Solid Films*. 2001;**398-388**:501-506

[18] Wei B, Liang H, Zhang D, Wu Z, Qi Z, Wang Z. CrN thin films prepared by reactive DC magnetron sputtering for symmetric supercapacitors. *Journal of Materials Chemistry A*. 2017;**5**:2844-2851

[19] Choi D, Blomgren GE, Kumta PN. Fast and reversible surface redox reaction in nanocrystalline vanadium nitride supercapacitors. *Advanced Materials*. 2006;**18**:1178-1182

[20] Das B, Behm M, Lindbergh G, Reddy MV, Chowdari BVR. High performance metal nitrides, MN (M = Cr, Co) nanoparticles for non-aqueous hybrid supercapacitors. *Advanced Powder Technology*. 2015;**26**:783-788

[21] Garzon-Fontecha A, Castillo HA, Restrepo-Parra E, De La Cruz W. The role of the nitrogen flow rate on the transport properties of CrN thin films produced by DC magnetron sputtering. *Surface and Coatings Technology*. 2018;**334**:98-104

[22] Zhang L, Dou SX, Liu HK, Huang YH, Hu XL. Symmetric electrodes for electrochemical energy storage devices. *Advancement of Science*. 2016;**3**:12-21

[23] Arif M, Sanger A, Singh A. Sputter deposited chromium nitride thin electrodes for supercapacitor applications. *Materials Letters*. 2018;**220**:213-217

Section 2

Application of Supercapacitors

Performance Evaluation and Control Strategy Comparison of Supercapacitors for a Hybrid Electric Vehicle

*Enhua Wang, Minggao Ouyang, Fujun Zhang
and Changlu Zhao*

Abstract

Electrification of powertrain system is a great technical progress of traditional vehicle, leading to a significant reduction of fuel consumption and emission pollution. Energy storage system (ESS) normally consisting of batteries is a key component of an electric vehicle or hybrid electric vehicle. An ESS can recover braking energy during the regenerative braking process. Currently, lithium-ion batteries are the main energy storage device due to their high energy density. However, sometimes, a sudden large increase of operation current is required during acceleration or regenerative braking processes, which will jeopardize the operation life of batteries. A supercapacitor takes advantage of high power density and can tolerate large current in a short time. Application of supercapacitor in an ESS can reduce the peak current of batteries effectively, and the life time of batteries can be extended. Meanwhile, the braking energy can also be recovered sufficiently. Supercapacitors can be used solely in some hybrid electric vehicles. In this chapter, the application of supercapacitors in electric vehicles or hybrid electric vehicles is reviewed briefly. Then, the performance of a series hybrid transit bus, which uses a compressed natural gas engine and supercapacitors as power sources, is analyzed.

Keywords: supercapacitors, transit bus, control strategy, dynamic programming, series hybrid

1. Introduction

A transit bus is a prime commuting tool for city residents, which consumes lots of fuel every year and produces a huge amount of poisonous emissions [1]. Electrification of transit bus is a good solution for these problems. Normally, the energy storage device consists of batteries [2]. The supercapacitor is a newly developed high-power electrochemical energy storage component [3, 4]. Farkas and Bonert have predicted that a supercapacitor is a good solution for hybrid vehicles [5]. Recently, many researches were performed to study the characteristics of supercapacitors as the energy storage system (ESS) of a hybrid electric vehicle (HEV) [6, 7].

Supercapacitors have a large surface area of electrode materials, which normally are activated carbons, and a very thin electrolytic separator leading to a very high capacitance. They store energy electrostatically. For automotive applications, most of them are electrochemical double-layer capacitors (EDLCs) [8]. Supercapacitors have a very high power density, which is over 10 times than batteries and can be charged or discharged up to 1,000,000 times which is significantly larger than lithium-ion batteries. They also have a very long life time and a wide operation temperature range [9].

Because supercapacitors have a high power density and can be charged or discharged in a short time, they can be used as a sole ESS for transit bus, which undergoes a frequent acceleration and deceleration processes. The first known transit bus powered by supercapacitors alone is Capabus operating in Shanghai since 2010. The buses were manufactured by Sunwin Bus Co., Ltd., and the supercapacitors were provided by Shanghai Aowei Co., Ltd. The transit bus can run 8–10 km each time after being fully charged. A total mileage of several million kilometers has been achieved, and the average energy consumption is close to 0.98 kWh/km [10]. Many other bus manufacturers also developed their products. Higer Bus Co., Ltd. together with an Israeli-Bulgarian bus company designed a transit bus with 20 kWh supercapacitors named as Chariot e-bus [10].

Supercapacitors have a low energy density of up to 10 Wh/kg. However, batteries especially lithium-ion batteries take advantage of high energy density which can be over 180 Wh/kg. For most automotive applications such as a plug-in hybrid electric vehicle (PHEV) or electric vehicle (EV), the ESS should guarantee a driving distance of more than 50 km normally, which can cover over 80% of people's daily travel in Beijing. Therefore, supercapacitors are combined together with batteries as a hybrid energy storage system (HESS). The batteries provide average energy, while the supercapacitors absorb energy during regenerative braking or discharge energy during acceleration. As a result, the high-rate working conditions of the batteries are avoided, and their life spans are extended. On the other hand, the internal resistance of a supercapacitor is much lower than that of a battery; the energy efficiency of a vehicle with an HESS is also improved compared with only batteries. Moreover, the size of the ESS can be decreased if supercapacitors are used. Accordingly, the cost can be reduced. There are mainly three kinds of topologies for HESS: passive, semi-active, and active [11]. Currently, supercapacitor semi-active topology shows a better performance considering efficiency, size, cost, and complexity [12]. Many studies were carried out to determine the size of HESS and optimize the energy management [13–16].

Control strategy design of a hybrid transit bus has important impact on system performance. The control strategy can be categorized as rule-based and optimization-based strategies [17, 18]. Rule-based control strategy specifies the power distribution between the auxiliary power unit (APU) and the ESS based on a set of rules according to the power demand of a vehicle and the state of charge (SOC) of ESS. Thermostatic control, power follower control, and fuzzy logic control are three types of rule-based control strategies [19–23]. Because these strategies do not need information of future driving conditions and have a low computation load, they are appropriate for real-time control application. Optimization-based control strategy splits the power demand based on an optimal algorithm and a mathematical model of the hybrid powertrain. They require the details of the entire driving profile. Normally, they are a kind of global optimization method such as dynamic programming [24], optimal control strategy [25–27], and neural network control [28]. Optimization-based control strategy can be used to estimate the theoretical maximum energy efficiency. However, it requires future information of the driving

velocity and has a huge computation load. Therefore, it is infeasible for a practical real-time vehicle system.

In this chapter, a series hybrid transit bus powered by a compressed natural gas (CNG) engine and supercapacitors is studied. The energy conversion characteristics of the designed series hybrid powertrain are analyzed using a mathematical model. First, two rule-based control strategies—the thermostatic control and the power follower control—are designed and compared. Later, the maximum potential of energy savings is estimated using an optimal control strategy based on dynamic programming. Finally, the operation characteristics of the series hybrid powertrain using the different control strategies are discussed. The results of this study provide a demonstration on how to design an ESS for an electric vehicle or hybrid electric vehicle from the systematic level.

2. System description

The designed series hybrid powertrain for a transit bus is described as follows. A CNG engine is directly connected with a permanent magnetic synchronous generator (PMSG). A high-voltage power line is connected to the generator and the ESS as well as a permanent magnetic synchronous motor (PMSM). The PMSM connected to the final drive is a specially designed low-speed and high-power PMSM. The engine is a Yuchai 6.5 L CNG engine whose rated power is 140 kW. Both the PMSG and the PMSM are developed by Jing-Jin Electric Technologies (Beijing) Co., Ltd. The PMSG is a low-speed and high-efficiency electric machine whose rated power is 135 kW. The rated power of the PMSM is slightly greater than that of the PMSG. These two high-power electric machines have already been applied to several different types of hybrid vehicles successfully. The ESS includes three parallel groups of supercapacitors, and each group consists of 13 units of Maxwell 48 V module connected in series. The total energy capacity of the ESS is 2.115 kWh, and the rated voltage is 624 V. To keep the supercapacitors from overdischarging, the minimum operation voltage of the ESS is set to 300 V.

The working principle of the designed series hybrid powertrain can be explained by an energy flow diagram shown in **Figure 1**. When the series hybrid transit bus is running, four different operation modes are defined according to the working conditions. Two modes are used for the driving conditions, and the other two modes are for the regenerative braking conditions. For the driving mode A, the

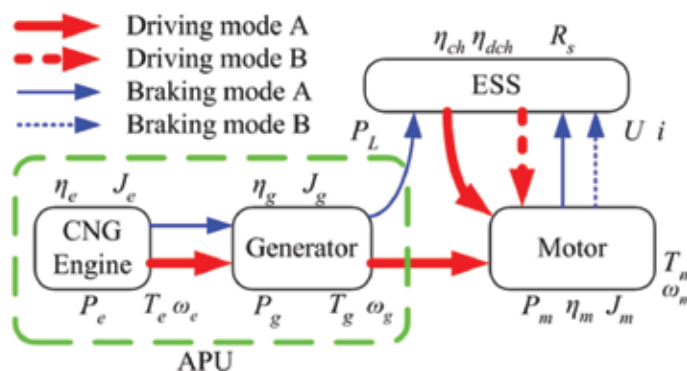


Figure 1.
 Energy flow diagram of the series hybrid transit bus.

CNG engine is running, and the APU together with the ESS supplies electric power to the motor. This driving mode is activated if the required driving power is high or the SOC is low. When the SOC is high and the required driving power is less than a certain value, the ESS provides electric energy to the motor alone as the driving mode B shows. If the series hybrid bus is braking, the regenerative energy output from the motor is supplied to the ESS. Meanwhile, the APU can be activated or deactivated denoted by the braking modes A and B, respectively.

3. Mathematical model

A mathematical model is established according to the working principle of the designed series hybrid powertrain. The corresponding parameters of the hybrid transit bus are listed in **Table 1**. The tractive force acting on a rear-wheel-driven two-axle vehicle can be determined according to the corresponding longitudinal dynamic equation expressed as

$$F = mg \cos \alpha (f_1 + f_2 v) + \frac{1}{2} \rho A C_D v_r^2 + mg \sin \alpha + \delta m \frac{dv}{dt}. \quad (1)$$

The wheel and axle model first calculates the front axle load and the rear axle load according to the technical parameters of the series hybrid transit bus. Then, the tractive force coefficient of the rear tires can be determined. The slip of the tires can be modeled as a function of the tractive force coefficient. Finally, the angular speed of the rear tire can be obtained [29].

If the transit bus is operating at the regenerative braking process, the required braking force F_b can be determined according to the deceleration of the vehicle. Then the regenerative braking force of the rear axle F_{br} is obtained based on the following force distribution equation:

$$F_{bf} = \beta_1 F_b, \quad (2)$$

$$F_{br} = (1 - \beta_1 - \beta_2) F_b. \quad (3)$$

The model of the final drive takes into account the friction loss T_{l0} , and the inertia of rotating parts J_0 and is expressed as

$$T_m = T_w / i_0 + T_{l0} + i_0 J_0 d\omega / dt, \quad (4)$$

Parameter	Value	Unit
Vehicle mass excluding pack	9000	kg
Cargo mass	3200	kg
Dimensions	$8.995 \times 2.42 \times 3.085$	m × m × m
Rolling resistance coefficient	0.0094	—
Aerodynamic drag coefficient	0.79	—
Vehicle frontal area	7.466	m ²
Wheel radius	0.506	m
Final gear	5.833	—

Table 1.
Technical parameters of the series hybrid transit bus.

$$\omega_m = i_0 \omega, \quad (5)$$

where T_w is the output torque of the final drive and T_m and ω_m are the input torque and speed of the final drive, respectively.

The electric motor model determines the requested torque T_{mr} according to the motor inertia J_m and the output torque T_m . Then the input power P_m is calculated based on a two-dimensional (2D) lookup table measured from a motor test bench.

$$T_{mr} = T_m + J_m d\omega_m/dt. \quad (6)$$

$$P_m = f(\omega_m, T_{mr}). \quad (7)$$

The mathematical model of the generator is similar to the motor.

If the detailed physical mechanism of supercapacitors is studied, an electro-chemical model or a high-order equivalent circuit model must be adopted [30]. In this study, we only consider the systematic performance of the ESS. Therefore, the RC equivalent circuit model is built using Advisor. The internal series resistance R_s and capacitance C can be obtained according to the capacitor test procedure. The relation between the current i and the voltage U_c is expressed as

$$i = \frac{dQ}{dt} = C \frac{dU_c}{dt}. \quad (8)$$

With regard to the energy conversion processes during charging or discharging, the current is obtained by

$$i = \frac{U_c - \sqrt{U_c^2 - 4R_s P_L}}{2R_s}, \quad (9)$$

where P_L is the output power of the ESS. During discharging, the energy efficiency η_{dch} is calculated as

$$\eta_{dch} = \left(1 - \frac{R_s i^2}{P_L + R_s i^2} \right) \times 100\%. \quad (10)$$

For charging process, the energy efficiency η_{ch} is expressed as

$$\eta_{ch} = \left(1 - \frac{R_s i^2}{P_L} \right) \times 100\%. \quad (11)$$

The CNG engine model computes the requested torque T_{er} according to the engine output torque T_e and the engine speed ω_e determined by the control strategy block:

$$T_{er} = T_e + J_e d\omega_e/dt. \quad (12)$$

Subsequently, the instantaneous fuel consumption m_e is determined from a 2D map measured by an engine test bench.

$$m_e = f(\omega_e, T_{er}). \quad (13)$$

Then, the equivalent fuel consumption Q_e can be obtained according to the integral values of the fuel consumption and the driving distance using the density of diesel fuel ρ_f :

$$Q_e = \frac{\int_0^{t_f} m_e dt}{\rho_f \int_0^{t_f} v dt}, \quad (14)$$

where t_f is the final time of the driving cycle.

4. Control strategy design

4.1 Rule-based control strategy

To evaluate the performance of the designed series hybrid powertrain, a simulation program is developed according to the established mathematical model with MATLAB/Simulink and Advisor. Advisor is a modeling and simulation tool for hybrid electric vehicle based on MATLAB and Simulink developed by the US National Renewable Energy Laboratory [31]. The designed program is shown in **Figure 2**. Using a backward-facing method, the performance and fuel consumption of the series hybrid transit bus can be calculated. First, the driving force is determined based on the longitudinal dynamic equation. The rotating speed and driving torque of the rear axle are computed according to the tire model. Subsequently, the input torque and speed are determined for the final drive, and the input power of the motor is obtained. Then, the control strategy decides the power distribution between the ESS and the APU. As a result, both the output powers of the ESS and the APU are specified by the power bus. The supercapacitor model calculates the current and energy loss of the ESS. Moreover, the control strategy determines the operation torque and speed of the CNG engine according to the output power of the APU. Then, the fuel consumption is determined based on the performance maps of the CNG engine and the PMSG.

Rule-based control strategy takes advantage of a small computation load, which is very suitable for real-time applications. Therefore, two rule-based control strategies—the thermostatic control and the power follower control—are set up, respectively. The thermostatic control is adopted first for hybrid electric vehicles due to its simple logic. When the HEV is running, if the SOC value drops to a lower bound, the engine starts and operates at a fixed point until the SOC value reaches to an upper bound. The operation condition of the engine is set to the point with the highest effective thermal efficiency.

Large current variation in the ESS may occur for the thermostatic control strategy which results in high energy loss. Therefore, a more sophisticated power follower control is developed. According to this strategy, if the engine state is on, the output power of the APU follows the power demand of the transit bus along an optimal operation line (OOL). Hence, the output power of the APU is decreased, and the operation current of the ESS can be alleviated. The designed power follower control strategy is shown in **Figure 3**. The decision algorithm for the engine state is designed using Stateflow.

Since the power follower control needs to define an OOL, the energy efficiency characteristics of the APU must be studied first. The performance map of the CNG

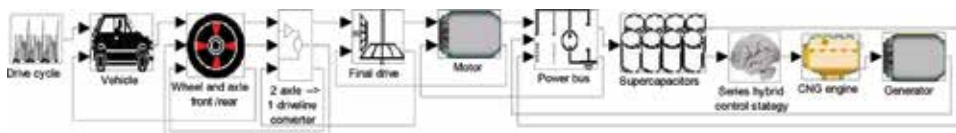


Figure 2.
The analysis program of the series hybrid powertrain.

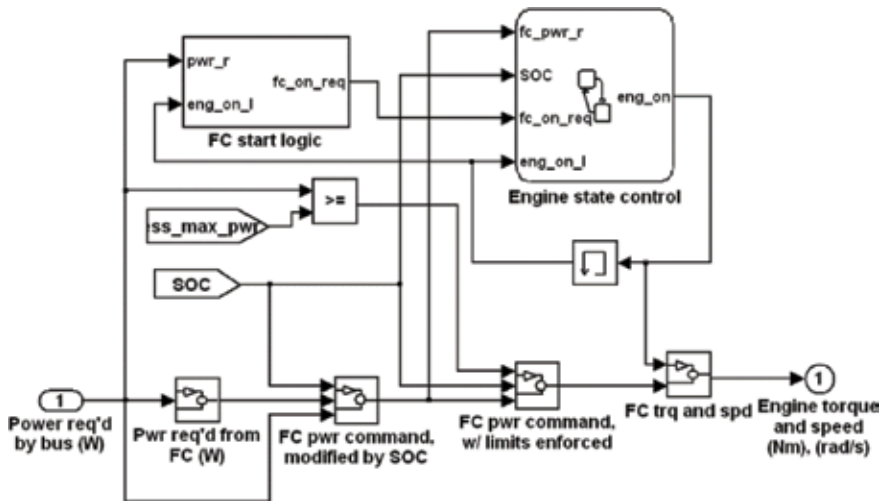


Figure 3.
 The designed power follower control strategy.

engine is shown in **Figure 4a**. The blue contour denotes the engine power in kW. The black contour is the brake-specific fuel consumption (bsfc) in g/kWh. It can be seen that the minimum bsfc of the CNG engine is 196 g/kWh, which is better than that of a diesel engine. The effective thermal efficiency map of the CNG engine shown in **Figure 4b** is obtained based on the performance map of **Figure 4a**. The maximum engine efficiency achieves 36.8%, and in most of the operation regions, the effective thermal efficiency of the CNG engine is greater than 30%. The efficiency map of the PMSG is given in **Figure 4c**, where the highest energy efficiency is 94.5%. In most of the operation regions, the generator efficiency is greater than 89%. The efficiency decreases obviously if the generator speed is less than 500 r/min. According to the results of **Figure 4b** and **c**, the energy efficiency map of the APU is obtained as the product of the efficiencies of the CNG engine and the generator. The engine speed ranges from 900 to 2500 r/min, and the maximum engine torque is 650 Nm, which can be covered completely by the generator's operation domain. The results are given in **Figure 4d**. In this figure, the x-axis is the engine speed, and the y-axis is the engine torque. The blue contour represents the APU output power in kW. The black contours denote the energy efficiency of APU, which decreases with the engine torque and is greater than 30% over the regions of middle and high engine torques. The maximum efficiency is 34.06% located very close to the point with a maximum of engine torque.

Subsequently, the OOL is determined according to the efficiency map of the APU. The efficiency for each point of the OOL is the maximum at each power contour. The result is shown as the green line in **Figure 4d**. The OOL is the same with the external profile when the engine speed is greater than 1600 r/min. Meanwhile, the engine speed of the OOL remains at 900 r/min if the APU power is less than 50 kW. The OOL appears to have a U shape when the APU power is between 50 and 100 kW. Finally, the parameters of the rule-based control strategies must be optimized. The maximum energy efficiency of the APU is 34.06%. This point is denoted as point P in **Figure 8**. The corresponding engine speed and torque are 1543 r/min and 650 Nm, respectively, which are specified as the operation point of the thermostatic control strategy. The lower and upper bounds of the SOC is set to 0.58 and 0.99. The other parameters are also optimized for the power follower control strategy.

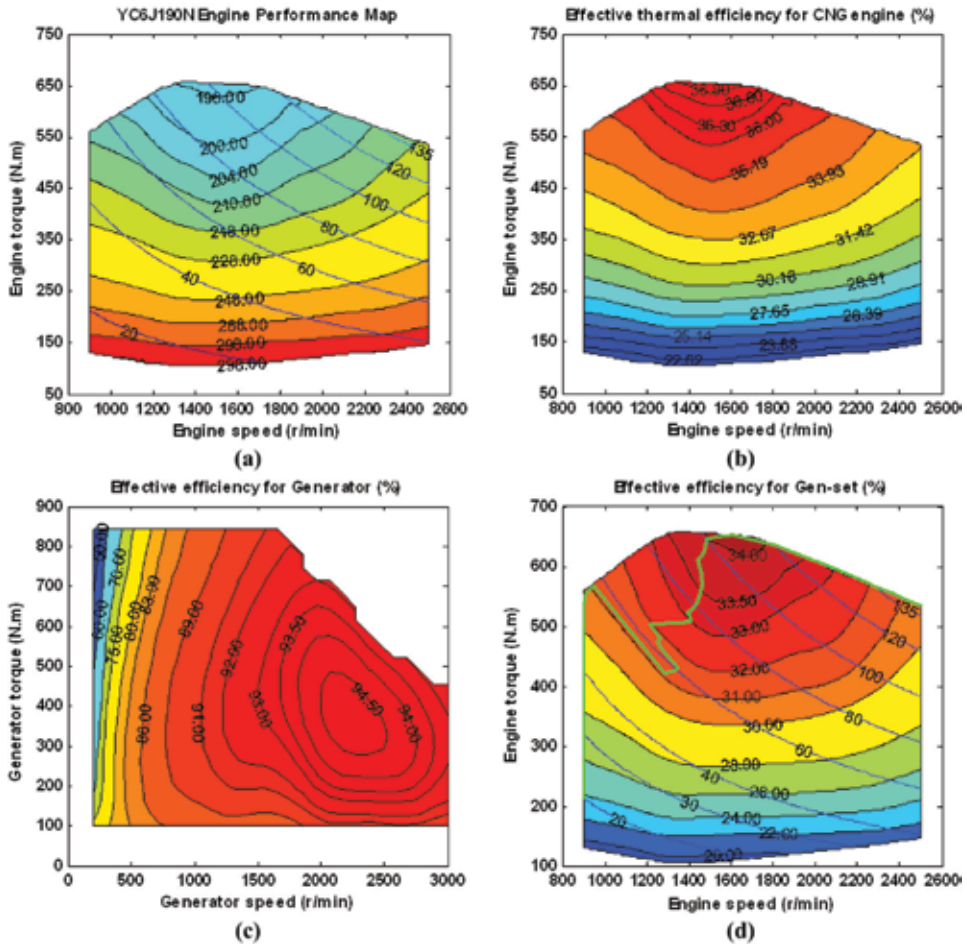


Figure 4. Performance maps of the APU.

4.2 Optimal control using dynamic programming

In order to evaluate the maximum potential of energy savings, the theoretical minimum fuel consumption of the designed series hybrid powertrain is calculated using an optimal control algorithm based on dynamic programming. Dynamic programming is a static backward-facing optimal algorithm according to Bellman's principle of optimality. The boundary conditions of the optimal algorithm are the same with the thermostatic control.

The optimization target is the total fuel consumption based on the Chinese Transit Bus City Driving Cycle (CTBCDC). The SOC of the ESS is used as the state variable, and the output power of the APU is used as the input variable. If the output power of the APU keeps constant, the fuel consumption achieves the minimum when the CNG engine operates along the OOL. Therefore, the corresponding engine output torque and speed are determined. The target function calculates the instantaneous fuel consumption at time t and is denoted by $m(x(t), u(t), t)$. Function $F(x(t), u(t), t)$ is the state equation determining the SOC for the next time. The initial and final states of the SOC are set to the same values as a constraint. Moreover, the SOC and the output power of the APU must be limited within the allowable ranges all the time.

Neither the target function nor the state equation of the designed series hybrid powertrain can be expressed as an explicit equation. Therefore, the analytic solution of this optimal problem cannot be obtained. However, a numerical optimal solution can be determined by a discrete optimal model translated from the aforementioned designed program:

$$\min_{u(k)} J(u(k)) = \sum_{k=1}^{N-1} m_k(x(k), u(k), k), \quad (15)$$

subject to

$$\begin{cases} x(k+1) = F_k(x(k), u(k), k) \\ x(0) = s_0 \\ x(N) = s_0 \\ x(k) \in [\text{SOC}_{\min}, \text{SOC}_{\max}] \\ u(k) \in [0, P_{\text{apu}, \max}] \end{cases} \quad (16)$$

Based on the established model of the series hybrid powertrain, the numerical solution of this discrete optimization problem can be determined. The solution approximates a theoretical minimum of the continuous model if the discrete computational grids for the state and input variables are fine enough. In this study, the discretization steps for the SOC and the APU output power are set to 0.005 and 1 kW, respectively. Since the total driving time of the CTBCDC is 1305 s, a time step of 1 s is used.

The optimization problem for the designed series hybrid powertrain contains the final state constraint, which can be translated to a problem without constraint via a penalty function. Sundstrom et al. have successfully applied this method to optimize the energy management problem of a parallel hybrid electric vehicle [32]. In this research, the penalty function for the state variable x_i at time stage k is defined as

$$\Phi_k(x_i(k)) = \theta(x_i(k) - S_0)^2. \quad (17)$$

Accordingly, the cost-to-go function is defined by

$$J_k(x_i(k)) = \min_{u_j(k) \in U(k)} \{m(x_i(k), u_j(k), k) + J_{k+1}[F_k(x_i(k), u_j(k), k)]\} + \Phi_k(x_i(k)). \quad (18)$$

A program is developed in MATLAB based on the designed optimal algorithm, and its working principle can be explained by **Figure 5**. The entire driving cycle is discretized along the time horizon from stage 1 to stage N shown as the yellow dashed lines. For time stage k , the state variable is discretized from SOC_{\min} to SOC_{\max} in a step of 0.005 and is expressed by $x_i(k)$, $i = 1, 2, \dots, 79$. At each state variable $x_i(k)$, the value of the cost-to-go function is denoted by $J_i(k)$, and the corresponding penalty function is $\Phi_i(k)$. The input variable is discretized from 0 to $P_{\text{apu}, \max}$ in a step of 1 kW and is denoted by $u_j(k)$, $j = 1, 2, \dots, 136$. The fuel consumption from stage k to stage $k+1$ at the state $x_i(k)$ is denoted by the function $m_i(k)$. The initial and final states are constrained to the two red points S_0 shown in **Figure 5**.

The algorithm first calculates the penalty function J_N at the last stage for the state vector x_i :

$$J_N(x_i) = \theta(x_i - S_0)^2. \quad (19)$$

Then taking into account each state variable of stage $N - 1$, a state vector at the next time stage is computed corresponding to the input variable vector based on the state equation. This process is described by a group of lines from one state point of stage $N - 1$ to different positions of stage N . Because the calculated state vector for stage N may not locate exactly at the computational grid points, a linear interpolation is used to determine the values of the corresponding cost-to-go function. Meanwhile, the fuel consumption function for each state variable is calculated. As a result, the values of cost-to-go function at time stage $N - 1$ is obtained according to Eq. (18). The optimal path for each state variable is represented by a blue line in **Figure 5**. The above recurrence calculation process is repeated along the time horizon one by one until to the first time stage. Finally, an optimal map of the cost-to-go function for all the time stages and the state variables is obtained.

In order to determine the optimal policy, a forward calculation process is performed based on the optimal map. The following equation is used to compute the minimum fuel consumption from the initial state S_0 to the same final state, and the corresponding input variable is recorded:

$$M(k) = \min_{u_j(k) \in U(k)} \{m(x_{op}(k), u_j(k), k) + J_{k+1}[F_k(x_{op}(k), u_j(k), k)]\}. \quad (20)$$

where $x_{op}(k)$ is the optimal state variable at stage k . The optimal state value for the next time stage is determined by

$$x_{op}(k + 1) = x_{op}(k) + \frac{(P_m(k) - u(k))C(k)}{U_0^2 x_{op}(k)}, \quad (21)$$

where U_0 is the rated voltage of the ESS. Repeating the calculation process until the last time stage, an optimal policy is obtained shown as the green line in **Figure 5**. The algorithm uses a weighting factor θ for the penalty function whose value specifies the importance of the SOC deviation relative to the fuel consumption. In order to make the final state of the optimal path converge to S_0 , various values of θ are tried. Finally, a value of 120 is specified, and the relative error of the SOC at the last state is 0.44%.

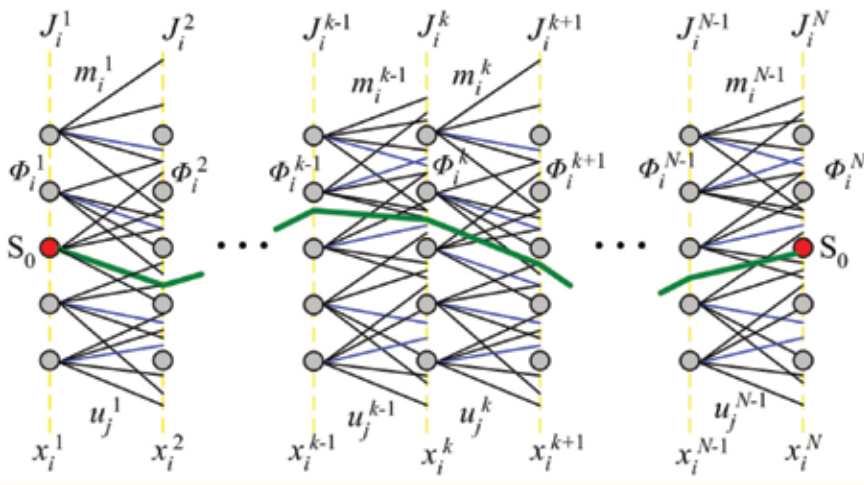


Figure 5. Principle of the optimal algorithm based on dynamic programming.

5. Result analysis

5.1 Comparison of rule-based control strategies

The system performance and fuel economy of the series hybrid transit bus are evaluated using the CTBCDC driving cycle. The performances of the thermostatic control and the power follower control are compared. The results of the thermostatic control strategy are given in **Figure 6**. **Figure 7** shows the results of the power follower strategy.

The target vehicle speed and the achievable vehicle speed are given in **Figures 6a** and **7a**, which are denoted by the blue and magenta lines, respectively. The achievable vehicle speeds for both of the rule-based strategies can trace the target one perfectly. Therefore, both can satisfy the requirements of drivability. **Figure 6b** shows the input power of the PMSM as the blue lines and the output power of the CNG engine by the red lines. **Figure 7b** shows the results of the power

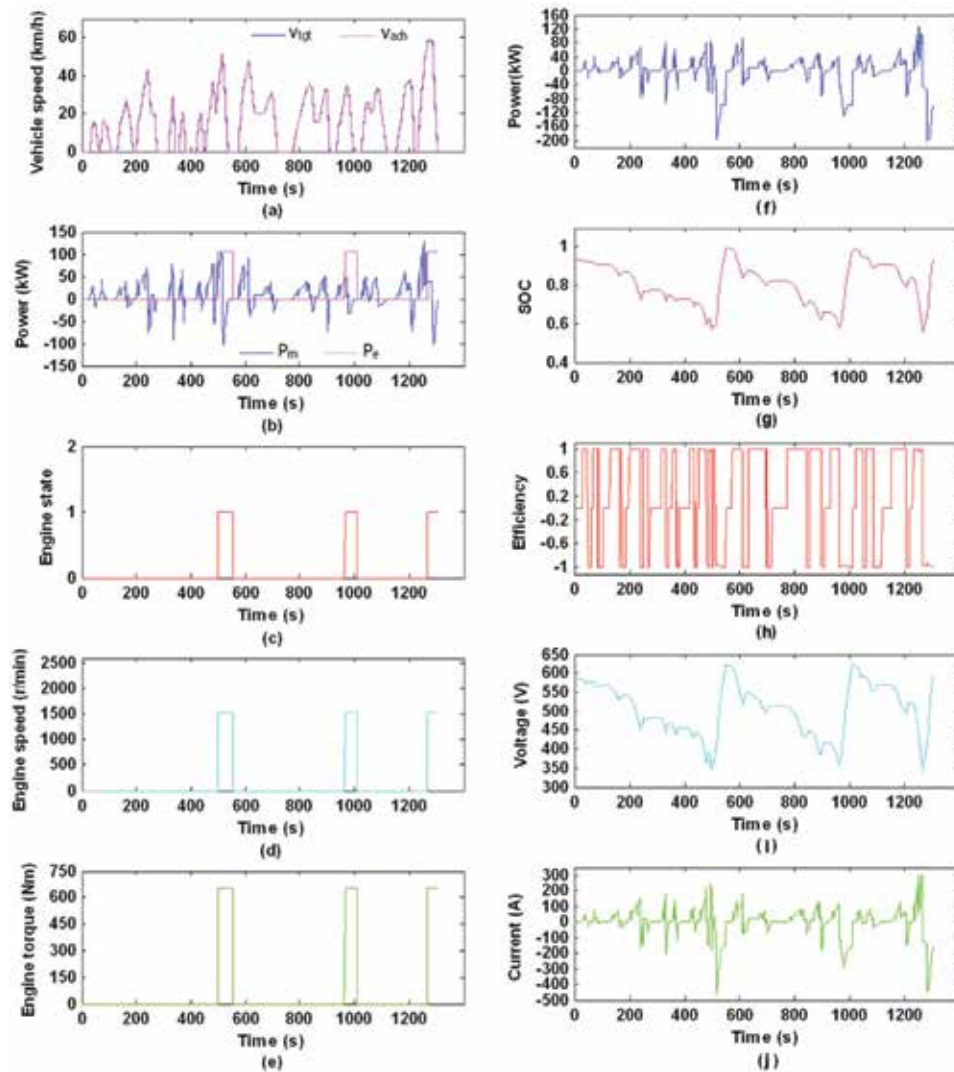


Figure 6.
System performance of the thermostatic control strategy.

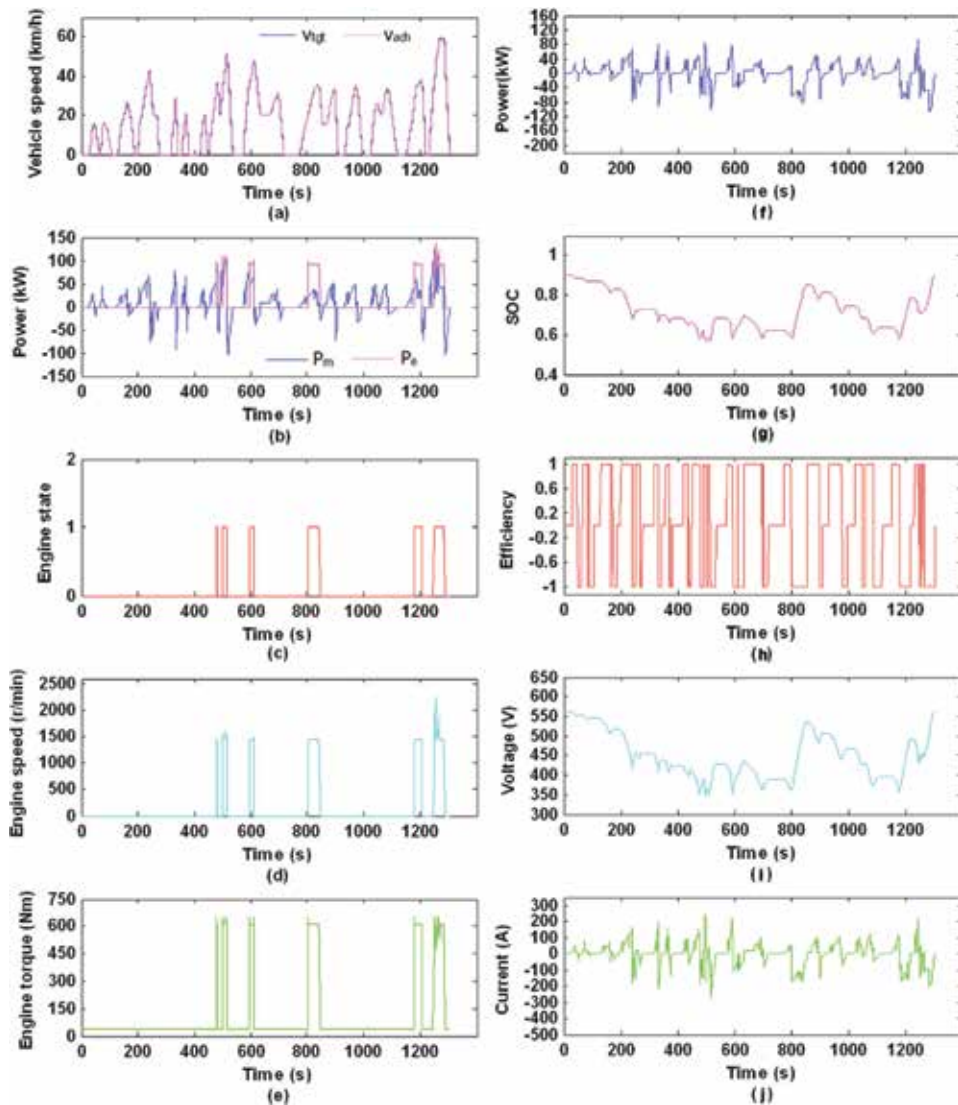


Figure 7. System performance of the power follower control strategy.

follower strategy. The engine operation time of the thermostatic control is less than that of the power follower strategy, which is 141 s for the thermostatic control while 151 s for the power follower control. The engine power keeps constant for the thermostatic control. However, the engine power of the power follower control varies along the OOL within a small range. The results of the engine state for these two control strategies are shown in **Figures 6c** and **7c**, where the engine state ON is represented by 1, and the engine state OFF is denoted by 0. The engine demonstrates a regular alternative start and stop for the thermostatic control, whereas the engine starts more frequently for the power follower control, which will worsen the engine emissions. The engine speed and torque are shown in **Figure 6d** and **e** for the thermostatic control. Compared to the results of the power follower control given in **Figure 7d** and **e**, the engine can operate more stably for the thermostatic control, which will be beneficial for the engine working life.

The output power of the ESS for the thermostatic control is shown in **Figure 6f**, where the positive values mean discharging and the negative values denote charging (this expression is used for the following figures). **Figure 7f** shows the results of the power follower control. Both output powers vary all the time except for the stop-ping conditions. Furthermore, the variation magnitude of the thermostatic control is obviously greater than that of the power follower control. The maximum discharging power for the thermostatic control is 126.8 kW, while this value reduces to 95.68 kW for the power follower control. By contrast, the maximum charging power of the ESS for the thermostatic control is 202.8 kW, while this value reduces significantly to 106.6 kW for the power follower control. The profiles of the SOC are given in **Figures 6g** and **7g**, respectively. In terms of the thermostatic control, the SOC shows an alternative variation process that first decreases slowly then increases rapidly. However, the SOC of the power follower control shows a relative slow augmentation process, which is in favor of the life span of the ESS.

The energy efficiencies of the ESS are obtained according to Eqs. (10) and (11). The results are given in **Figures 6h** and **7h**. The average discharging and charging efficiencies of the power follower control are 99.1 and 98.5%. As a contrast, these two values are 99.1 and 98.4% for the thermostatic control. The results indicate that the energy efficiency of the power follower control is slightly higher than the thermostatic control. The energy efficiency of supercapacitor will decrease obviously if the operation temperature is too high. Therefore, a temperature control system for the ESS is required in practice. The voltage profiles are given in **Figures 6i** and **7i**. Both of them operate within the constraint range. The average voltage for the power follower control is 450 V, while the average voltage is 505 V for the thermostatic control. Enhancement of the operation voltage is helpful to improve the energy efficiency of the electric motor. Because the SOC value has a linear relation with the operation voltage, the variation tendency of the SOC is consistent with that of the voltage. The current profiles are given in **Figures 6j** and **7j**. The maximum discharging and charging currents for the power follower control are 247 and 269 A. However, these two values are increased significantly to 300 and 471 A for the thermostatic control. Although supercapacitors can work with a high power rate, a lower current will be in favor of their life span. Therefore, it seems that the power follower control strategy is better than the thermostatic control.

Table 2 gives the equivalent fuel consumptions of these strategies. The equivalent fuel consumption is 17.32 L/100 km for the power follower strategy, while it equals 17.51 L/100 km for the thermostatic control strategy. In contrast to a conventional vehicle powered solely by the same CNG engine, the fuel consumptions of the two rule-based strategies are decreased by 52%. **Figure 8** is used to explain the reason from a viewpoint of energy efficiency. The OOL is displayed as the green line. Point P is the operation point of the thermostatic control whose energy efficiency is 34.06%. Because most of the APU output power of the thermostatic control first charges to the ESS and then outputs to the power line, the overall energy efficiency of the series hybrid powertrain decreases slightly to 33.2%, which is denoted by a blue contour L in **Figure 8**. The operation points of the power follower control are described by the cyan points. Most of the APU output power is delivered directly to the power line for the power follower strategy. The energy efficiencies for the thermostatic control approximate the line L, while the energy efficiencies of the power follower control remain at the cyan points. Therefore, the fuel economy of the power follower control is a little higher than that of the thermostatic control.

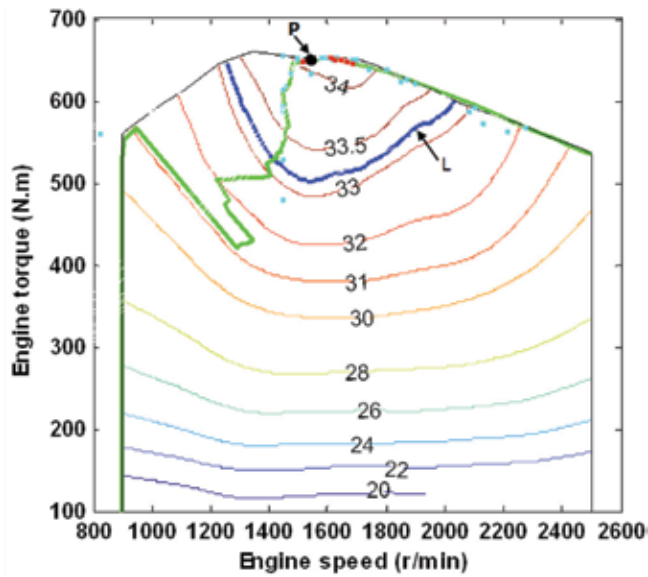


Figure 8.
Comparison of energy efficiencies of different control strategies.

Powertrain	Fuel consumption (L/100 km)	Energy reduction (%) ^a
Conventional bus using a CNG engine	36.60	
Hybrid bus using the thermostatic control	17.51	52.2
Hybrid bus using the power follower control	17.32	52.7
Hybrid bus using optimal control	15.72	57.1

^aRelative to the conventional bus with a CNG engine.

Table 2.
Results of fuel consumption.

5.2 Results of optimal control

The optimal performance of the series hybrid powertrain is shown in **Figure 9**. **Figure 9a** is the velocity profile of the CTBCDC cycle. The corresponding input power required by the PMSM is shown in **Figure 9b**, where the positive values are used for the driving mode and the negative values are used for the regenerative braking mode. These two profiles are used as input parameters for the optimal algorithm. The optimal results of the output power of the APU are given in **Figure 9c**, which demonstrates a series of short impulse when the transit bus undergoes an acceleration process. Furthermore, the number of the impulse increases as the power demand of the motor rises. The APU stops if the power demand of the motor is negative. The corresponding engine output torque and speed are shown in **Figure 9d** and **e**, respectively. The optimal engine speed and torque remain around 1500 r/min and 600 Nm. The reason for such an optimal trajectory can be explained as follows. The operation points of the CNG engine for the optimal control are described by the red points in **Figure 8**. These red points are very close to the point P where the energy efficiency is the highest. Therefore, an overall minimum of the fuel consumption is realized. On the other hand, the

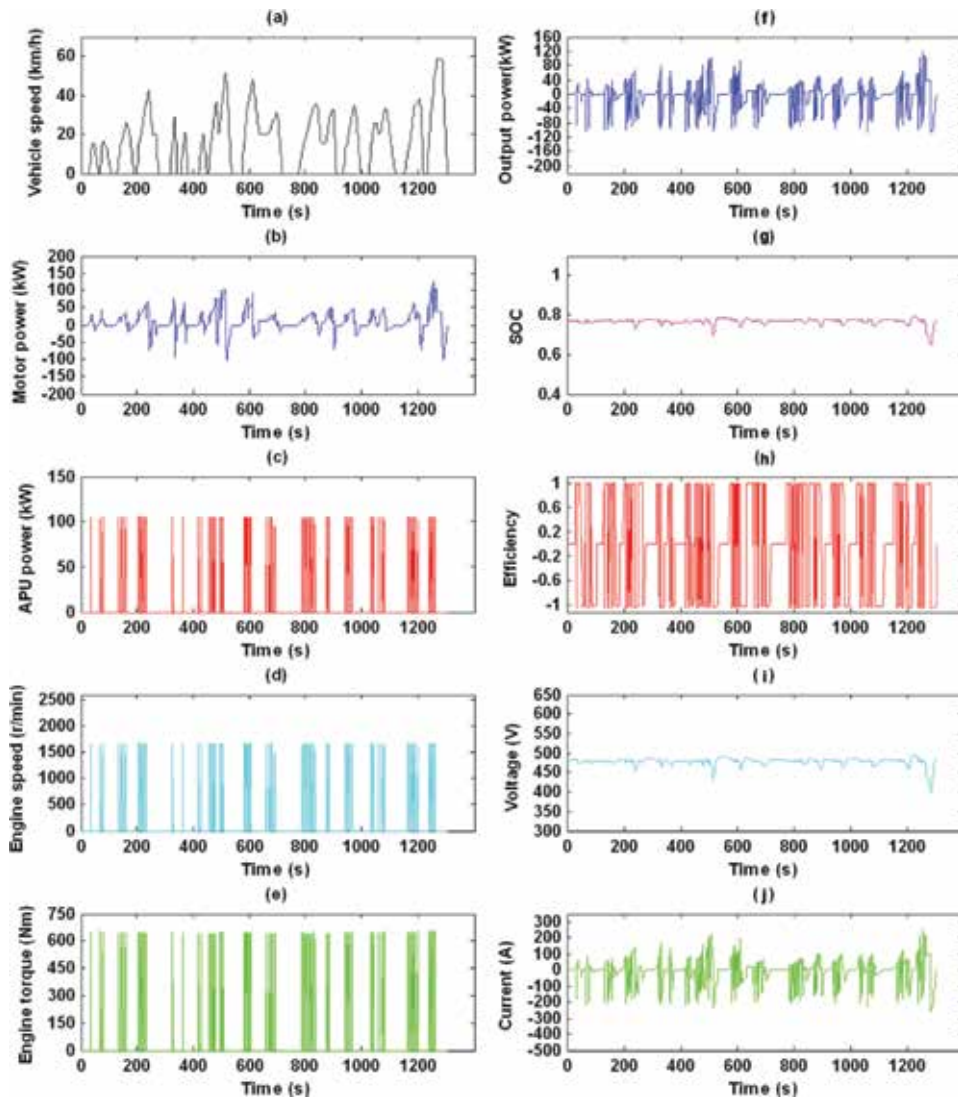


Figure 9. System performance of the optimal control by dynamic programming.

internal series resistance of the ESS consumes part of the energy during the charging or discharging process, especially for large current conditions. To avoid too much energy loss of the ESS, the optimal policy will try to use the APU power to satisfy the power demand of the PMSM exactly. In other words, the optimal policy is obtained if the APU operates at the maximum energy efficiency point and the amount of the output power equals to the power demand of the PMSM, leading to the energy supply in the form of a series of impulse.

The output power of the supercapacitors is given in **Figure 9f**. Generally, the variation tendency of the output power is similar to that of the power follower control shown in **Figure 7f**. However, a series of impulses occur under the driving modes due to the same reason for the output power of the APU. The SOC profile is given in **Figure 9g**. The optimal SOC remains within a small interval around the initial valleys. Only two valleys occur at the high-velocity condition with rapid braking. The energy loss of the ESS is decreased if the current of the ESS is limited

within a small range. Thus, the fuel consumption can be reduced. The calculated energy efficiencies of the ESS are shown in **Figure 9h**. The average energy efficiency is very close to the results of the rule-based strategies. The output voltage and current are given in **Figures 9i** and **j**, respectively. The output voltage is proportional to the SOC. The optimal current demonstrates a similar tendency as that of the power follower control. However, more spikes occur at the driving conditions.

The optimal equivalent fuel consumption is 15.72 L/100 km listed in **Table 2**. Compared to the conventional transit bus, the optimal fuel consumption of the hybrid bus can be decreased by 57% if the quantity of fuel consumed during the starting processes is ignored. In practice, the fuel consumption including starting process will be increased slightly. Taking the optimal result as a reference, the fuel consumptions of the rule-based control strategies are increased by approximate 1.7 L/100 km.

6. Conclusions

In this chapter, the energy efficiency of a series hybrid transit bus powered by a CNG engine and supercapacitors was evaluated. A mathematical model was established, and three different control strategies were designed. The performance characteristics of two rule-based control strategies were compared to the result of the optimal control using dynamic programming. Based on our analysis, the following can be concluded:

1. The performance of the designed series hybrid transit bus powered by a CNG engine and supercapacitors can fulfill the requirements of the vehicle. Because supercapacitors take advantage of low energy loss and can recover the vehicle's kinetic energy efficiently during regenerative braking, the fuel consumption of the designed series hybrid powertrain is decreased significantly by approximately 52% compared to a conventional transit bus under the CTBCDC driving cycle. The results indicate that supercapacitors are a good solution for the ESS of the hybrid transit bus.
2. The energy efficiency of the designed series hybrid transit bus using the power follower control strategy is slightly greater than that of the thermostatic control strategy because the operation current of the ESS remains at a low level. The thermostatic control has a relatively simple logic and less starting times compared with the power follower control. In practice, the most suitable control strategy should be selected according to the requirements of system performance including efficiency, cost, size, reliability, emissions, and so on.
3. The maximum energy efficiency of the designed series hybrid powertrain is estimated using an optimal algorithm based on dynamic programming. The optimal fuel consumption can be decreased by 57% compared to the results of the conventional transit bus. Although the fuel consumption from the rule-based control strategies is slightly higher than that of the optimal control, taking into account the operation requirements of the engine, the rule-based control strategies are more practical for real-time application. However, the result of the optimal control provides some useful insights for real-time control strategy design.

Acronyms

APU	auxiliary power unit
bsfc	brake-specific fuel consumption
CNG	compressed natural gas
CTBCDC	Chinese Transit Bus City Driving Cycle
EDLC	electrochemical double-layer capacitor
ESS	energy storage system
EV	electric vehicle
HESS	hybrid energy storage system
HEV	hybrid electric vehicle
OOL	optimal operation line
PHEV	plug-in hybrid electric vehicle
PMSG	permanent magnetic synchronous generator
PMSM	permanent magnetic synchronous motor
SOC	state of charge

Conflict of interest

The authors declare no conflict of interest.

Author details


Enhua Wang^{1*}, Minggao Ouyang², Fujun Zhang¹ and Changlu Zhao¹

¹ School of Mechanical Engineering, Beijing Institute of Technology, Beijing, China

² State Key Laboratory of Automotive Safety and Energy, Tsinghua University, Beijing, China

*Address all correspondence to: enhua.wang@yahoo.com

IntechOpen

© 2018 The Author(s). Licensee IntechOpen. This chapter is distributed under the terms of the Creative Commons Attribution License (<http://creativecommons.org/licenses/by/3.0>), which permits unrestricted use, distribution, and reproduction in any medium, provided the original work is properly cited. 

References

- [1] Silva C. At what extent the benefits of introducing alternative light-duty vehicles offset those of increasing the buses average occupancy? *Energy Conversion and Management*. 2013;**70**: 211-219
- [2] Bayindir KC, Gozukucuk MA, Teke A. A comprehensive overview of hybrid electric vehicle: Powertrain configurations, powertrain control techniques and electronic control units. *Energy Conversion and Management*. 2011;**52**:1305-1313
- [3] Sharma P, Bhatti TS. A review on electrochemical double-layer capacitors. *Energy Conversion and Management*. 2010;**51**:2901-2912
- [4] Mellincovsky M, Kuperman A, Lerman C, Aharon I, Reichbach N, Geula G, et al. Performance assessment of a power loaded supercapacitor based on manufacturer data. *Energy Conversion and Management*. 2013;**76**: 137-144
- [5] Farkas A, Bonert R. Ultracapacitors as sole energy storage device in hybrid electric cars? In: *Proceedings IEEE Power Electronics in Transportation*, 1994 Oct 20–21, Dearborn, MI, IEEE. 1994. pp. 97-101
- [6] Burke A. Ultracapacitor technologies and application in hybrid and electric vehicles. *International Journal of Energy Research*. 2010;**34**:133-151
- [7] Vinot E, Trigui R. Optimal energy management of HEVs with hybrid storage system. *Energy Conversion and Management*. 2013;**76**:437-452
- [8] Yassine M, Fabris D. Performance of commercially available supercapacitors. *Energies*. 2017;**10**:1340
- [9] Wang E, Guo D, Yang F. System design and energetic characterization of a four-wheel-driven series-parallel hybrid electric powertrain for heavy-duty applications. *Energy Conversion and Management*. 2015;**106**: 1264-1275
- [10] Barbosa FC. Ultracapacitor Transit Bus—Urban Electric Mobility into an Opportunity Charging Concept. SAE Paper 2016-36-0176
- [11] Wang E, Yang F, Ouyang M. A hybrid energy storage system for a coaxial power-split hybrid powertrain. In: Donateo T, editor. *Hybrid Electric Vehicle*. Croatia: InTech; 2017. pp. 83-104
- [12] Veneri O, Capasso C, Patalano S. Experimental investigation into the effectiveness of a super-capacitor based hybrid energy storage system for urban commercial vehicles. *Applied Energy*. 2017. DOI: 10.1016/j.apenergy.2017.08.086
- [13] Geetha A, Subramani C. A comprehensive review on energy management strategies of hybrid energy storage system for electric vehicles. *International Journal of Energy Research*. 2017;**41**:1817-1834
- [14] Min H, Lai C, Yu Y, Zhu T, Zhang C. Comparison study of two semi-active hybrid energy storage systems for hybrid electric vehicle applications and their experimental validation. *Energies*. 2017;**10**:279
- [15] Song Z, Zhang X, Li J, Hofmann H, Ouyang M, Du J. Component sizing optimization of plug-in hybrid electric vehicles with the hybrid energy storage system. *Energy*. 2018;**144**:393-403
- [16] Kouchachvili L, Yaici W, Entchev E. Hybrid battery/supercapacitor energy storage system for the electric vehicles. *Journal of Power Sources*. 2018;**374**: 237-248

- [17] Salmasi FR. Control strategies for hybrid electric vehicles: Evolution, classification, comparison, and future trends. *IEEE Transactions on Vehicular Technology*. 2007;**56**:2393-2404
- [18] Chau KT, Wong YS. Overview of power management in hybrid electric vehicles. *Energy Conversion and Management*. 2002;**43**:1953-1968
- [19] Sorrentino M, Rizzo G, Arsie I. Analysis of a rule-based control strategy for on-board energy management of series hybrid vehicles. *Control Engineering Practice*. 2011;**19**:1433-1441
- [20] Li SG, Sharkh SM, Walsh FC, Zhang CN. Energy and battery management of a plug-in series hybrid electric vehicle using fuzzy logic. *IEEE Transactions on Vehicular Technology*. 2011;**60**: 3571-3585
- [21] Jalil N, Kheir NA, Salman M. A rule-based energy management strategy for a series hybrid vehicle. In: *Proceedings of the 1997 American Control Conference*, 1997 Jun 4–6, Albuquerque, NM, Vol. 1, IEEE. 1997. pp. 689-693
- [22] Hung YH, Wu CH. An integrated optimization approach for a hybrid energy system in electric vehicles. *Applied Energy*. 2012;**98**:479-490
- [23] Xiong W, Zhang Y, Yin C. Optimal energy management for a series-parallel hybrid electric bus. *Energy Conversion and Management*. 2009;**50**:1730-1738
- [24] Perez LV, Bossio GR, Moitre D, Garcia GO. Optimization of power management in a hybrid electric vehicle using dynamic programming. *Mathematics and Computers in Simulation*. 2006;**73**:244-254
- [25] Anatone M, Cipollone R, Donati A, Sciarretta A. Control-oriented modeling and fuel optimal control of a series hybrid bus. In: *SAE Paper 2005-01-1163*. 2005
- [26] Konev A, Lezhnev L, Kolmanovsky I. Control strategy optimization for a series hybrid vehicle. In: *SAE Paper 2006-01-0663*. 2006
- [27] Nguyen A, Lauber J, Dambrine M. Optimal control based algorithms for energy management of automotive power systems with battery/supercapacitor storage devices. *Energy Conversion and Management*. 2014;**87**: 410-420
- [28] Moreno J, Ortuzar ME, Dixon JW. Energy-management system for a hybrid electric vehicle, using ultracapacitors and neural networks. *IEEE Transactions on Industrial Electronics*. 2006;**53**:614-623
- [29] Ouyang M, Zhang W, Wang E, Yang F, Li J, Li Z, et al. Performance analysis of a novel coaxial power-split hybrid powertrain using a CNG engine and supercapacitors. *Applied Energy*. 2015;**157**:595-606
- [30] Wu CH, Hung YH, Hong CW. On-line supercapacitor dynamic models for energy conversion and management. *Energy Conversion and Management*. 2012;**53**:337-345
- [31] Advisor documentation. US: National Renewable Energy Laboratory; 2013
- [32] Sundstrom O, Ambuhl D, Guzzella L. On implementation of dynamic programming for optimal control problems with final state constraints. *Oil & Gas Science and Technology*. 2010; **65**(1):91-102

Edited by Takaya Sato

Application fields of supercapacitors are expanding because they have a very large charge/discharge current density and a cycle durability of tens of thousands of cycles or more compared to secondary batteries. There are various kinds of supercapacitor: electric double layer capacitors with a relatively long history, pseudocapacitors that utilize electrochemical reactions, and the progress of hybrid capacitor technology that combines double layer capacity and electrochemical reactions. Development of electrode materials and electrolytes and new cell design for constructing devices support the performance improvement and expansion of new applied fields such as automobiles, heavy machinery, and energy harvesting. This book aims to provide engineers with the opportunity to review the latest information by integrating cutting-edge papers on science, technology, and the application of supercapacitors.

Published in London, UK

© 2019 IntechOpen
© iammos / iStock

IntechOpen

